2000

A Time Resolved Laser Spectroscopy Study of Resonance Energy Transfer between Tb(III) and an Organic Dye: 6-Hydroxy-5-[(2-methoxy-5-methyl-4-sulfophenyl)azo]-2-na acid disodium salt

Ronald Wesley Tennis
Eastern Illinois University

THESIS/FIELD EXPERIENCE PAPER
REPRODUCTION CERTIFICATE

TO: Graduate Degree Candidates (who have written formal theses)

SUBJECT: Permission to Reproduce Theses

The University Library is receiving a number of request from other institutions asking permission to reproduce dissertations for inclusion in their library holdings. Although no copyright laws are involved, we feel that professional courtesy demands that permission be obtained from the author before we allow these to be copied.

PLEASE SIGN ONE OF THE FOLLOWING STATEMENTS:

Booth Library of Eastern Illinois University has my permission to lend my thesis to a reputable college or university for the purpose of copying it for inclusion in that institution's library or research holdings.

2 May 2000
Date

I respectfully request Booth Library of Eastern Illinois University **NOT** allow my thesis to be reproduced because:

_____

_____

_____

_____ _____

Author's Signature Date

A Time Resolved Laser Spectroscopy Study of Resonance Energy Transfer between Tb(III) and an Organic Dye: 6-Hydroxy-5-[(2-methoxy-5-methyl-4-sulfophenyl)azo]-2-naphthalenesulfonic acid disodium salt.

BY

RONALD WESLEY TENNIS

THESIS

SUBMITTED IN PARTIAL FULFILLMENT OF THE REQUIREMENTS
FOR THE DEGREE OF

MASTER OF SCIENCE

IN THE GRADUATE SCHOOL, EASTERN ILLINOIS UNIVERSITY
CHARLESTON ILLINOIS

2000

I HEREBY RECOMMEND THIS THESIS BE ACCEPTED AS FULFILLING
THIS PART OF THE GRADUATE DEGREE CITED ABOVE

3-31-2000
DATE

4/25/00
DATE

Abstract

Intermolecular energy transfer is a process of crucial importance to photochemistry and photophysics. Complexed lanthanide ions are well suited as energy transfer donors because they display dependable absorption and luminescence qualities with narrow rare-earth ion emission in addition to relatively long excited-state lifetimes.

This project used a pulsed nitrogen laser and high speed digital techniques to study energy transfer dynamics between excited state $Tb(acac)_3$ and an ionic organic dye called Red 40. Luminescence decay profiles of excited terbium atoms in the presence of the quencher were measured in both high and low viscosity solvents. The effects of solvent viscosity and radiative path length on wavelength and time resolved spectra have shown that both radiative energy transfer and resonance (Förster) energy transfer were the principal quenching mechanisms in this system.

The excited state lifetime of terbium in the absence of Red 40 has been determined in cold glycerol and in room temperature ethanol as 1083(10) and 796(5) μs respectively. These lifetimes are similar to those of other reported terbium systems. The Förster critical radius has been determined in cold glycerol and in room temperature ethanol as 81(5) and 85(5) Å respectively. These values are larger than any previously reported critical transfer radii.

Experimentally measured energy transfer efficiencies in cold glycerol were found to be in good agreement with those predicted by Förster theory. Measured diffusion enhanced energy transfer efficiencies in room temperature ethanol solution were also in agreement with theoretical predictions.

This study has revealed trends in excited state lifetimes, diffusion coefficients and activity coefficients that dramatically deviate from those of ideal systems. These trends

suggest that strong ion associations occur in ethanol solutions of divalent Red 40 at concentrations above 10^{-6} M resulting in greatly diminished activity, ionic mobility and diffusion coefficients. Diffusion data were used to estimate mean activity coefficients for Na_2Red 40. The concentration dependences of electrical conductance, diffusion and activity coefficients were found to resemble those of other divalent electrolytes. Differences between electrolyte behavior in ethanol and water were shown to be consistent with their respective dielectric constants.

Dedication

To Bry, Caryn and Francée.

Acknowledgment

I must thank Dr. Giles Henderson for assessing the Laser Lab equipment and proposing the ideal for this project. He gently points to where you have performed well for encouragement. His insight and wisdom were irreplaceable in keeping this project moving.

I thank the Eastern Illinois University Chemistry faculty for their input and suggestions when questions arose.

I also thank my committee, Dr. Giles Henderson, Dr. Carol Deakyne, Dr. Mark McGuire and Dr. Barbara Lawrence for the time they took from their schedules to read this paper and make useful suggestions and ask pertinent questions.

Finally I must thank my Mother, Frances W. Tennis, for her help and patience; without which none of this would have been possible.

Table of Contents

List of Figures

List of Tables

List of Appendices

Introduction.

I. Tb(III) as an Energy Transfer Donor.

Intermolecular energy transfer is a process of crucial importance to photochemistry and photophysics (1-4). Complexed lanthanide ions are well suited as energy transfer donors because they display dependable absorption and luminescence qualities with narrow rare-earth ion emission in addition to relatively long, single exponential, excited-state lifetimes (2, 5, 6). The ability of lanthanide (III) to substitute for Ca(II) makes it useful as a biological probe (7). The relatively high quantum yields of Eu^{3+} and Tb^{3+}, in particular, have made them a popular choice for studying energy transfer mechanisms in solutions (8).

1. *Electronic properties of Tb(III).*

The electronic ground state configuration of Tb(III) is [Xe] $4f^8$. Interelectronic repulsion splits this configuration into Γ spectroscopic terms where Γ = S, P, D, F, etc. These terms are further split by spin-orbital coupling as shown in Figure 1 and result in spectroscopic transitions within the 4f sublevel (9).

Figure 1: Relative energy difference between luminescence energy levels of Tb(III) (9).

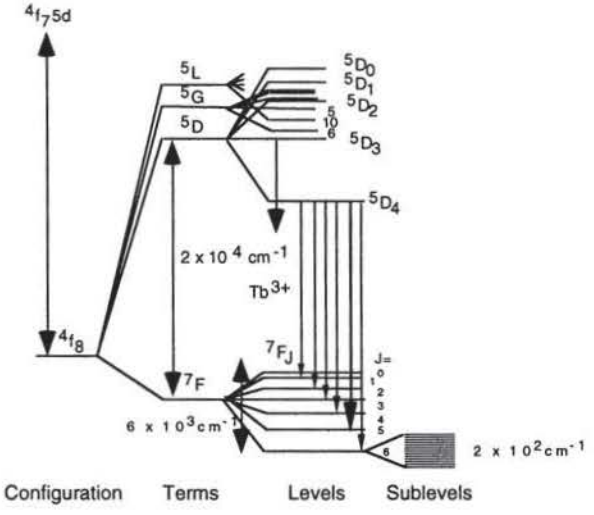

The f orbitals of a lanthanide cation are shielded from the field effects of surrounding anions so there is little perturbation in the electronic transitions between these levels; this results in narrow bandwidth transitions. Since f→f transitions are Laporte forbidden ($g \leftrightarrow u \Rightarrow \Delta l = \pm 1$) the ^5D excited levels cannot be efficiently populated by direct absorption. However, efficient excitation is possible through energy transfer from a chelated sensitizer (10).

2. *Energy transfer from acac sensitizer.*

Crosby et. al. (11) have shown that when $Tb(acac)_3$ is excited with near UV light the absorption is primarily by the attached acetylacetonate (acac) ligand which then intramolecularly transfers the energy to the metal ion. They reported that direct transfer from the acac first excited singlet state is possible but not favorable. When the complex undergoes intersystem crossing to the triplet state, radiation decay of the complex is slower (spin forbidden) and nonradiative intramolecular energy transfer becomes competitive and effective.

Their study showed that if the triplet state was equal to or above the resonance energy level of the metal ion (Figure 2), energy transfer was possible and the mean lifetime of the ion would at least equal that of the triplet state of the ligand complex.

Figure 2: Energy level diagram of the energy migration path of terbium(III) complexed with acetylacetonate (adapted from refs. 12, 13).

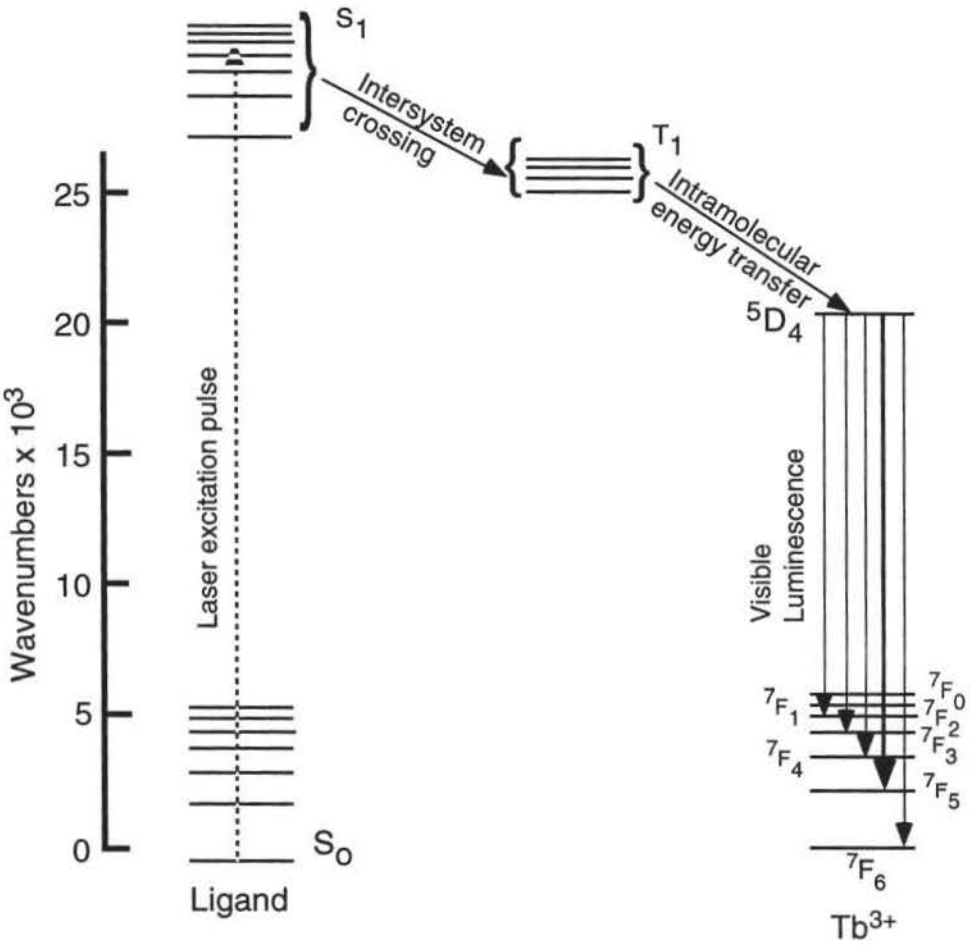

II. Previous Lifetime & Quenching Studies.

1. *Time resolved Tb(III) emission in glass with no quencher.*

Freeman and Crosby (13) undertook a study of rare earth luminescence in a rigid organic glass (EPA) consisting of 4 parts diethyl ether, 4 parts methylpentane and 2 parts absolute alcohol frozen in liquid nitrogen. The purpose was to study the intramolecular energy transfer from the triplet state of various chelate ligands to the excited energy levels of the rare earth ion. They report lifetimes for the $^5D_4$-$^7F_5$ transition of tris

(benzoylacetonate) terbium, tris (dibenzolymethide) terbium, tris (acetylacetonate) terbium and terbium trichloride as 630, 464, 903 and 487 μs respectively. Their frozen glass solvent observation of $Tb(acac)_3$'s lifetime (903 μs) is similar to values observed in various liquid phase solutions (see Table 16).

2. *Quenching by water and oxygen.*

In aqueous solution the Tb(III) ion is generally found to be surrounded by 9 water molecules. The OH vibrational manifold has been found to be an effective quencher of intrinsic Tb(III) ion luminescence (14). The mechanism of this quenching is thought to occur by the transfer of electronic energy from the donor to the OH vibrational manifold. This transfer is enhanced by the fortuitous near resonance of an OH vibrational overtone and the excited $^5D_4$ energy level of Tb(III) (Figure 3). Because the environment immediately surrounding the Tb(III) ion's first coordination sphere greatly affects the luminescence lifetime, Horrocks and Sudnick (7) developed a quantitative method of determining the number of H_2O molecules (in the first coordination sphere) by changing the mole fraction of H_2O with D_2O. Due to the much lower OD vibrational frequency, D_2O is a much less efficient pathway for de-excitation of Tb(III) ion luminescence.

Figure 3: Electronic energy levels for Tb (III). The downward arrow shows the normal luminescence pathway for the ion. The short arrow shows the favorable transition to the OH vibrational overtone system.(5).

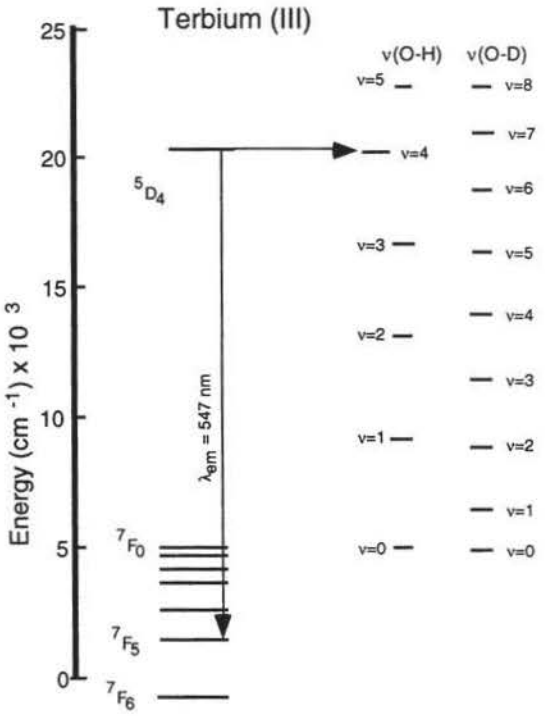

By studying D_2O solutions, τ^{-1}_{OH} vanishes in the following equation:

$$\tau^{-1}_{obsd} = \tau^{-1}_{nat} + \tau^{-1}_{nonrad} + \tau^{-1}_{OH} \qquad (1)$$

where τ^{-1}_{obsd} is composed of τ^{-1}_{nat}, the natural rate constant for photon emission by Tb(III) luminescence, τ^{-1}_{nonrad}, the rate constant for nonradiative de-excitation which does not involve OH oscillators and τ^{-1}_{OH}, the rate constant for nonradiative energy transfer involving OH vibration of molecules in the first coordination sphere. The term, τ^{-1}_{OH}, is significant. τ^{-1}_{obsd} varies linearly with the mole fraction χ_{H2O} in a H_2O-D_2O mixture and allows extrapolation of τ^{-1}_{obsd} to pure D_2O. These values in addition to pure H_2O

measurement yields τ^{-1}_{OH} which is proportional to the number of H_2O molecules in the first coordination sphere.

Tb(III) is classified as a hard acid and so prefers to bond with hard bases such as oxygen. Upon complexation with hard ligands, water molecules are expelled with a corresponding enhancement in emission intensity (14).

Dissolved oxygen is an efficient quencher of nanosecond fluorescence lifetime molecules. Kropp and Windsor (15) have observed the time resolved luminescence of 0.1 M terbium nitrate solution; a) equilibrated with air, b) flushed with helium and c) flushed with oxygen. The observed decay times were within 0.5 % of each other and they conclude that dissolved oxygen has no measurable effect on the approximately 1000 microsecond terbium luminescence lifetime.

3. *La - La energy transfer.*

Shepherd et. al. (8) undertook a study of $Tb(acac)_3$ energy transfer in n-butanol to other acac complexed lanthanide (III) ions: Pr^{3+}, Nd^{3+}, Sm^{3+}, Eu^{3+}, Gd^{3+}, Dy^{3+}, Ho^{3+}, Er^{3+} and Yb^{3+}. The terbium (III) complex was chosen due to its relatively high quantum efficiency of luminescence and the favorable position of terbium's emitting $^5D_4$ energy level which was above many of the acceptor energy levels of the lanthanide complexes.

$Tb(acac)_3$'s observed τ_o of 790 μs was decreased upon addition of other acac complexed lanthanides and was reported to obey the relation:

$$\frac{\tau_O}{\tau_{[Ln]}} = 1 + K_{SV}[Ln] \qquad (2)$$

where τ_o is the intrinsic lifetime with no quencher, $\tau_{[Ln]}$ is the lifetime with quencher and K_{SV} is the Stern-Volmer rate constant for a concentration of lanthanide complex [Ln]. Since the $^5D_4$ level of the Ln^{3+} was some 5000 cm^{-1} below the lowest excited triplet state of the $Tb(acac)_3$ complex, it was concluded that the energy transfer was directly to the Ln^{3+} excited energy levels. Although a Förster energy transfer mechanism was considered, the overlap integral was too small to account for the observed transfer rate. They concluded that energy transfer was through spin allowed Tb to Ln electron exchange.

This study was extended (16) to several polar solvents and two nonpolar solvents. Except for the polar solvents pyridine and dimethyl sulphoxide (DMSO), $Tb(acac)_3$ experienced a decrease in radiative lifetime in polar solvents and obeyed equation (2). There was no obvious correlation between bulk solvent properties such as viscosity or refractive index and the rate transfer constant. It was proposed that $Tb(acac)_3$ and $Ln(acac)_3$ each exist in a dimeric form and that the two dimers mix according to the formula:

$$Tb_2(acac)_6 + Ln_2(acac)_6 \rightarrow 2TbLn(acac)_6 \qquad (3)$$

They report that a rapid exchange on the order of 10^5 s^{-1} is needed for favorable energy transfer. When quenching failed it was thought to be due to a slow exchange rate in these solvents. Dimers would also provide the close proximity needed for electron exchange to occur.

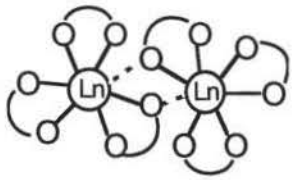

Tanaka et. al. (17) studied energy transfer between trivalent lanthanide ions. Energy transfer rate constants were determined using mixed dimers of tris (acetylacetonate) complex ($[Ln(acac)_3]$) with chloroform as the solvent. The acac complexed trivalent lanthanide ions used for energy donor and acceptors were Pr^{3+}, Nd^{3+}, Sm^{3+}, Eu^{3+}, Gd^{3+},

Tb^{3+}, Dy^{3+}, Ho^{3+}, Er^{3+} and Yb^{3+}. The energy rate transfer constant, 10^4-10^7 s^{-1}, was correlated to the gap in electronic energy levels between donor and acceptor.

Chloroform solutions of $Tb(acac)_3/Eu(acac)_3$ showed an initial fast luminescence decay followed by a longer lived component that was not observed in methanol. A fit of the luminescence lifetime of 5 x 10^{-3} M $Tb(acac)_3/Eu(acac)_3$ in chloroform was 780 μs for the longer component and 200 ns for the short component. It was proposed that three species were present in chloroform; Tb-Tb, Eu-Eu and Tb-Eu. The slow time component was thought to be due to Tb-Tb dimers and the fast component was attributed to Tb-Eu dimers. The lack of the fast component in methanol was thought to be due to competition of the oxygen atoms in the polar donating methanol solvent with oxygen on the ligand for terbium coordination sites. This would prevent dimer formation.

4. *Time resolved Tb(III) emission in the rapid diffusion limit.*

Thomas et. al. (18) studied the effect of diffusion on the rate of nonradiative energy transfer. Tb(III) chelated to dipicolinic acid [$Tb(DPA)_3$] was used because of its relatively long luminescence lifetime (τ_o = 2.2 ms) which permits molecules to diffuse to within the effective energy transfer radius within the excited state lifetime. Rhodamine B or nitrobenzodioxazol (NBD) diethanolamine were used as energy acceptors. By varying the temperature and the concentration of glycerol in a tris buffer solvent, diffusion rates were varied from the static limit (D = 5 x 10^{-11} cm^2/sec) to the rapid diffusion limit (D = 1.5 x 10^{-4} cm^2/sec). Their data were found to be in good agreement with diffusion enhanced energy transfer theory (19).

III. Project Goals.

Previous studies have characterized lanthanide emission parameters in liquid and solid solutions and have included studies of energy transfer between lanthanide metals and from lanthanide donors to a variety of molecular acceptors. This study will employ time resolved laser spectroscopy to study energy transfer between a lanthanide metal and a divalent ionic acceptor in liquid solvents.

Tris (acetylacetonate) terbium ($Tb(acac)_3$) (Figure 4) was selected as an energy transfer donor because: 1) it can be efficiently excited with our nitrogen laser; 2) its excited state lifetime is not affected by dissolved oxygen; 3) the effects of molecular diffusion were expected to be readily observable with terbium's relatively long excited state lifetime; 4) $Tb(acac)_3$ is commercially available.

Figure 4: Structures of tris (acetylacetonate) terbium and Red 40.

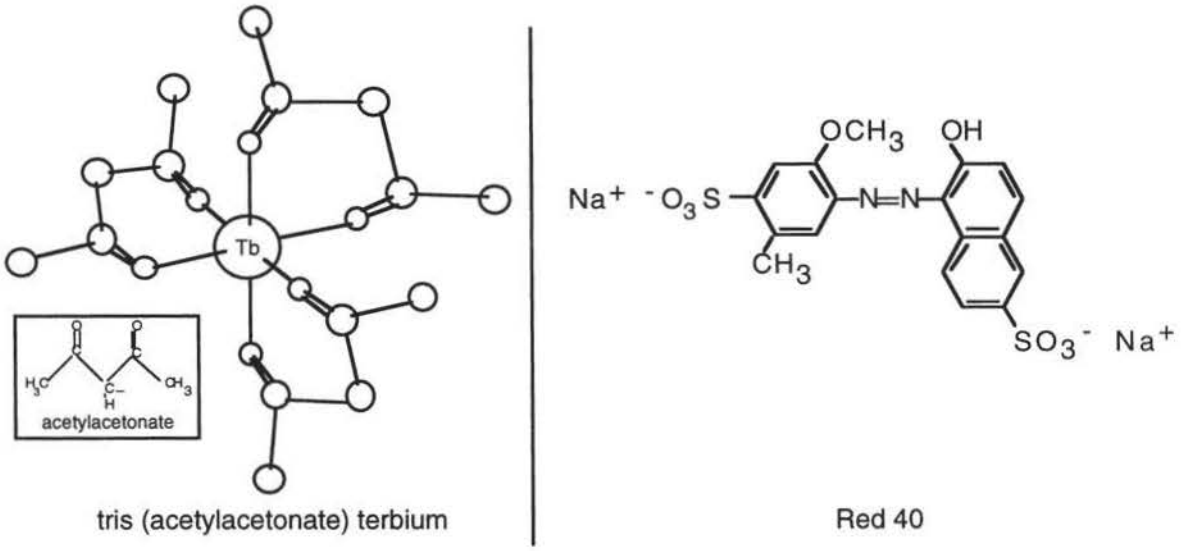

6-hydroxy-5-[(2-methoxy-5-methyl-4-sulfophenyl) azo]-2-naphthalenesulfonic acid disodium salt (hereafter referred to as Red 40) (Figure 4) was selected as an energy transfer

acceptor because: 1) its absorption maximum favorably coincides with the wavelength of terbium's $^5D_4 - {}^7F_5$ emission transition and is therefore a candidate for long range, resonance enhanced Förster transfer; 2) Förster transfer was expected to be enhanced by Red 40's large absorption coefficient ($\varepsilon \approx 18500$); 3) Red 40 is a divalent anion and provides an opportunity to observe electrostatic effects on energy transfer dynamics; 4) Red 40 is commercially available.

The goals of this study are to characterize the quenching mechanism(s) and to evaluate diffusion and electrostatic effects on energy transfer.

IV. Background.

1 *Quenching mechanisms.*

Quenching mechanisms fall under two categories. *Static quenching* decreases the intensity of fluorescent emission while *dynamic quenching* decreases the radiative lifetime through energy transfer. Static quenching mechanisms include both *complex formation* and so called *radiative quenching* (1, 20). Dynamic quenching mechanisms include the *contact electron exchange mechanism* and *resonance enhanced inductive energy transfer*, sometimes called the Förster mechanism (1, 21). Static quenching entails relatively simple mechanisms and will be discussed first.

2. *Static quenching mechanisms.*

A. *Complex formation.*

This static quenching mechanism involves the creation of a ground state *quencher-fluorophore complex* ;

$$D + A \rightarrow [DA] \qquad (4)$$

which is nonfluorescent. Evidence of this formation comes from shifts in the absorption spectrum of the donor when quencher is added. It should be noted that this process lowers the concentration of both D, the ground state donor, and D* the excited state fluorophore. Complex formation attenuates fluorescence intensity but has no effect on $\tau(D^*)$ the excited state lifetime.

B. *Radiative quenching.*

Radiative quenching, sometimes called radiative energy transfer is a 'trivial' mechanism in which the fluorophore emits a photon and an acceptor absorbs it.

$$D^* \rightarrow D + h\nu \qquad (5)$$
$$h\nu + A \rightarrow A^* \qquad (6)$$

The optical pathlength of radiative quenching diminishes fluorescence intensities exponentially in accordance with Beer's law;

$$i = i_o e^{-\varepsilon lc} \qquad (7)$$

where: ε is the absorption coefficient of the quencher, l is the radiative quenching pathlength and c is the quencher concentration. This energy transfer mechanism diminishes fluorescence intensity but does not affect the fluorophore's excited state lifetime and is therefore regarded as a static quenching mechanism.

3. Dynamic quenching mechanisms.

Dynamic quenching processes involve nonradiative energy transfer mechanisms between an excited state donor D* and a ground state acceptor A:

$$D^* + A \rightarrow D + A^* \qquad (8)$$

When a donor molecule (D) absorbs a photon of suitable frequency, it is transformed into an electronically excited state. Electronic energy transfer, or simply *energy transfer*, occurs

when the donor transfers its energy to an acceptor molecule (A) while the donor itself simultaneously becomes deactivated (equation 8).

A. *Contact electron exchange.*

Contact exchange is a nonradiative encounter mechanism that requires orbital overlap of the molecules D and A. The following diagram shows a simplified representation of the electron exchange process.

Figure 5: Simplified diagram showing electron exchange during orbital overlap.

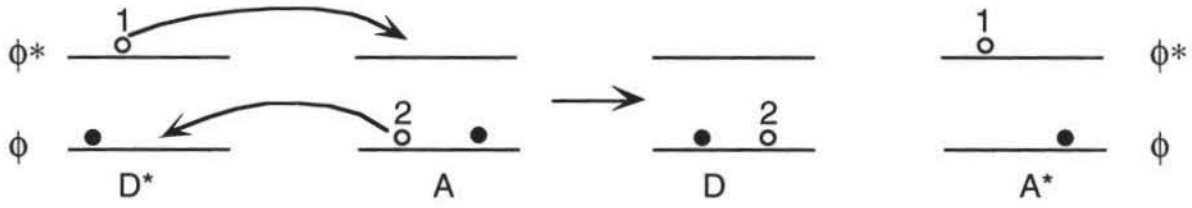

For this contact exchange process to occur the Wigner spin conservation rule (22) must be obeyed. "The spin states produced by coupling of the spins of D* and A in D*/A must yield at least one spin state which is in common with the spin states produced by coupling of the spins of D and A* in the final complex D/A*"(21). The spins of D* and A are S_{D^*} and S_A respectively and consequently, the possible states are described by the Clebsch–Gordan sequence;

$$S_{D^*} + S_A,\ S_{D^*} + S_A - 1 \ldots\ |S_{D^*} - S_A|$$

The corresponding spin states for D/A* are:

$$S_D + S_{A^*},\ S_D + S_{A^*} - 1 \ldots\ |S_D - S_{A^*}|$$

If a donor and acceptor have singlet ground states and singlet and triplet excited states, spin rules may be derived for the system. In singlet to singlet energy transfer, both D*/A and D/A* have possible spin states of 0 in *both* the precursor and the final complex, so energy transfer is allowed. Triplet to triplet transfer also conserves a spin state, but singlet to triplet

transfer is forbidden because this encounter has a precursor state of 1 but a final complex state of 0.

The rate of contact exchange is described by Marcus theory (1) and depends on the free energy of activation of the energy transfer step, $\Delta G^{\neq}_{DA}$. A donor molecule undergoing this type of transfer sees its fluorescent lifetime reduced and obeys Stern-Volmer quenching kinetics which describes the decay of an exited D* molecule by two simultaneous processes: spontaneous emission and bimolecular quenching. The decay of D* can be experimentally measured by observing the emission intensity as a function of time:

$$\frac{d[D^*]}{dt} = - \frac{[D^*]}{\tau_{rad}} - k_{exch}\,[D^*]\,[A] \qquad (9)$$

Here the first term represents decay of the excited state concentration [D*] by spontaneous emission with a radiative lifetime τ_{rad}. The second term describes contact electron exchange quenching which can occur when D* encounters A. This bimolecular process is characterized by a rate constant k_{exch}. The integrated form of equation (9) reveals an exponential luminescence decay[a] :

$$i \propto [D^*] = A\, e^{-t/\tau obs} \qquad (10)$$

where A is a constant and

$$\frac{1}{\tau_{obs}} = \frac{1}{\tau_{rad}} + k_{exch}\,[A] \qquad (11)$$

Since the intensity, i, is proportional to [D*], the luminescence lifetime, τ_{obs} can be obtained from the slope of a plot of ln (i) vs time. This behavior is known as *Stern-Volmer*

[a] In this paper small 'i' = intensity will be used to prevent confusion with capital 'I' = electrical current.

Kinetics. If contact exchange is the only bimolecular quenching mechanism, the radiative lifetime and the contact exchange quenching rate constant can be obtained from a Stern-Volmer plot of $1/\tau_{obs}$ vs [A].

This contact exchange mechanism has no dependence on radiative path length but is limited by diffusion effects. As the viscosity of a solvent system increases, diffusion through the medium becomes increasingly more difficult to the point that donor-acceptor encounters can no longer occur within the donor's excited state lifetime. Marcus theory will not be reviewed here as it will be shown that contact electron exchange makes no significant contribution to the quenching of $Tb^*(acac)_3$ by Red 40.

B. *Resonance enhanced long range energy transfer.*

The energy eigenvalues E_i, and the Born probability functions $\psi_i^* \psi_i \, dq$ of a molecule are time independent or stationary since (23):

$$\hat{H} \chi_i(q) = E_i \chi_i(q) \tag{12}$$

and

$$\psi_i^*(q,t) \, \psi_i(q,t) \, dq = \chi_i^*(q) \, \chi_i(q) \, dq \tag{13}$$

where $\Psi_i(q,t) = \chi_i(q) \exp(-iE_i t/\hbar)$ are the de Broglie standing waves and q and t are generalized spatial and temporal variables respectively. During the interaction with an electric field of suitable frequency, a molecule will change in time from one stationary state to another and can be described as an evolution of intermediate states that are not eigenfunctions of the Hamiltonian.

The time dependent wavefunctions of these intermediate states are described by a linear superposition of the initial and final eigenfunctions (24).

$$\psi = c_1(t)\psi_1(q,t) + c_2(t)\psi_2(q,t) \tag{14}$$

where $\psi_i(q,t)$ are stationary state eigenfunctions and $c_1(t)$ and $c_2(t)$ are time dependent mixing coefficients. Normalization requires that $c_1^2(t) + c_2^2(t) = 1$. At $t = 0$, the onset of a transition between $\psi_2 \rightarrow \psi_1$, $c_1(t) = 0$ and $c_2(t) = 1$. As the molecule evolves between the excited state and ground state, $c_1(t)$ will increase and $c_2(t)$ will decrease. Rabi (25) has determined these coefficients for stimulated transitions:

$$c_1(t) = \sin\left[\frac{\varepsilon<\mu_{1,2}>}{\hbar}\left(\frac{t-t_o}{2}\right)\right] \qquad (15)$$

$$c_2(t) = \cos\left[\frac{\varepsilon<\mu_{1,2}>}{\hbar}\left(\frac{t-t_o}{2}\right)\right] \qquad (16)$$

Here ε is the electric field strength of the radiation, $<\mu>$ is the transition moment integral $<\psi_1 \,|\mu|\, \psi_2>$ which = 0 for forbidden transitions and is > 0 for allowed transitions and t_o is the initial time. Figure 6 graphically depicts how c_1^2 and c_2^2 evolve in time for a stimulated transition.

Figure 6: Rabi coefficients of the linear superposition function.

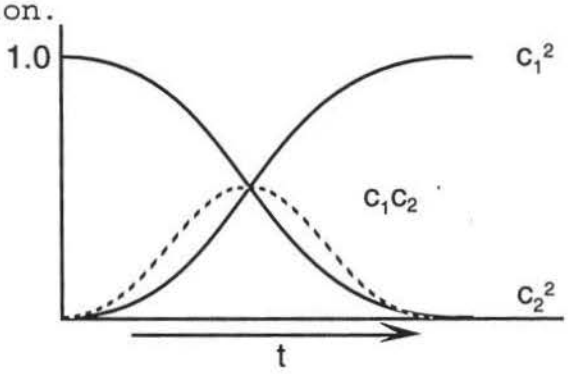

C. *Dynamic transition moment.*

The eigenfunctions oscillate at frequencies $\nu_1 = E_1/h$ and $\nu_2 = E_2/h$. With the mixing of states there can be a dipole or *transition dipole moment* (23) which oscillates at the beat frequency, $\nu = \nu_1 - \nu_2 = (E_1 - E_2)/h$:

$$\langle \mu_{1,2} \rangle (t) = 2c_1(t)\, c_2(t) \langle \mu \rangle \cos(2\pi \nu t) \qquad (17)$$

The amplitude of the oscillating dipole is governed by the product $c_1(t)\, c_2(t)$ as shown by the dotted line in Figure 6.

D. *Maxwell energy transfer.*

An oscillating dipole can inductively interact with an electromagnetic field as predicted by Maxwell's equations and verified by Hertz. This interaction results in a traveling electromagnetic wave that propagates through space at the speed of light. If the difference between energy levels is relatively small, the radiation will be at radio frequencies. Larger energy differences result in oscillations at infrared, visible or UV frequencies.

The cos function in equation (17) has its frequency set by ΔE of the states and $c_1 c_2$ has the effect of scaling the amplitude of the oscillating transition moment. The net result is that photons are emitted as a quantized pulse as shown in Figure 7.

Figure 7: Time dependence of the electric field for a quantum pulse.

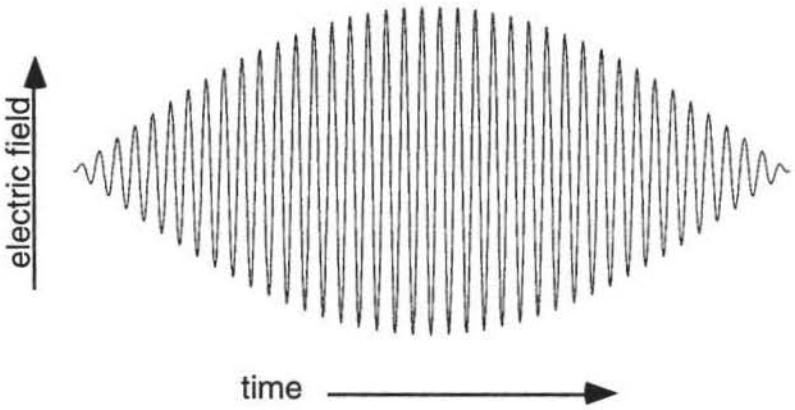

In addition to the Maxwell interaction with an electromagnetic field, an oscillating dipole can also undergo electrostatic interaction with neighboring dipoles.

E. *Coulombic energy transfer.*

Dipole-dipole interactions are based on coulombic potential energy. Two charges q_1 and q_2 separated by a distance r, have a potential energy of interaction given by Coulomb's Law:

$$V = \frac{q_1 q_2}{4\pi\varepsilon_o r} \tag{18}$$

where ε_o is the permittivity of a vacuum. When this is extended to 2 dipoles (26):

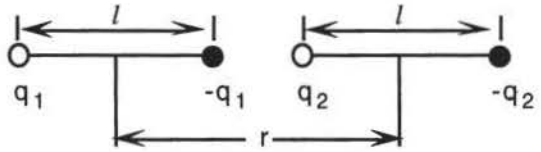

The potential becomes the sum of 4 pairwise interactions. There are 2 attractions between opposite charges that give rise to negative potential terms and 2 positive repulsion interactions such that:

$$V = \frac{1}{4\pi\varepsilon_o r}\left(-\frac{q_1 q_2}{r+l} + \frac{q_1 q_2}{r} + \frac{q_1 q_2}{r} - \frac{q_1 q_2}{r-l}\right) \tag{19}$$

This expression can be written in terms of $\mu_1 = q_1 l$ and $\mu_2 = q_2 l$:

$$V = \frac{\mu_1 \mu_2}{4\pi\varepsilon_o}\frac{2}{r^3} \tag{20}$$

The importance of equation (20) is the r^{-3} dependence for this interaction. Förster (27) has shown that an oscillating dipole-dipole interaction can be a very effective energy transfer mechanism when both dipoles oscillate at the same frequency, i.e. resonance enhanced energy transfer. This mechanism is most easily modeled when there is a fixed distance (r_{DA}) between the donor and the acceptor such a two sites in a rigid macromolecule.

F. *Förster energy transfer.*

Förster (27) derived an expression for the energy transfer rate constant which according to perturbation theory (29) is proportional to the square of the interaction potential and therefore decreases with an r^{-6} dependence on donor-acceptor separation:

$$k_{\mathcal{F}} = \frac{9000 \ln 10 \kappa^2}{128 \pi^6 \eta^4 N \tau_D r^6} \int_0^\infty \frac{f_D(\bar{\nu}) \varepsilon_A(\bar{\nu}) d\bar{\nu}}{\bar{\nu}^4} \qquad (21)$$

where $\bar{\nu}$ is the wavenumber, $\varepsilon(\bar{\nu})$ is the molar decadic extinction coefficient, $f_D(\bar{\nu})$ is the spectral distribution of fluorescence (in quanta, normalized to infinity), N is Avogadro's number, η is the refractive index, r is the radius of the mutual distance between donor and acceptor and τ_D is the radiative lifetime of the excited donor and κ is an orientation factor:

$$\kappa = \cos \phi_{DA} - (3\cos \phi_D)(\cos \phi_A) \qquad (22)$$

where ϕ_{DA} is the angle between transition moment vectors of both molecules and ϕ_D and ϕ_A are the angles between these respective vectors and the direction D $\rightarrow$ A. For a random directional distribution $\kappa^2 = 2/3$.

Equation (21) may be written as:

$$k_{\mathcal{F}} = \frac{1}{\tau_D} \left(\frac{r_o}{r}\right)^6 \qquad (23)$$

where:

$$\tau_D = \Phi_D^{\circ} \cdot \tau_D^{\circ} \qquad (24)$$

and Φ_D° is the quantum yield of donor fluorescence without transfer, τ_D° is the radiative lifetime in the absence of quencher and r_0 is the critical distance over which radiative emission and nonradiative energy transfer have equal probability. Because the $\bar{\nu}$ range of a luminescence-absorption overlap is much less than the integration limits, $\bar{\nu}^{-4}$ can be considered approximately constant and factored out of the integral in equation (25).

$$r_0^6 \approx \frac{9000 \ln 10 \, \kappa^2 \Phi_D^\circ}{128 \pi^6 \eta^4 N \bar{\nu}^4} \int_0^\infty f_D(\bar{\nu}) \, \varepsilon_A(\bar{\nu}) \, d\bar{\nu} \qquad (25)$$

Förster (27) states that:

> "This is valid for any thermal equilibrium distribution over the vibrational levels of both molecules, provided the spectra are taken at the corresponding temperature. The transfer probability is independent of the exciting wavelength even if higher electronic states of the donor are involved. As is to be expected r_0 increases with the quantum yield of the donor and with the overlap of the spectra. In typical cases, r_0 values from 50 to 100 Å have been calculated."

G. *Resonance enhancement.*

Resonance is defined as a large amplitude vibration in a system caused by a relatively small periodic stimulus of the same or nearly the same period as the natural vibration of the system (28). This feature is an important part of the Förster mechanism, as evident in equation (21). The overlap integral in this equation provides a quantitative measure of the resonance condition. Figure 8 compares three hypothetical cases in which both $f_D(\bar{\nu})$, the donor's emission spectrum, and $\varepsilon_D(\bar{\nu})$ the acceptor's absorption spectrum, are represented by simple Gaussian functions:

$$Sig(\nu) = \exp\left[-\left(\frac{\nu - \nu_o}{\Delta^2}\right)^2\right] \qquad (26)$$

Here Δ is the width at half height. The overlap integral, $\langle f_D(\nu) \mid \varepsilon_A(\nu) \rangle$ in cases 1, 2 and 3 reveals the relative energy transfer efficiency for; 1) off resonance ($\nu - \nu_o = 800$), 2) near resonance ($\nu - \nu_o = 50$) and 3) resonance ($\nu - \nu_o \cong 0$) cases respectively.

Energy transfer efficiency dramatically decays with a small off-resonance frequency shift as shown in Figure 8.

Figure 8: Graphic representation of transfer efficiency as ν_1 approaches ν_o. Insets show the relation between ν_1 and ν_o with the resulting overlap integral as the two frequencies approach each other.

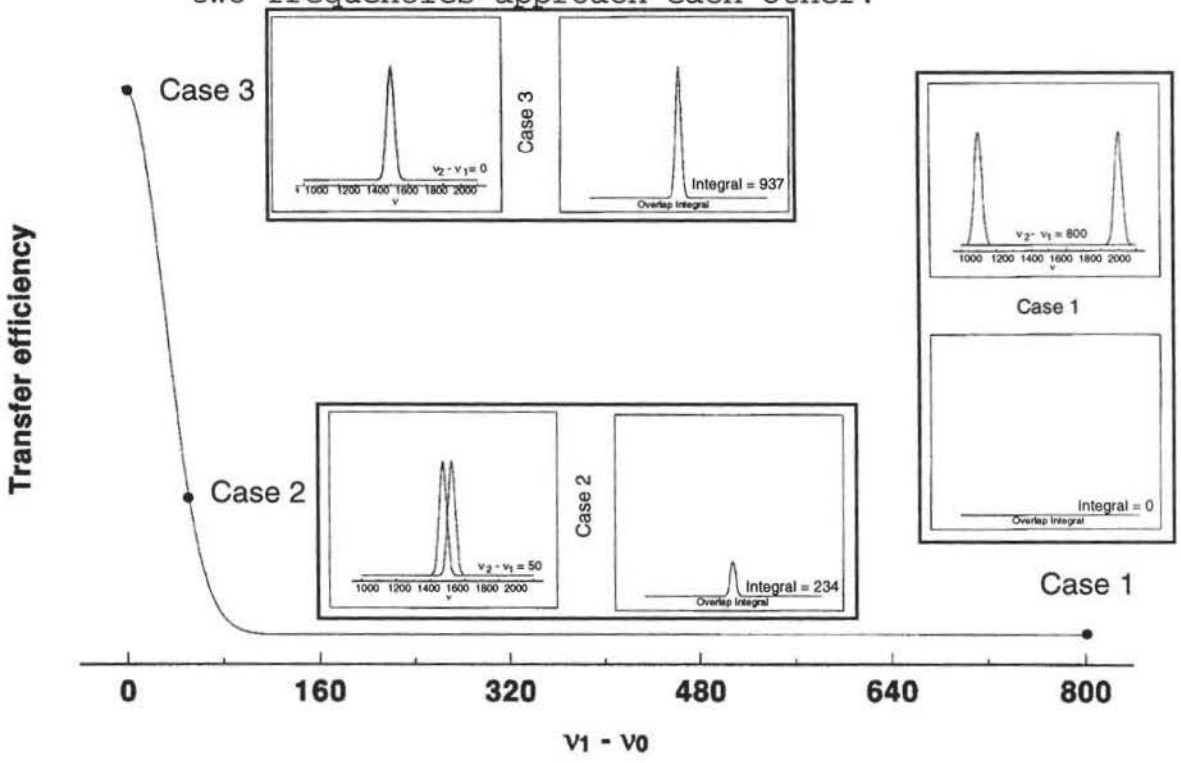

The efficiency of energy transfer from a radio frequency transmitter antenna to a distant receiver is a well known example of this resonance effect. The receiver's response

is imperceptible unless the detector circuit is tuned into resonance with the transmitter frequency.

Resonance transfer occurs before or at least concurrent with photon emission thus quenching the radiative lifetime of the donor. Unlike contact transfer, spin coupling is not required for Förster transfers to take place. A triplet to singlet energy transfer can be quite facile (21, 27).

As with contact transfer τ_0 the natural luminescent lifetime is reduced and the radiative path length has no effect on this mechanism. Unlike contact transfer, the Förster mechanism is not dependent on diffusion effects. Diffusion however modifies the Förster dipole-dipole mechanism and the method of analysis of quenching data. If the transfer is symmetry-forbidden, it could be transferred by higher order interactions such as dipole-quadrupole with an r^{-8} dependence (27). Dexter (30) has shown that these transfers occur over distances larger than those involved with electron transfer.

H. *Energy transfer in a stationary and random distribution of* r_{DA}.

Förster's preceding equations describe energy transfer between a donor and an acceptor, at a fixed r value. A more complex model is required to describe a rigid system with random donor acceptor radii such as a random dispersion of D and A in a rigid glass.

Förster extended his model (28) to describe a stationary and random distribution of r_{DA}, with allowed Brownian rotation. This theory was independently developed by Galanin (31). This model describes donors and acceptors dispersed in solvents of high viscosity such as glycerol. Only donors having at least one acceptor at r_0 or less have any appreciable probability of transferring energy. When D* and A remain effectively stationary during luminescence decay, Förster kinetics (28) shows nonexponential decay according to the relation:

$$[D^*](t) \propto i(t) = i(t)_o \exp\left\{ -\frac{t}{\tau_o} - 2\gamma \left(\frac{t}{\tau_o}\right)^{1/2} \right\} \qquad (27)$$

where τ_o is the radiative lifetime of the donor D in the absence of acceptor A.

and

$$\gamma = \frac{[A]}{[A]_o} \qquad (28)$$

where $[A]_o$ the 'critical' molar concentration of A is given by:

$$[A]_o = \frac{3000}{2\pi^{3/2} N r_o^3} \qquad (29)$$

and N is Avogadro's number.

I. *Effects of diffusion on Förster energy transfer.*

The theoretical description becomes even more complex if r fluctuates during the excited state lifetime of the donor. Efficient energy transfer is not restricted to only donors having an acceptor at r_o or less. Transfer will occur between donors and acceptors that diffuse within the distance r_o during the donor lifetime. For diffusion enhancement, the average distance diffused during the donor's lifetime τ_o must be comparable to $\bar{r} - r_o$ where $\bar{r}$ is the mean donor-acceptor distance as shown in Figure 9.

Figure 9: Representation of r_o and the mean donor-acceptor distance.

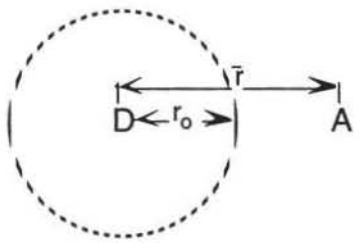

The root mean square diffusion distance in time t is $(6Dt)^{1/2}$ (26, 18, 32) where D is the diffusion coefficient. If $(6D\tau_o)^{1/2} \geq (\bar{r} - r_o)$ then diffusion will substantially increase the rate of energy transfer. In this study we will consider two different theoretical descriptions of energy transfer in the intermediate kinetics case where $(6D\tau_o)^{1/2} \approx (\bar{r} - r_o)$.

Yokota and Tanimoto (32) have developed a theoretical expression for the influence of diffusion on energy transfer and luminescence intensity:

$$[D^*](t) \propto i(t) = i(t)_o \exp\left\{ -\frac{t}{\tau_o} - 2B\gamma \left(\frac{t}{\tau_o} \right)^{1/2} \right\} \qquad (30)$$

where

$$B = \left(\frac{1 + 10.87x + 15.5x^2}{1 + 8.743x} \right)^{3/4} \qquad (31)$$

and

$$x = \frac{D\alpha^{-1/3}}{t^{2/3}} \qquad (32)$$

and

$$\alpha = \frac{r_o^6}{\tau_o} \qquad (33)$$

Voltz (34) developed an alternative expression based on diffusion theory (35). The rate constant of a diffusion-controlled *collision* process is:

$$k = \frac{4\pi N D\rho r}{1000} \{1 + r(\pi Dt)^{-1/2}\} \qquad (34)$$

where r is sum of the collision radii and ρ is the reaction probability per collision (36). By considering a diffusion controlled *energy transfer* process in place of a collision process, r was set to r_o, and since r_o represents a 50% probability of energy transfer or spontaneous

emission, ρ was set to 0.5. Thus, the rate constant for diffusion-controlled energy transfer is:

$$k'_{AD} = \frac{2\pi N D r_o}{1000} \{1 + r_o(\pi Dt)^{-1/2}\} \quad (35)$$

This bimolecular rate constant can be used to describe the excited state decay rate:

$$\frac{d[D^*]}{dt} = -\frac{[D^*]}{\tau_o} - k'_{DA}[A][D^*] \quad (36)$$

where τ_o is the radiative lifetime of the excited donor in the absence of acceptor. Note that unlike the Stern-Volmer rate constant k'_{DA} is time dependent. Through integration (see Appendix A) it may be shown that luminescent decay is described by:

$$[D^*](t) \propto i(t) = i(t)_o \exp\left(-\frac{t}{\tau_o} - k_{AD}[A]t - 2F t^{1/2}\right) \quad (37)$$

where

$$k_{AD} = \frac{2\pi N D r_o}{1000} \quad (38)$$

and

$$F = \frac{2 N r_o^2 (\pi D)^{1/2} [A]}{1000} \quad (39)$$

The first two terms of equation (37) represent the natural radiative decay and exponential bimolecular quenching respectively. The final $2Ft^{1/2}$ term gives log(i) plots subject to Förster transfer a characteristic nonlinear appearance. In the rapid diffusion limit where $(6D\tau_o)^{1/2} >> (\bar{r} - r_o)$, this term becomes small and equation (37) reduces to the

familiar Stern-Volmer expression for bimolecular quenching. Figure 10 demonstrates the dramatic effects that diffusion has on energy transfer and excited state lifetime.

Figure 10: Effect of diffusion on energy transfer. Equation (30) was used to calculate these theoretical profiles using r_o = 87.9 x 10^{-8} cm and τ_o = 800 μs and γ = 2. The diffusion coefficients were D = 0.0, 5 x 10^{-7} and 1 x 10^{-5} cm^2/s for the zero, intermediate and rapid diffusion limits respectively.

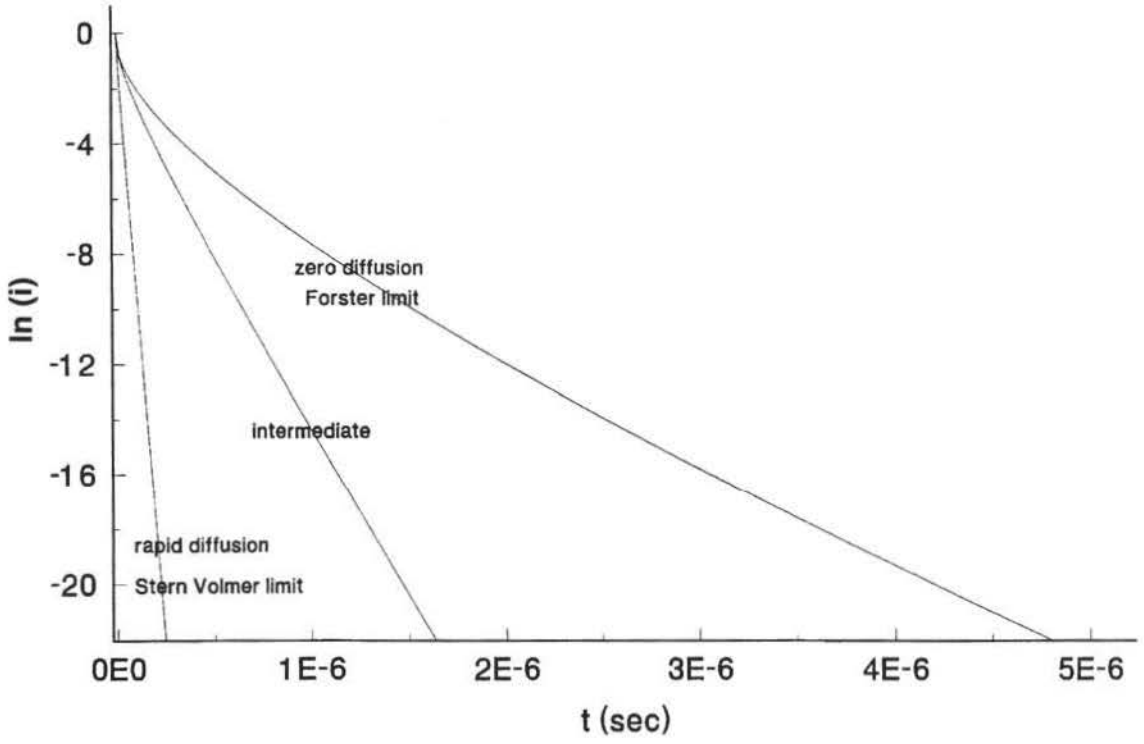

V. Summary of Energy Transfer Characteristics.

The distinguishing features of these various quenching mechanism are summarized in Table 1.

Table 1: Characteristic properties of energy transfer mechanisms (Adapted from reference 27).

	Ground State Complex Formation	Radiative Energy Transfer	Contact Exchange	Resonance (Förster) Energy Transfer
Dependence on radiative path length	none	increase	none	none
Dependence on solvent viscosity	none	none	decrease	none
Donor lifetime	unchanged	unchanged	decreased	decreased
Donor luminescence spectrum	unchanged	changed	unchanged	unchanged
Donor and/or acceptor absorption spectra	changed	unchanged	unchanged	unchanged

VI. Quantum Efficiency.

In the absence of energy transfer, an emission intensity profile is characterized by an exponential decay of lifetime τ_o:

$$i = i_o e^{-t/\tau_o} \qquad (40)$$

As shown above in Figure 10, the shape and duration of this profile can be dramatically altered by the presence of an energy transfer acceptor. The quantum efficiency of energy

transfer can be experimentally measured from the ratio of the respective quantum yields (37):

$$f = 1 - \frac{\Phi}{\Phi_o} = 1 - \frac{\langle i_{\lambda o} \rangle}{\langle i_{\lambda o} \rangle_o} \qquad (41)$$

where Φ and Φ_o are the quantum yields and $\langle i_{\lambda o}(t) \rangle$ and $\langle i_{\lambda o}(t) \rangle_o$ are the integrated intensity profiles with and without acceptor and:

$$\langle i_{\lambda o}(t) \rangle = \int_o^\infty i_{\lambda o}(t)\, dt \qquad (42)$$

In the rapid diffusion limit, the emission profile remains exponential and only the excited state lifetime is shortened by energy transfer as described by Stern-Volmer kinetics. In addition to reducing τ, energy transfer results in nonexponential decay when diffusion and molecular mixing are slow compared to the excited state lifetime. Under these conditions experimental energy transfer efficiencies can be calculated from integrated luminescence intensities (equation 41).

Förster has derived a theoretical expression for the energy transfer efficiency in the zero diffusion limit.

$$f_{DA} = \pi^{1/2}\, \gamma \exp(\gamma^2)\, (1 - \mathrm{erf}\, \gamma) \qquad (43)$$

where γ is defined by equation (28) and erf γ is the integrated error function:

$$\mathrm{erf}\, \gamma = 2\pi^{-1/2} \int_0^\gamma \exp(-x^2)\, dx \qquad (44)$$

In contrast the theoretical transfer efficiency in the Stern-Volmer rapid diffusion limit is given by:

$$f = \frac{k_t[A]}{k_o + k_t[A]} \qquad (45)$$

where k_t is the energy transfer rate constant and k_o is the luminescent rate constant. Voltz (34) has derived a theoretical expression for the energy transfer rate constant in the Stern-Volmer limit as described previously (equation 9, 38).

VII. Conductivity.

Since the Red 40 chromophore is a divalent anion, conductivity measurements can be used to study its mobility (38). Using alternating current (1 to 5 kHz) the problem of polarization that occurs with direct current, is avoided because any chemistry that occurs during one half cycle is reversed by the opposite half cycle (assuming kinetic feasibility).

Ohm's law states that the current through a conductor is proportional to the voltage and inversely proportional to the resistance.

$$I = E / R \qquad (46)$$

where E is in volts, I is the current in amps and R is the resistance in ohms. Resistivity relates the measure of a conductor's resistance to its length and cross-sectional area.

$$R = \frac{\rho\, l}{A} \qquad (47)$$

Here ρ is the resistivity in (Ω m), l is the length of a conductor and A is the cross sectional area (Figure 11).

Figure 11: Representative drawing of a conductor.

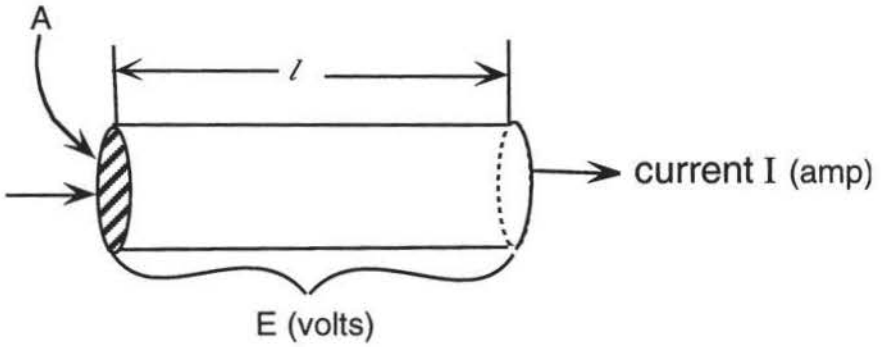

Conductance G, for a solution, is the inverse of its resistance R in ohms (Ω^{-1}). The reciprocal ohm is called the siemens, S ($1S = 1\Omega^{-1}$). Conductivity κ is the inverse of resistivity:

$$R = \frac{\rho\, l}{A} \quad \text{so} \quad R = \frac{l}{\kappa A} \quad \text{and} \quad \kappa = \frac{l}{RA} \tag{48}$$

where l is the length of the conducting pathway or distance between electrodes and A is the cross sectional area (Figure 11, 12). The units of κ are Sm^{-1} with the resistance in ohms and the electrode dimensions in meters or Scm^{-1} if the electrode dimensions are in centimeters.

Figure 12: The conductivity cell counterpart to a solid conductor.

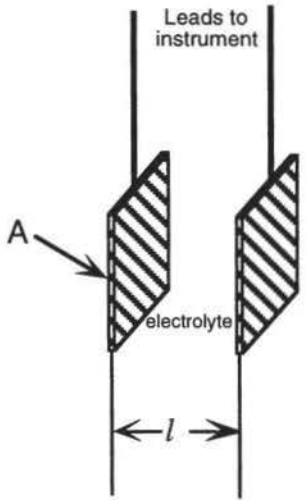

A conductivity cell can be calibrated with a sample of known conductivity:

$\kappa_{(0.02000M\ KCl)}$ = .002768 Scm^{-1} at 25° C, l/A.

In order to adjust conductivity measurements to concentration the term *molar conductivity* is defined as:

$$\Lambda_m = \frac{\kappa}{c} \qquad (49)$$

where Λ_m is the molar conductivity (S cm^2 mol^{-1}) and c is the molar concentration of the electrolyte.

In spite of having adjusted for electrolyte concentration, molar conductivity varies with concentration (Figure 13). Kohlrausch (38) describes the molar conductivity of dilute solutions of strong electrolytes in terms of the square root of the concentration.

$$\Lambda_m = \Lambda^\circ_m - \mathcal{K}\, c^{1/2} \qquad (50)$$

where $\mathcal{K}$ is a coefficient that depends more on the stoichiometry of the electrolyte (i.e. MA or M_2A) than its identity and Λ°_m is the limiting molar conductivity at infinite dilution.

Figure 13: Molar conductance for a range of concentrations of some common ions (39).

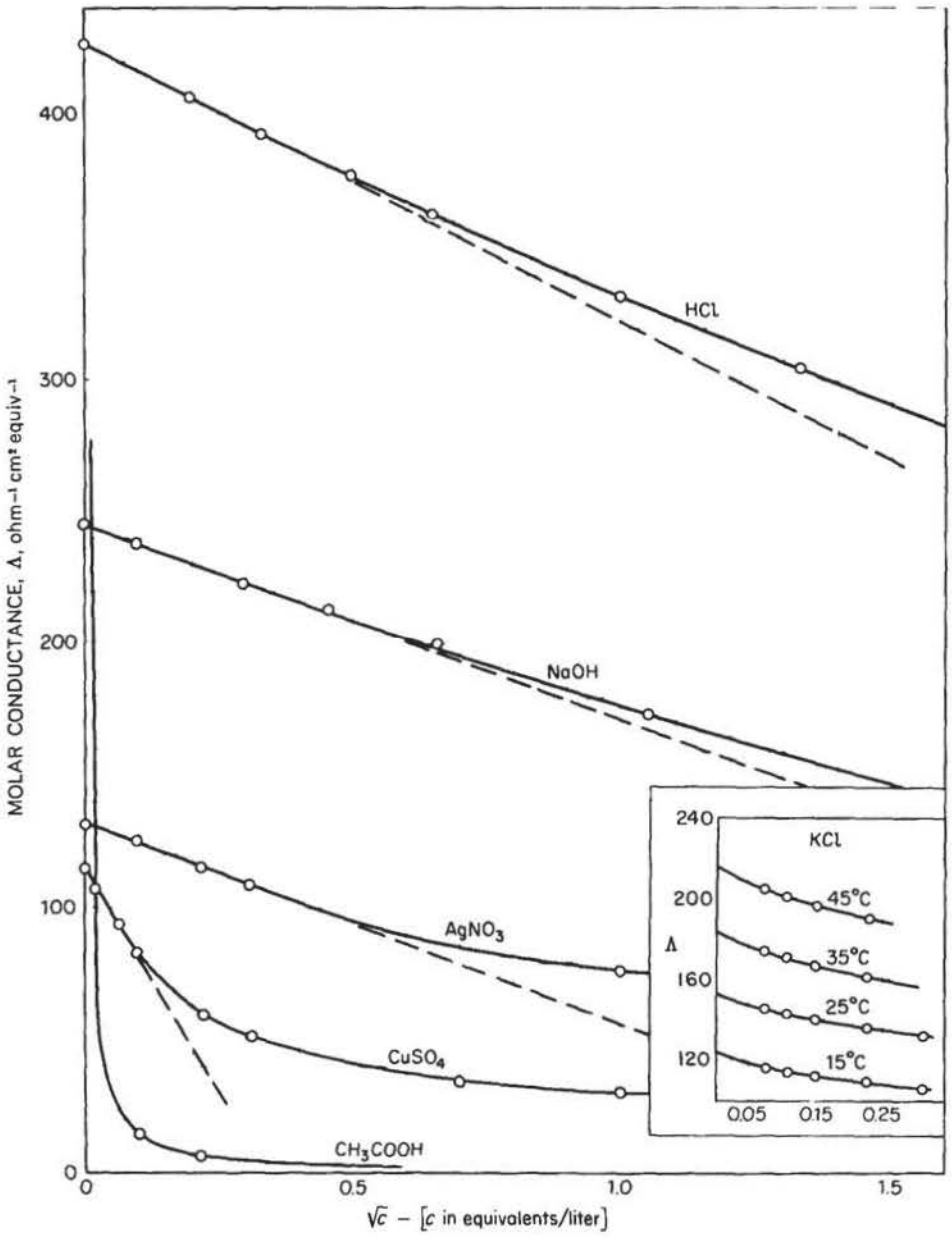

Kohlrausch (38) also confirmed what is now called the law of *independent migration* that shows how ions behave independently in the zero concentration limit:

$$\Lambda^{\circ} = \nu_{+}\lambda_{+} + \nu_{-}\lambda_{-} \qquad (51)$$

where λ_{+} and λ_{-} are the molar ionic conductances at infinite dilution. ν_{+} and ν_{-} are related to the stoichiometry and equal 1 for molecules such as HCl, NaCl but $\nu_{+} = 1$ but $\nu_{-} = 2$ for $MgCl_2$.

Conductivity measurements show that there are two classes of electrolytes; strong electrolytes whose molar conductivity decreases only slightly as the concentration is increased and weak electrolytes whose conductivity decreases sharply at low concentrations (Figure 13).

1. *Conductivity theory.*

When an electric field is applied, ions move through a solution in a series of zigzag steps somewhat like Brownian motions. Opposing the persistent average drift in the field direction is the frictional drag of the solvent. Small ions give rise to stronger electric fields so that a small ion has a larger hydrodynamic radius because it drags many solvent molecules through a solution in a viscous effect. Onsager attributes the dependence of molar conductivity on concentration to two dynamic effects (40, 41).

An ion in a static position is surrounded by an atmosphere of opposite charge. An ion's jump to a new position will drag the oppositely charged aura along. The ionic atmosphere's inertia causes the central ion's atmosphere to become asymmetric.

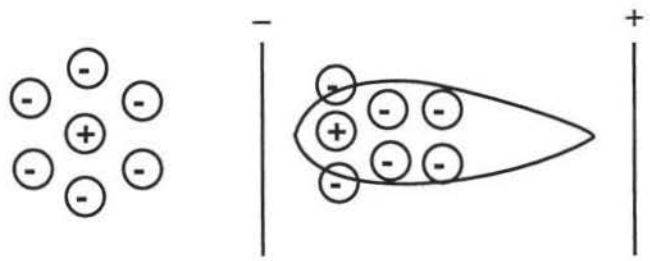

The ion drags behind it a net accumulation of opposite charge which exerts an electrostatic drag. This *asymmetry effect* is greater at high ionic concentrations.

A second factor is the *electrophoretic effect*. An anion migrating in an applied field must overcome the stream of cations moving in the opposite direction. The ions are effectively swimming upstream. When an electric current is applied to an ionic solution the ions will start to move to their respective poles. A steady state current is established when the electric driving force is balanced by the sum of opposing forces due to 1) the frictional drag of the solvent 2) the electrostatic drag associated with asymmetric effects and 3) the electrophoretic drag.

Onsager (40) used this steady state condition to derive:

$$\Lambda = \Lambda_o - \left(\frac{8.204 \times 10^{-5}}{(\varepsilon T)^{3/2}} \Lambda_o + \frac{82.04}{(\varepsilon T)^{1/2} \eta} \right) c^{1/2} \qquad (52)$$

where η is the viscosity of the solvent, ε is the dielectric constant, T is the temperature and c is the ionized solute concentration. Onsager theory correctly predicts the slope of a Kohlrausch plot only in the region of infinite dilution. These plots typically exhibit decreasing slopes at higher concentrations (see Figure 13) (40).

2. *Molar conductivity and diffusion.*

Diffusion describes mixing due to molecular motions and the process is characterized by a diffusion coefficient. The flux of ions diffusing in the z direction is proportional to the concentration gradient (Figure 14).

Figure 14: Diagram of diffusion in a concentration gradient[b].

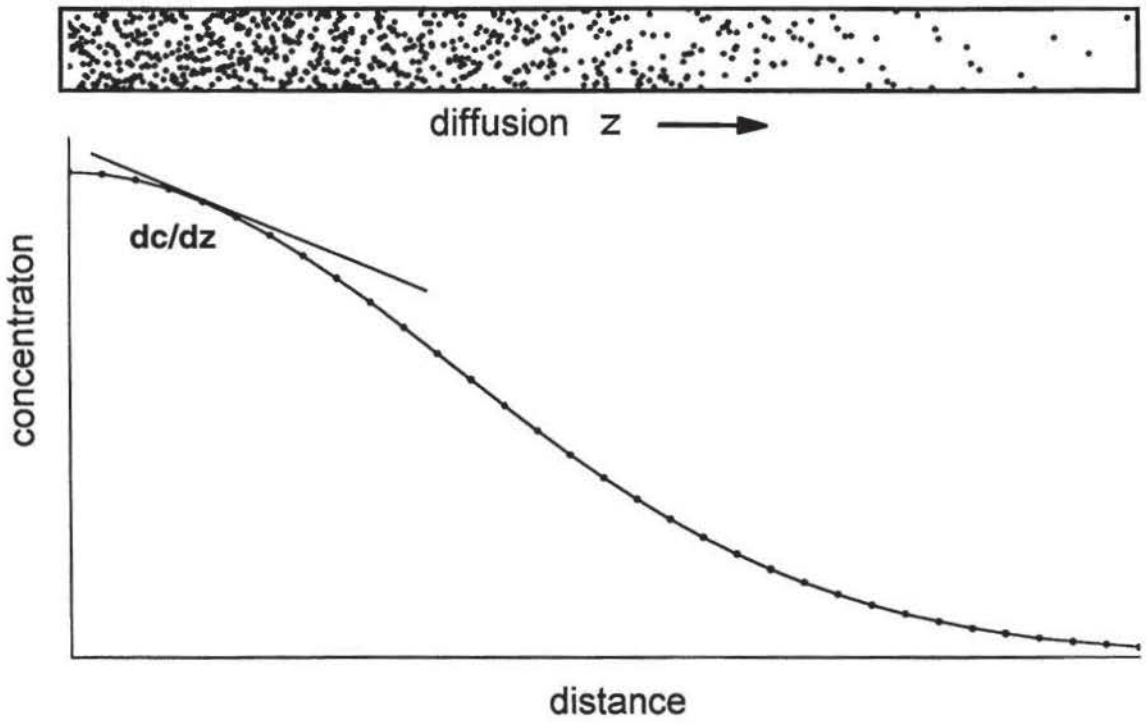

The flux J, of ions is given by Fick's first law:

$$J_{(ions)} = -D \frac{d\mathcal{N}}{dz} \qquad (53)$$

D is the diffusion coefficient and $\mathcal{N}$ is the number density of ions or the number of ions per unit of volume. The negative sign implies that the concentration gradient decreases in the positive z direction or that $d\mathcal{N}/dz$ is < 0. The diffusion coefficient is given by (42):

$$D = 1/3\ \lambda\bar{c} \qquad (54)$$

[b] Figure created by Dr. Giles Henderson using Axum software and qbasic code to generate data.

where λ is the mean free path length and $\bar{c}$ is the average speed. Although a molecule is capable of moving quickly through a given unit of space, its progress in solution is slow because of the short mean free path length and high collision frequency.

Nernst has shown that the mobility of a single ionic species is related to its diffusion coefficients (43):

$$D_i = \frac{RT\lambda_i}{F^2 |z_i|} \qquad (55)$$

Here R is the gas constant, T is the Kelvin temperature, λ_i is the molar conductance for the ionic species, F is Faraday's constant and $|z_i|$ is the absolute value of the charge on the ionic species. This relationship enables a comparison of the effects of concentration on electrical conductivity with the effects of concentration on diffusion enhanced energy transfer.

VIII. Methods Summary.

The distinguishing properties of the various processes described in Table 1 will be used in this study to characterize the quenching mechanism(s) in the $Tb(acac)_3$–Red 40 system. It will be shown that dynamic quenching occurs by long range resonance enhanced energy transfer. High speed digital methods will be used to measure luminescence decay profiles. Interactive curve fitting tools will be developed to determine the Förster critical radius in the zero diffusion limit. These methods will then be used to compare and evaluate the Voltz and Yakota-Tanimoto theories of diffusion enhanced energy transfer. Experimental energy transfer efficiencies will be compared with theoretical predictions for both Förster and intermediate kinetics. The concentration dependence of diffusion coefficients determined from excited state lifetime measurements will be compared to measured conductivity trends and discussed in terms of the physical chemistry of electrolytes.

Experimental.

I. Materials.

1. *$Tb(acac)_3$ donor.*

Samples of $Tb(acac)_3$ were purchased from Alpha ÆSAR (Stock 40032, lot L28E-24) and Gelest (stock AKT820-1gm, lot 8J-6396). Solubility problems were encountered with both. These samples were slightly off-white powders with similar physical properties. They were in varying degrees insoluble in ethanol and had melting points in excess of 240 °C. Aldrich reported the melting point as 127°C (dec).

Both sample lots were subsequently examined by their respective venders and eventually replaced. More than 33% of the original Alpha sample and 8% of the original Gelest sample were insoluble. Their second samples had 15% and 5% insoluble impurities respectively. Scattering of a HeNe laser beam was readily apparent in all of these solutions under normal room lights even after centrifuging and filtering. It was noticed that both of these samples were advertised as 99.9% REO which stands for Rare Earth Oxides. It seems that there was no real guarantee that they were $Tb(acac)_3$ only that 99.9% of the metal was terbium of some form ($Tb(OH)_3$...$Tb(Cl)_3$...). The components insoluble in ethanol were soluble in dilute HCl.

Aldrich listed 99.9% pure $Tb(acac)_3$ among its new compounds in their 98-99 catalog. This product was found to have a more crystalline texture and the solutions produced could be used directly. Its melting point was 128°C.

2. *Red 40 acceptor.*

Red 40, the quencher used in this study, has a trade name of Allura® Red AC and is also referred to as FD & C Red No. 40. Its formula is $C_{18}H_{14}N_2Na_2O_8S_2$. The structure is shown in Figure 4.

3. *Solvents.*

Reagent grade absolute ethanol (McCormick Distilling) was stored over 4Å molecular sieves. The quality was periodically checked by measuring the refractive index using a Bausch & Lomb (Abbe) refractometer. The index of refraction was compared to data listed in the Handbook of Organic Solvents (45). The ethanol was packaged in 1 pint bottles and proved to be quite consistent from bottle to bottle.

ACS reagent grade glycerol (Mallinckrodt lot 5092M49A03) (0.04% water) was found to be free from fluorescent impurities and was used directly.

4. *Solution preparation.*

A fixed $Tb(acac)_3$ concentration strategy was used to eliminate any self and or solvent quenching effects. Initially, solutions were prepared by weighing approximately 0.07 g of $Tb(acac)_3$ in a 100 mL beaker, adding 20 to 30 mL of ethanol and stirring with heat (60 to 70 °C) for at least an hour. The larger granules would break up under vigorous stirring and heating. Both the Alpha and Gelest samples would stir into a cloudy, almost colloidal suspension. After some experimentation with technique, heating was found to digest the insoluble particles for more effective filtering. A centrifuge was later used to remove large insoluble particles and the solution was then filtered through #2 (Whatman) filter paper into a 200 mL volumetric flask. The previously tared beaker and centrifuge test tubes were then weighed to determine the loss to insolubles.

It was noted that after heating, $Tb(acac)_3$ was less labile with respect to ligand attachment. This was judged by loss of $Tb(acac)_3$ luminescence signal intensity.

A similar quantity of the Aldrich sample was found to be completely soluble and stable upon cooling. These solutions could then be used directly. When the HeNe laser was shone through these solutions, only very faint scattering could be seen with the room lights off.

Typically the samples described above were diluted to 200 mL in ethanol to a concentration of approximately 800 μM. The $Tb(acac)_3$ solution was then used to dissolve about 5 mg of Red 40 to prepare 100 mL of solution. This stock $Tb(acac)_3$/Red 40 solution was then diluted with the $Tb(acac)_3$ solution as a solvent to prepare a series of solutions ranging from 20 μM to 0.27 μM in Red 40 and 800 μM in $Tb(acac)_3$.

In order to study excited state solution lifetimes in the absence of diffusion, $Tb(acac)_3$ /Red 40 solutions were also prepared in glycerol. To facilitate mixing and flow in pipettes and such, the glycerol was heated to about 60 to 70°C. Solutions of 800 μM were used fresh. These solutions were more difficult to handle as glycerol is still sluggish at 60°C, and the heat creates uncertainties in the true volume. Red 40 concentration ranged from 500 μM to 50 μM.

II. Laser Induced Emission Spectrometer and Software.

The excitation source for luminescence emission spectra was a Laser Photonics model LN300C sealed nitrogen laser which produces 3.5 ns pulses of approximately 50 kW peak power. The laser, beam steering optics, monochromator, and detector were mounted on a 1 x 2 meter Ealing optical bench (Ealing Electro-Optics, 89 Doug Brown Way, Holliston MA 01746). First surfaced mirrors and a 125 mm focal length quarts lens were used to direct and focus the laser radiation into the sample cell.

Figure 15: Diagram of optical bench setup for wavelength resolved luminescence studies. M are first surfaced mirrors and P is the PMT.

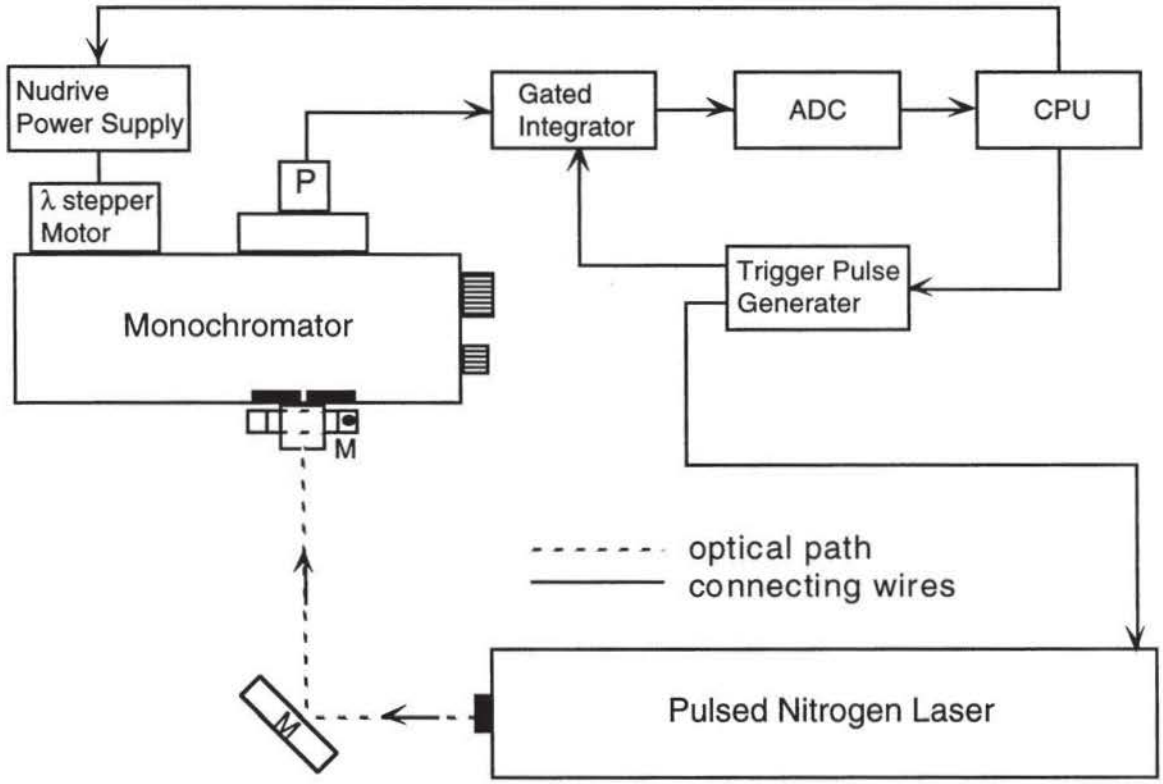

Emission perpendicular to the laser beam was scanned with a modified Hitachi 139 monochromator equipped with a stepper motor geared to the wavelength control, limit switches to protect the monochromator from incorrect scan limits, an optical encoder to calibrate the reading of the wavelength during a scan, and a Hammatsu photomultiplier detector. Power pulses for the wavelength stepper motor were generated with a computer controlled NuDrive (model ISR-2U) power supply.

The sample cell was positioned at the monochromator's entrance slit. A quartz lens and adjustable first surfaced mirrors allowed the laser beam to be focused and aligned for optimum signal strength. Increased signal strength could be achieved by exciting the sample with the laser beam parallel to the vertical monochromator slit. This was achieved by tilting the cell approximately 45° to the normal (Figure 16). It was noted that when a

vertical beam entered the sample cell, the sample solution refracted the beam off of its vertical alignment in accordance with Snell's law. The beam was aligned so that it struck the sample cell at an appropriate angle to create a true vertical beam parallel to the slits for optimum signal strength.

Figure 16: Optical path of laser through sample cell. M is a first surfaced mirror, L is a 125 mm quartz lens, C is the quartz cell and V is a true vertical reference. The drawing is not to scale.

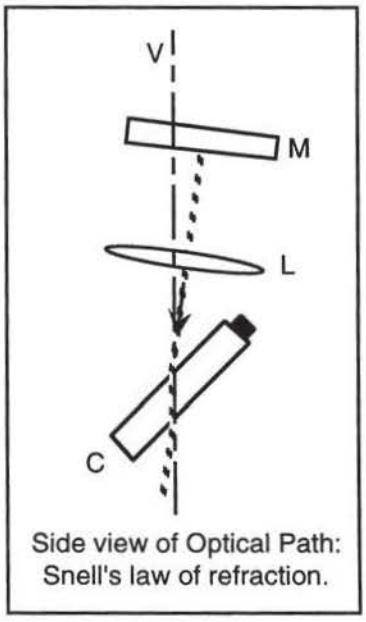

Wavelength resolved emission pulses arrive at a Hammatsu 6355 PMT-Detector. The system was equipped with a Laser Science preamplifier head model 337973, containing circuitry to stretch short ns pulses to a 20 μs period so that less expensive electronic components could integrate the resulting waveform. Because of the long excited state lifetime of $Tb(acac)_3$, ($\tau \approx 1$ ms) this circuitry cannot function properly and was normally bypassed so that signals taken directly from the PMT could be digitally integrated. The exception was when checking possible laser scattering signals or the fluorescence of the Red 40 dye which exhibits ns pulse widths. Nanosecond signal intensities were

analyzed with a Laser Science pulse stretcher and analog gated integrator described in a later section.

1. *Digital integration method.*

When using the digital integration method, PMT signals were transferred on a double shielded (Belden 9273) cable to a Tektronix TDS-320 digitizing oscilloscope where digital conversion was internal to the scope via an 8 bit analog to digital converter (ADC). The digitized data were transferred to a Pentium computer by an 8-bit parallel ANSI/IEEE 488 (GPIB) communication port. The communication was controlled on the PC by custom National Instrument LabView software (6504 Bridge Point Parkway, Austin, TX 78703-5039).

A custom LabView Virtual Instrument (VI) named *Pulsed Emission Spectrometer* written by Dr. Giles Henderson was used to control the monochromator's wavelength scan motor, numerically integrate the digitized PMT signals, display the wavelength resolved emission spectrum and write the data to a user specified ASCII file. The VI's front panel is shown in Figure 17.

Figure 17: Front panel of *Pulsed Emission Spectrometer* VI.

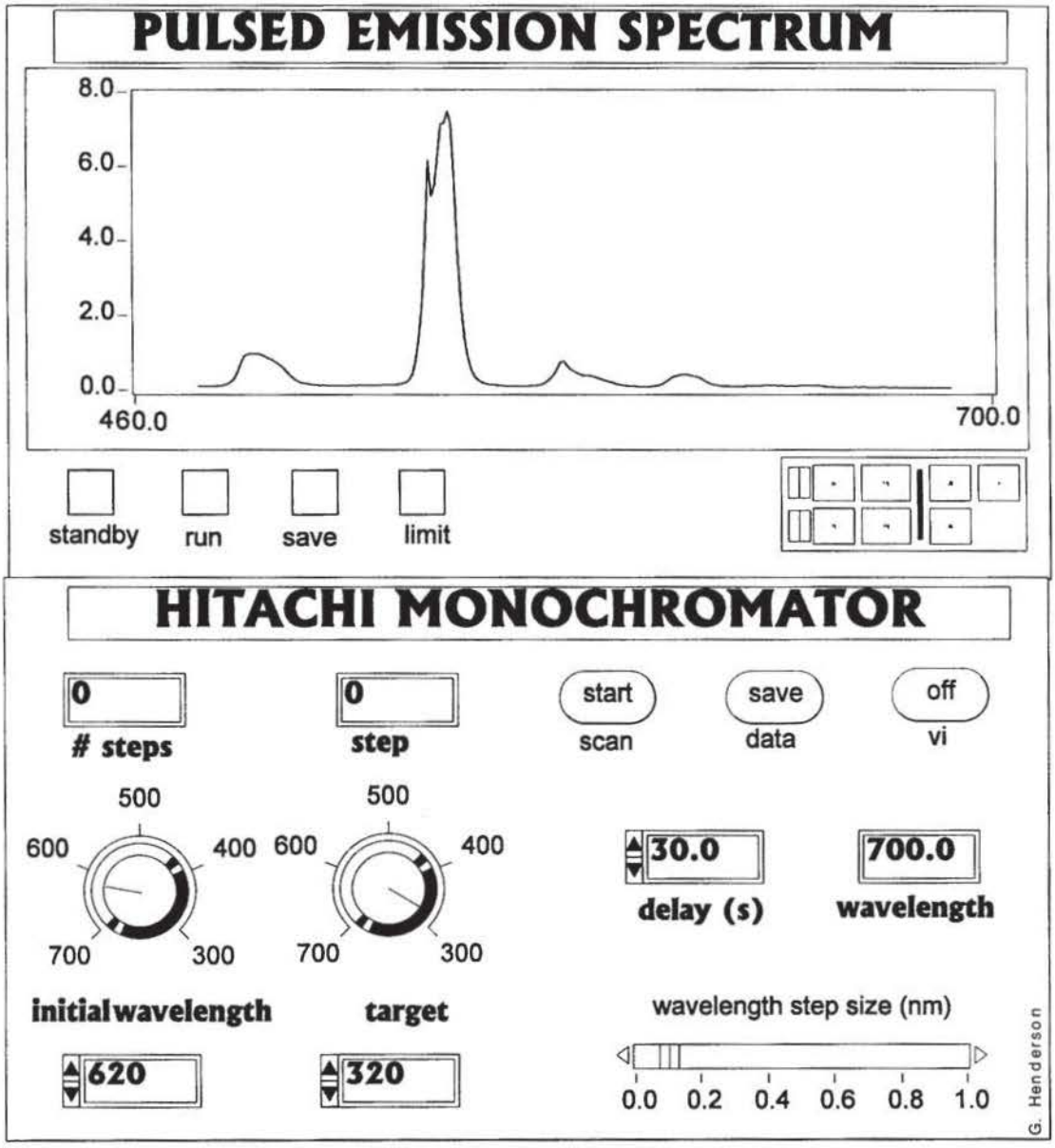

When using this configuration the laser was allowed to run in an internally triggered mode at approximately 20 Hz repetition rate (30 Hz. maximum).Triggering of the scope was from the trigger source on the laser and was routed to the scope's Y2 channel. The best trigger level was found to be -2 volts when using this source. As may be seen on the VI's front panel, the starting and ending wavelengths may be set. The initial wavelength

was manually set at the longest wavelength and the software steps the monochromator downward toward shorter wavelengths. The increments were specified by the "wavelength step size" control. During a scan the current wavelength value was shown on an indicator. If the data were to be saved this button was set before the start of the scan. The number of steps and current step are calculated and displayed when the spectrometer is started. The spectrum was generated one point at a time in which the x-coordinate of each point was determined from the optical encoder and the y-coordinate was determined from the integrated waveforms of a specified number of signal pulses.

The delay control was set to 8 seconds when using 1 nm steps. This 8 seconds included the time to transfer the data (perhaps .5 sec) and allow the NuDrive power supply to step the wavelength (3 seconds at 1 nm). The balance of the time allowed the scope to acquire and average 32 or 64 emission pulses. The TDS-320 oscilloscope has the ability to continually average from 2 to 256 successive signals selectable in 2^n steps. Vertical data cursors on the scope were used to select some portion of the displayed signal for subsequent integration. The VI software reads the signal between the data cursors and transfers it through the GPIB port. In this mode digital integration was done by the spectrometer software in a sub VI named *Read Tektronic Waveform and Integrate* using the trapezoidal rule to numerically integrate the digitized waveform. While longer delays and more averaging could be used, this configuration was a compromise between reasonable quality and the time needed to make the scan.

2. *Laser Science analog integration method.*

When integrating short ns waveforms the Laser Science analog gated integrator model 337971 was used. The corresponding VI used in this mode was named *LIF/Raman Spectrometer* and the front panel is shown in Figure 18.

Figure 18: Front Panel of *LIF/Raman Spectrometer* VI.

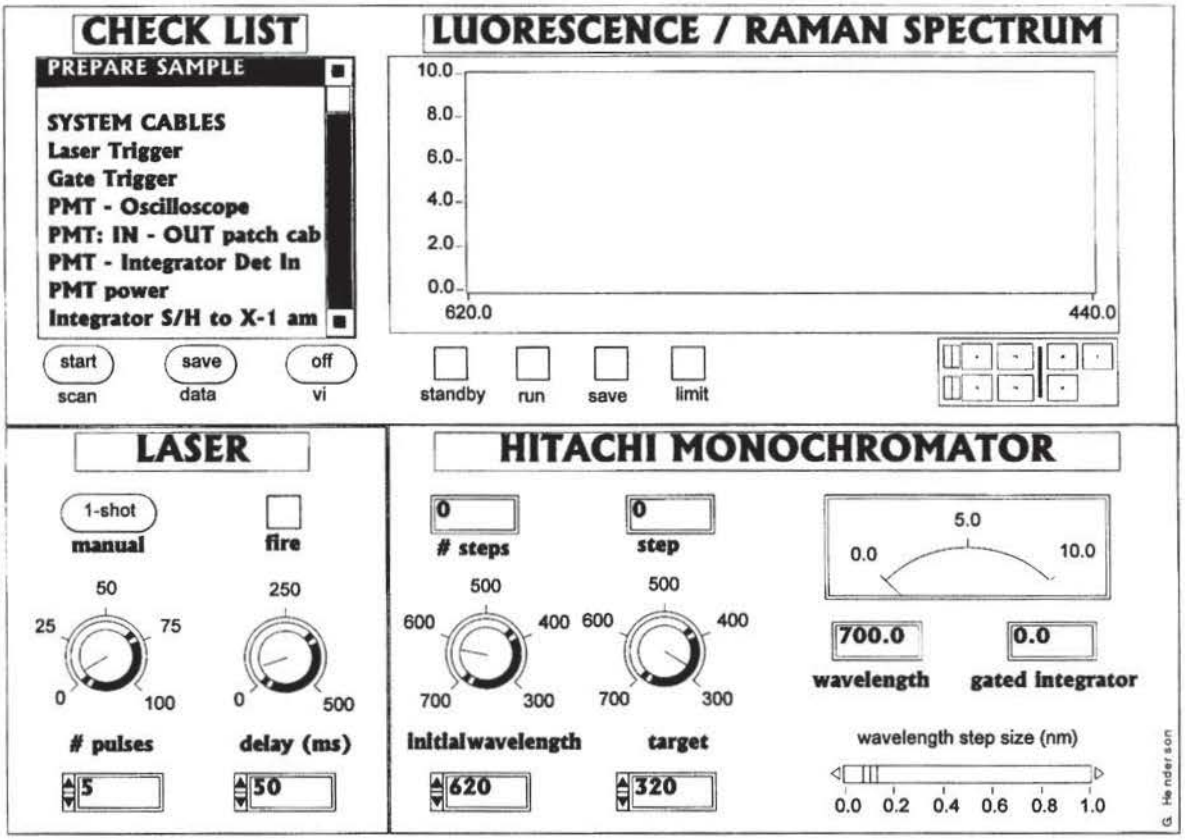

The wavelength was set up and controlled as described above. However, in this mode the laser was set to external triggering mode since the number of laser pulses at each wavelength must correspond to the number of gated integration intervals, normally 100. This was achieved by triggering each cycle of the laser and the gated integrator with a common computer generated trigger pulse. The PMT was wired to use the pulse stretching circuits. When the laser fires, the gated integrator receives the stretched signal and integrates a specified portion of it. The integrator adds up 100 pulses and then sends the total to the Lab-PC+ data acquisition board residing in an ISA slot on the pentium PC. The analog signal was then digitized on the board with a 12 bit ADC that was sign extended to 16 bits to fit the internal registers. The software then reads the digitized signal for the y axis coordinate and the optical encoder on the stepper motor for the x axis coordinate. In this

fashion the emission spectrum was generated and displayed one point at a time on the VI's strip chart. The wavelength step signal was then sent to the NuDrive power supply which increments the stepper motor. The software then fires another 100 trigger pulses and the process repeats.

III. Time Resolved Emission Spectra.

When time resolved spectra were collected the signal was taken from the PMT directly. It was transferred to the Tektronic scope through the Belden cable. A VI named *Read Tektronic Waveform* was used to capture the waveform through the GPIB port. This VI allows the entire waveform to be captured, or a selectable portion of the 1000 waveform data points or the data selected by user controlled data cursors may be read. The data for each time resolved profile was then written to a user specified ASCII file and subsequently analyzed with Axum (MathSoft, 101 Main St., Cambridge Mass.) and custom LabView software.

Figure 19: Setup for time resolved spectra. M are first surfaced mirrors and P is the PMT. The optical path is identical to Figure 16.

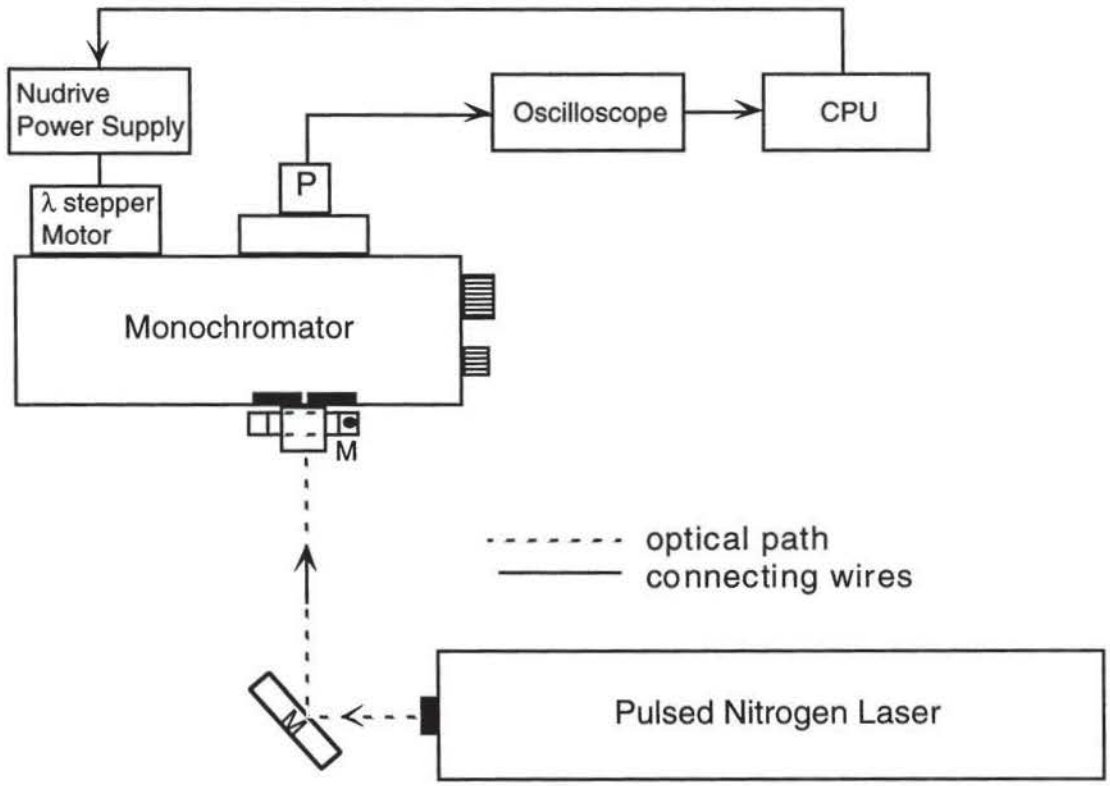

1. *RC time constant.*

Considerable care must be taken when observing time resolved signals since the equipment may create errors that have nothing to do with the real signal. The greatest source of error in time resolved profiles was the RC time constant of the cable. The PMT creates an output current that can be converted to a proportional voltage (IR) by passing it through a resistor. An equivalent circuit follows.

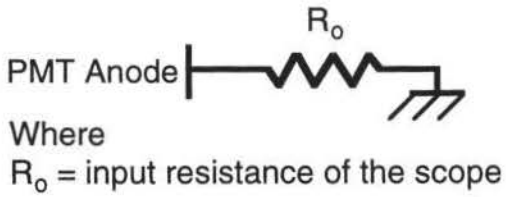

Since the input resistance of the oscilloscope was large (≈1 megaohm), a small current creates a measurable voltage in accordance with Ohm's law. This condition represents a reasonably high input resistance and loading of the PMT is negligible. However, if the current varies rapidly in time, the capacitance of the system becomes important as suggested by the following circuit.

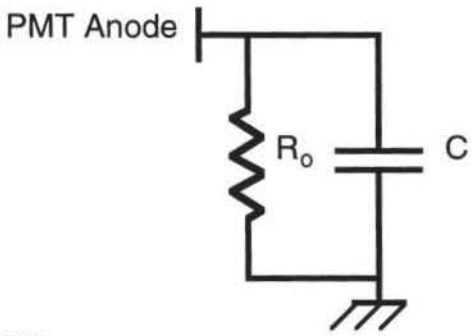

Where
R_o = input resistance of the scope (≈ 1MΩ)
C = capacitance of PMT + Cable + Scope

The capacitance of the cable was the most dramatic of these sources. When a current was applied and a voltage produced, these individual sources are charged and can decay only by discharge through R_o with an effective time constant $\tau = R_oC$. This capacitance distortion can be eliminated by providing a parallel resistance pathway which allows the circuit capacitance to discharge rapidly so that the decay of the signal is a true measure of the sample's excited state lifetime. In the present system an adapter gave a means of attaching an auxiliary resistor in parallel with the oscilloscope to ground as depicted in Figure 20.

Figure 20: Equivalent PMT to oscilloscope circuit with the auxiliary resistor R_T

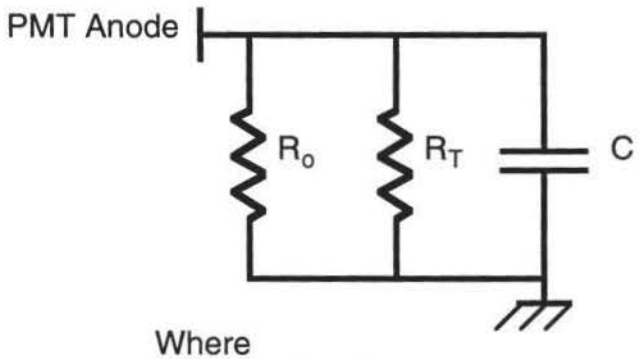

Where
R_o = input resistance of the scope
R_T = load resistance
C = capacitance of PMT + Cable + Scope

Demas (46) derives the following equation to analyze the effect of the detector circuit's time constant on an observed emission profile:

$$D(t) = \frac{I_o R}{(1-Z)} \exp\left(\frac{-t}{\tau}\right) - Z \exp\left(\frac{-t}{Z\tau}\right) \qquad (56)$$

$$Z = \frac{RC}{\tau} \qquad Z \neq 1$$

Here Z is the dimensionless ratio of the time constant to the sample lifetime, τ is the mean lifetime of the sample and I_o is the maximum PMT current.

Figure 21 shows a group of decay curves plotted using equation (56) to simulate the effect of RC distortion as the value of Z increases.

Figure 21: Decay curves plotted with increasing Z values. Curve **a** is an undistorted Z = 0 profile with an 800 μs lifetime. Curves **b-e** are Z = 0.25, 0.75, 1.5 and 2.0 respectively.

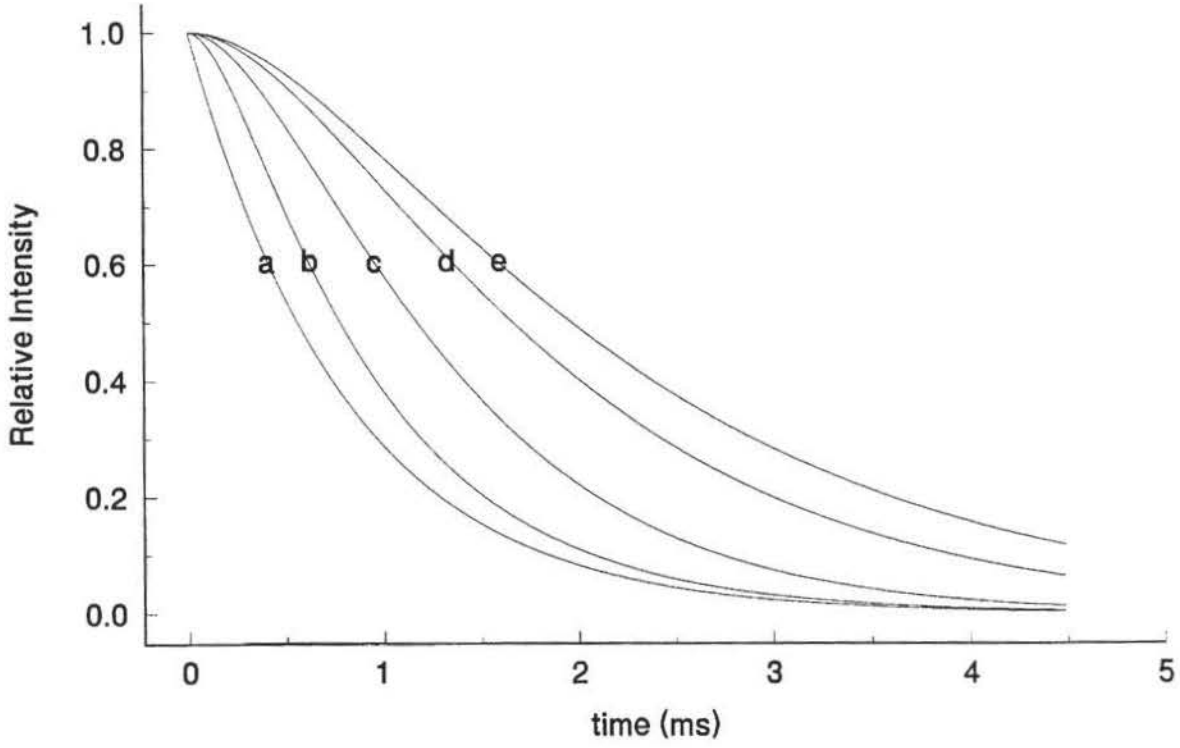

Excessive detector RC time constants cause nonexponential decays as is evident by their nonlinear semilogarithmic plots (curves **b-e** in Figure 22). Excited state lifetimes are determined from the slope of ln (i) vs time. Although the ln (i) plots exhibit exponential decay after a suitably long period, Figure 22 reveals a trend of increasing slopes and apparent lifetimes when Z-values increase. Indeed, data taken with large Z-values become a measure of the detector circuit's time constant rather than the sample's lifetime.

Figure 22: Conversion of Figure 21 to semilogarithmic plots. Assignments remain the same.

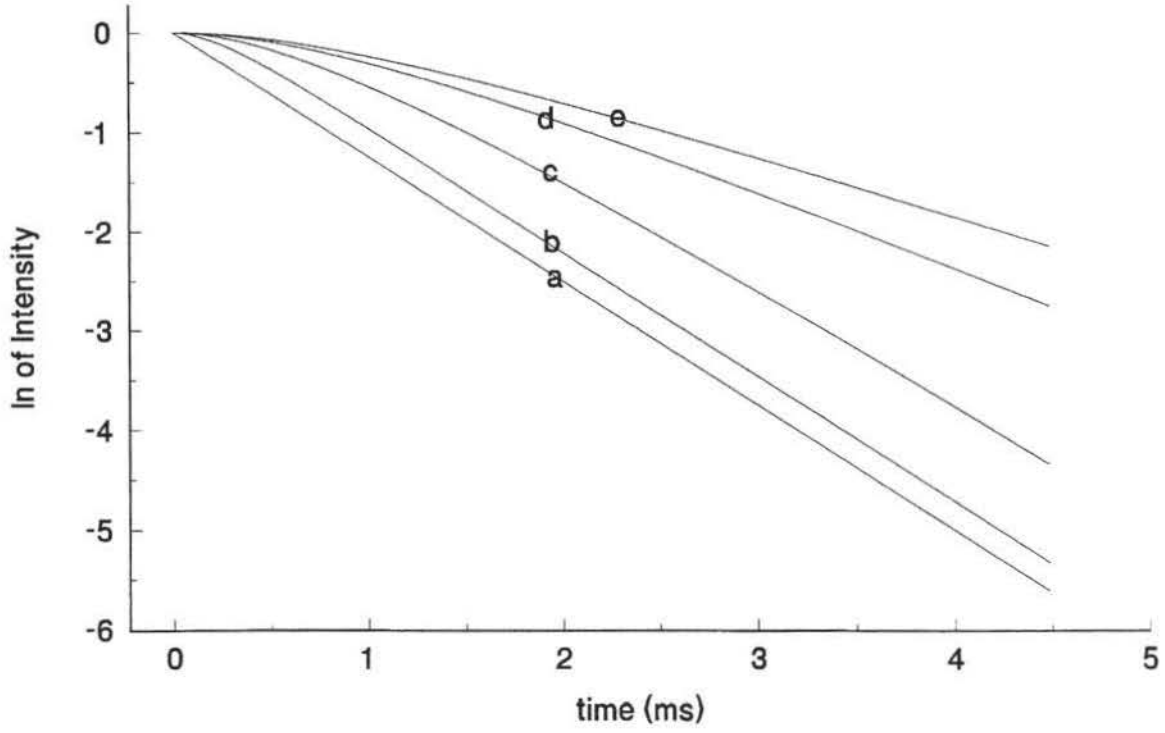

It is unfortunate that in order to reduce the RC time constant of the circuit to an acceptable level a 100 fold factor ($[R_o + R_T]/R_T$) in signal strength must be sacrificed. Table 2 is an example of peak signal using a typical PMT current.

Table 2: Signal loss as R_T and Z were reduced to lower the RC time constant where E = IR and I = 850 nanoamps.

R (ohms)	Peak signal voltage (millivolts)
1 meg	850
9100	8
50	0.4

As signals approach nanosecond pulse widths, reflected standing waves called ringing are created in the cable by terminal impedance mismatching. The rule at this point is

for the termination resistors to match the cable resistance. As may be seen in Table 2, most of the signal is then lost since 50 ohm cable requires 50 ohm terminating resistors.

A. *Characterization of the RC time constant.*

Time resolved luminescence profiles of $Tb(acac)_3$ samples of known excited state lifetime were measured and analyzed to determine the RC time constant and capacitance of the detector circuit and the photomultiplier current. Data were collected using resistor values of 1 MΩ and 9.2 KΩ (R_T in Figure 20). The effective parallel resistance of the oscilloscope (1 MΩ, R_o in Figure 20) with the terminal resistors of 1 MΩ and 9.2 KΩ gave $R_oR_T/(R_o + R_T)$ = 500 KΩ and 9.1 KΩ respectively. The resultant profiles are shown in Figure 23. The resistance limited capacitance discharge of the distorted profile produces a roll off at the start of decay and influences the curve for at least 100 μs.

Figure 23: Observed effect of RC Distortion on an exponential decay curve.

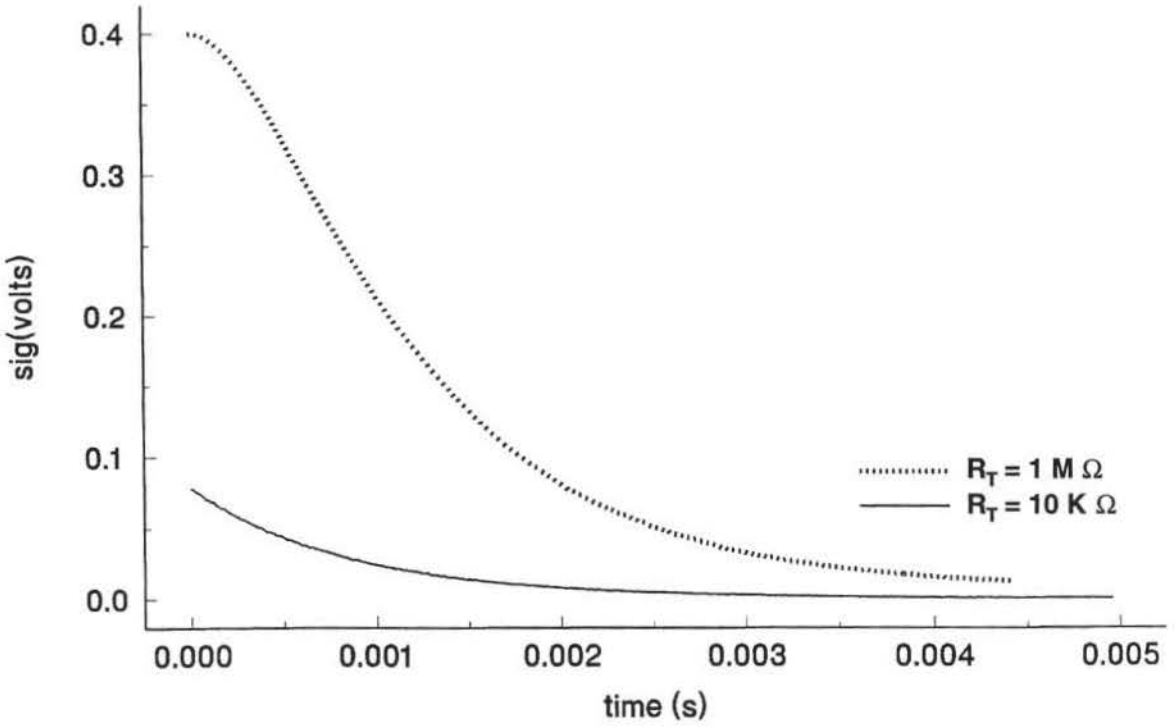

A LabView custom VI named *RC distortion* was used to analyze these profiles. This program uses equation (56) to calculate and display theoretical time resolved profiles on an interactive control panel (Figure 24). τ was set equal to the known excited state lifetime. R and R_2 controls were set to values consistent with the parallel $R_T + R_o$ resistance values of the terminating resistor. I, I_2 and Z were then adjusted to fit the theoretical profiles to the observed data.

Figure 24: Custom VI *RC Distortion* used to simulate theoretical distortions of an exponential decay.

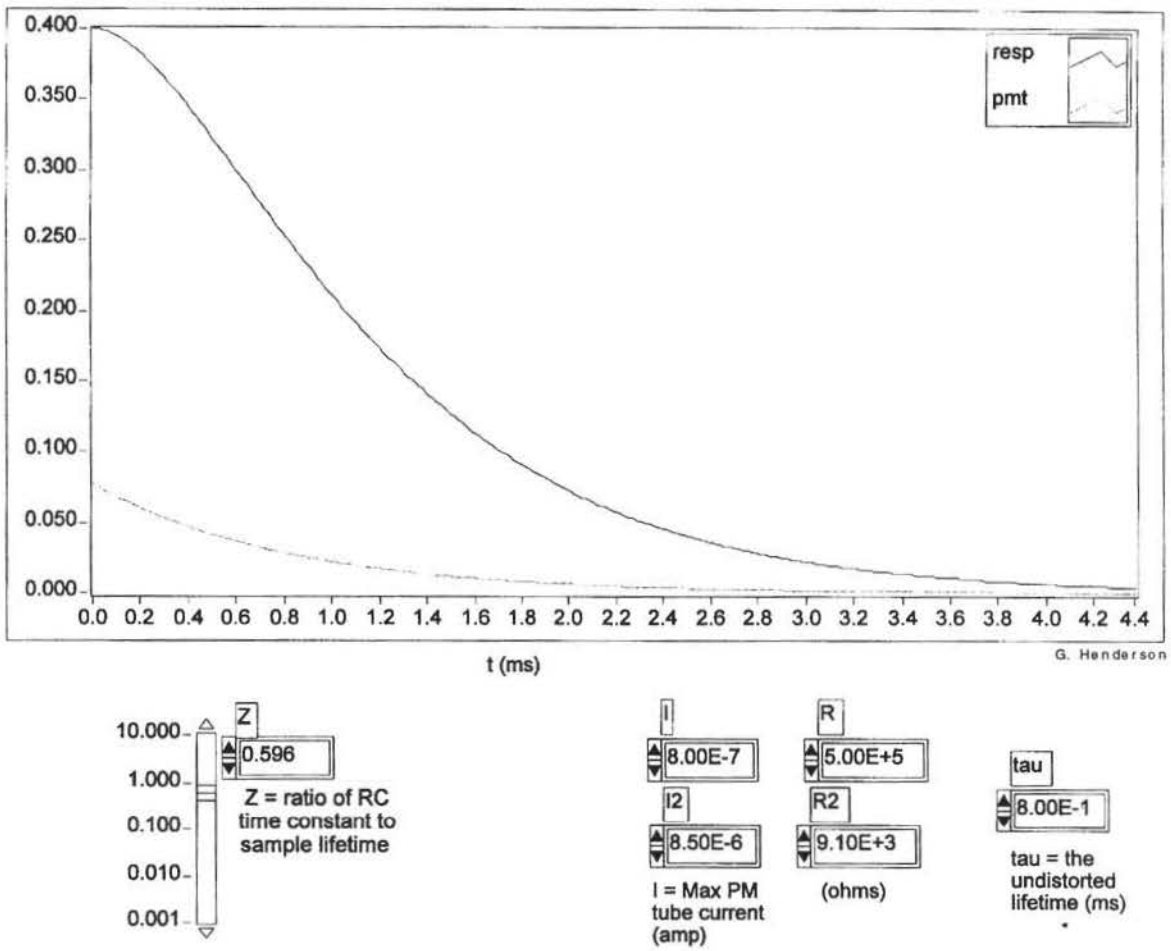

The analysis of the R_T = 1 MΩ profile gave a capacitance of 954 pf, and an RC time constant of 477 μs with Z = 0.6. This configuration seriously distorted the 800 μs lifetime decay. Analysis of the R_T = 9.1 KΩ profile gave an RC time constant of 8.7 μs and Z = 0.011. This configuration did not distort the 800 ms lifetime $Tb(acac)_3$ waveforms. With increasing quencher concentration the lifetime naturally decreases and results in a worst case of Z = 0.044, well below the Z = 0.35 Demas (47) considers to be a maximum acceptable limit.

B. *Useful RC time constants.*

In some circumstances the RC time constant of a detector circuit results in natural low pass filtering of a noisy signal. In the initial stages of this project the R value of 9.1K was increased to 26K to examine this effect. The apparent excited state lifetime changed approximately 1% and at that time it was considered the maximum usable value. Later when high concentrations of Red 40 in glycerol were used in this project, the prospect of using higher Z values was overlooked. In light of the earlier experiment it is possible that an increase to 20K ohms would have yielded better signal strength when it was needed without significant distortion in the waveform's decay time.

2. i_∞ *(dark current) correction.*

Another anomaly can occur when expected exponential decay data are naively converted to log plots. These plots are frequently nonlinear in that the tail of the plot curves upward. This deviation from exponential decay becomes increasingly more apparent as the signals become weaker. This behavior can result when a PMT has what is referred to as a dark current, due to stray light leaking through the monochromator, creating a small detector current flow, and a nonzero baseline. Shoemaker, et. al. (48) accommodates a dark current correction as:

$$\ln(i - i_\infty) = \ln i_o - t/\tau \qquad (57)$$

where: i is the signal intensity at time t
i_∞ is the signal intensity at time infinity (ideally zero)
i_o is the signal intensity at time zero.

A dark current correction must be made before a linear regression analysis is performed. Figure 25 demonstrates the results of i_∞ corrections for exponential and ln profiles.

Figure 25: Effects of i_∞ corrections on intensity (i) and ln(i) plots.

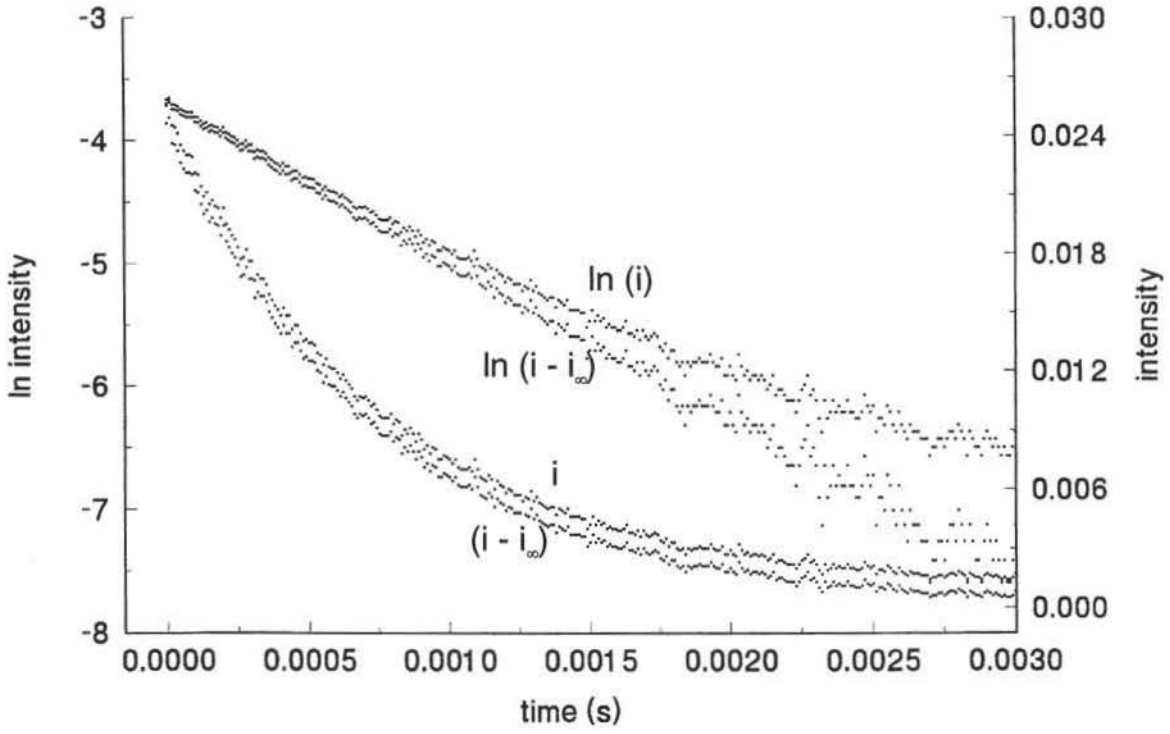

IV. Absorption.

Absorption measurements were performed on $Tb(acac)_3$, Red 40 and $Tb(acac)_3$ + Red 40 mixtures in ethanol with a Shimadzu UV-3100 controlled with UV-3100PC software running under Windows 3.1. Absorption spectra were used to determine whether any reaction may have occurred between $Tb(acac)_3$ and the quencher. This proved important in that an earlier quencher, tris (phenanthroline) iron(II) cation, was found to be reactive with $Tb(acac)_3$ (see Appendix B).

V. Conductivity.

All conductivity measurements were performed using deionized water and Red 40 dye with a Beckman model RC-18A conductivity bridge and a standard conductivity cell.

Data and Preliminary Results.

I. Spectral Properties of $Tb(acac)_3$-Red 40 System.

Figure 26 contains the luminescence emission spectrum of $Tb(acac)_3$ with assignments (See Figure 1). It is consistent with the published spectrum as noted in the Figure caption.

Figure 26: Laser induced emission spectrum of 8×10^{-4} M $Tb(acac)_3$ in ethanol with assignments from Dawson et. al. (49)

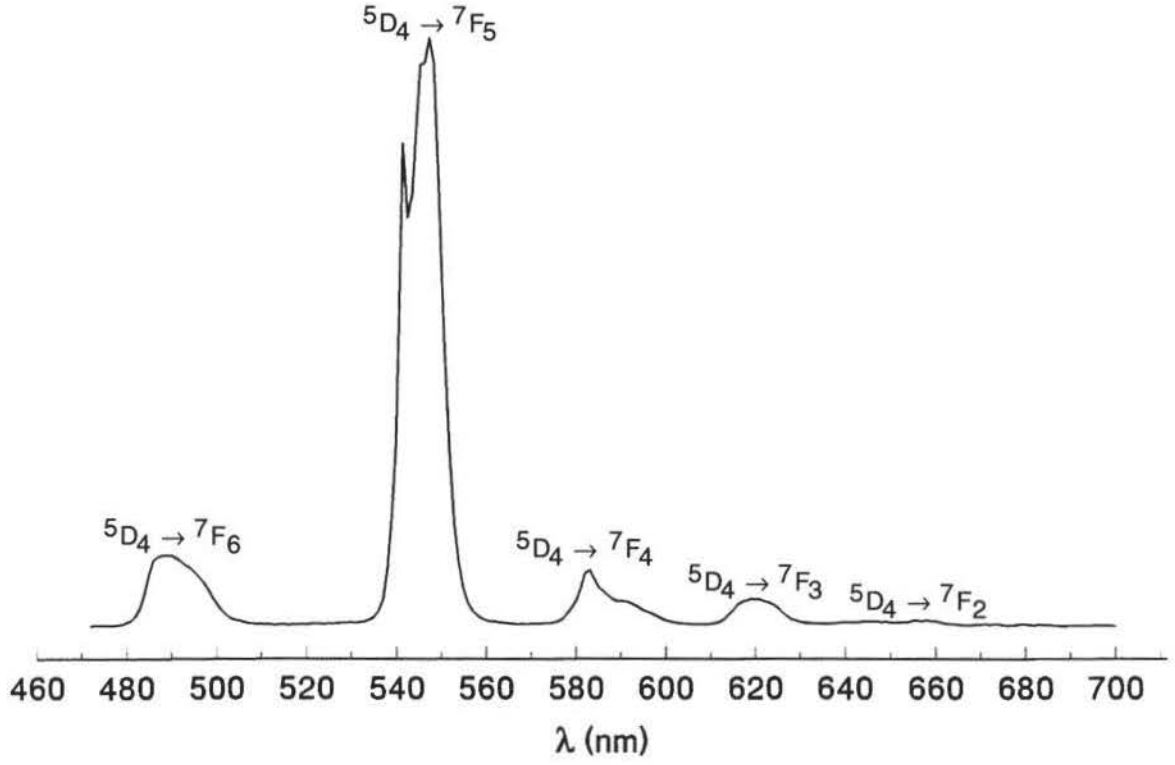

Figure 27 is an absorption spectrum of Red 40. It exhibits an intense absorption band in the green portion of the visible spectrum with $\lambda_{max} \approx 508$ nm. Since this absorption band favorably overlaps the $^5D_4 - {}^7F_5$ $Tb(acac)_3$ emission, Red 40 is a good candidate for both radiative and nonradiative quenching.

Figure 27: Absorption spectrum of 3.29×10^{-5} M Red 40 in ethanol.

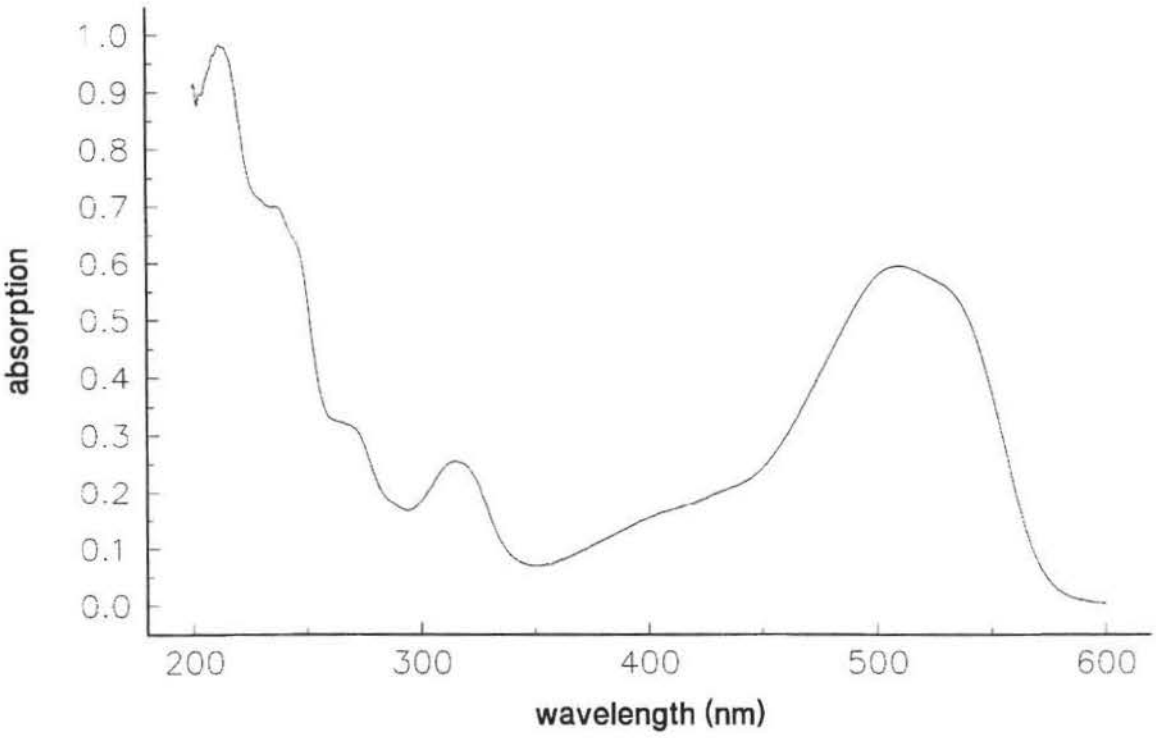

Figure 28 compares the absorption spectrum of a mixture of $Tb(acac)_3$ and Red 40. with the sum of the absorptions of their individual components. The coincidence of these spectra showed there was no combinational chemistry involved between these compounds.

Figure 28: Absorption spectrum of $Tb(acac)_3$ + Red 40 mixture vs. the sum of the individual spectra.

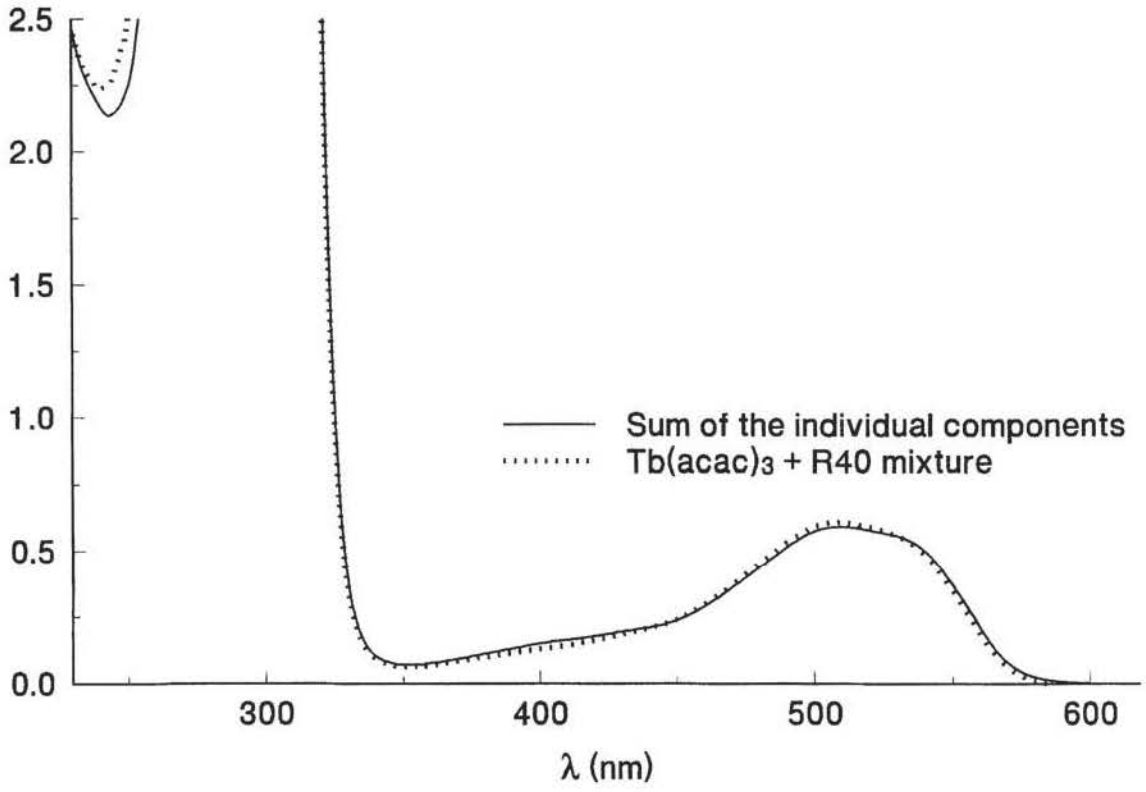

Figure 29 compares the nitrogen laser emission with the $Tb(acac)_3$ absorption spectrum. The coincidence of their wavelengths enables effective energy pumping.

Figure 29: Coincidence of the N_2 laser emission with $Tb(acac)_3$ absorption at 337.1 nm.

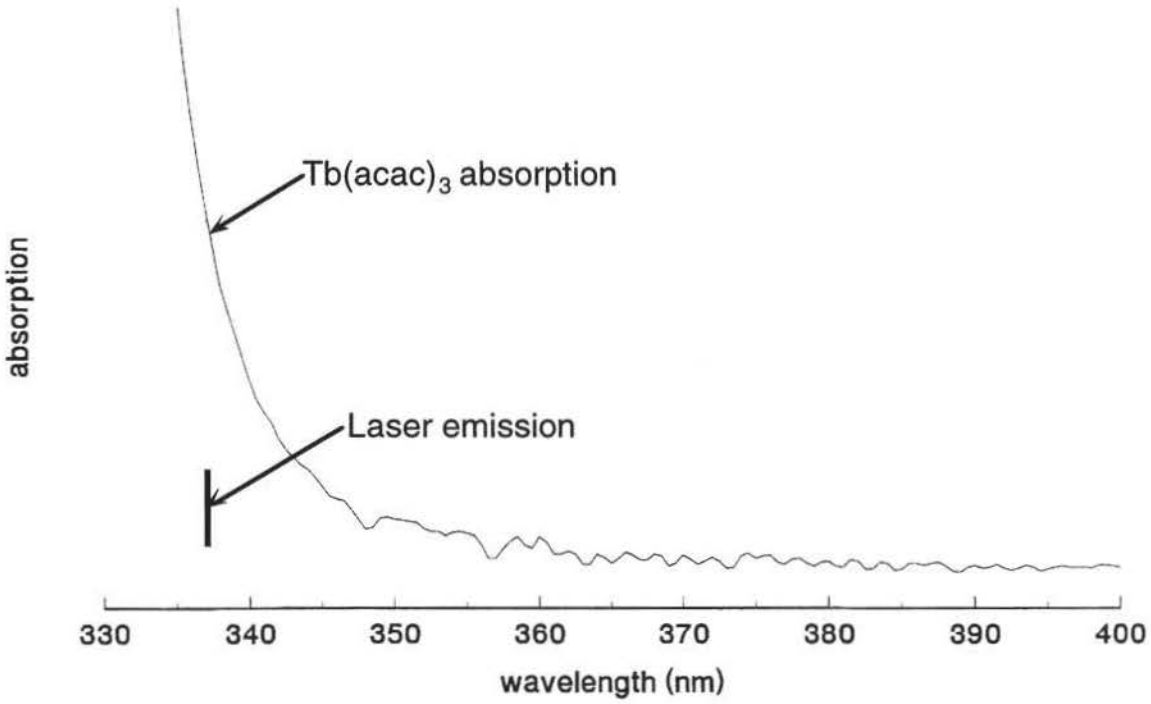

The $\langle f(\nu) \mid \varepsilon(\nu) \rangle$ overlap integrand in equation (21) is defined by the product of the normalized $Tb(acac)_3$ emission spectrum and the normalized Red 40 absorption spectrum as shown in Figure 30.

Figure 30: Overlap integrand of Red 40 absorption and $Tb(acac)_3$ emission.

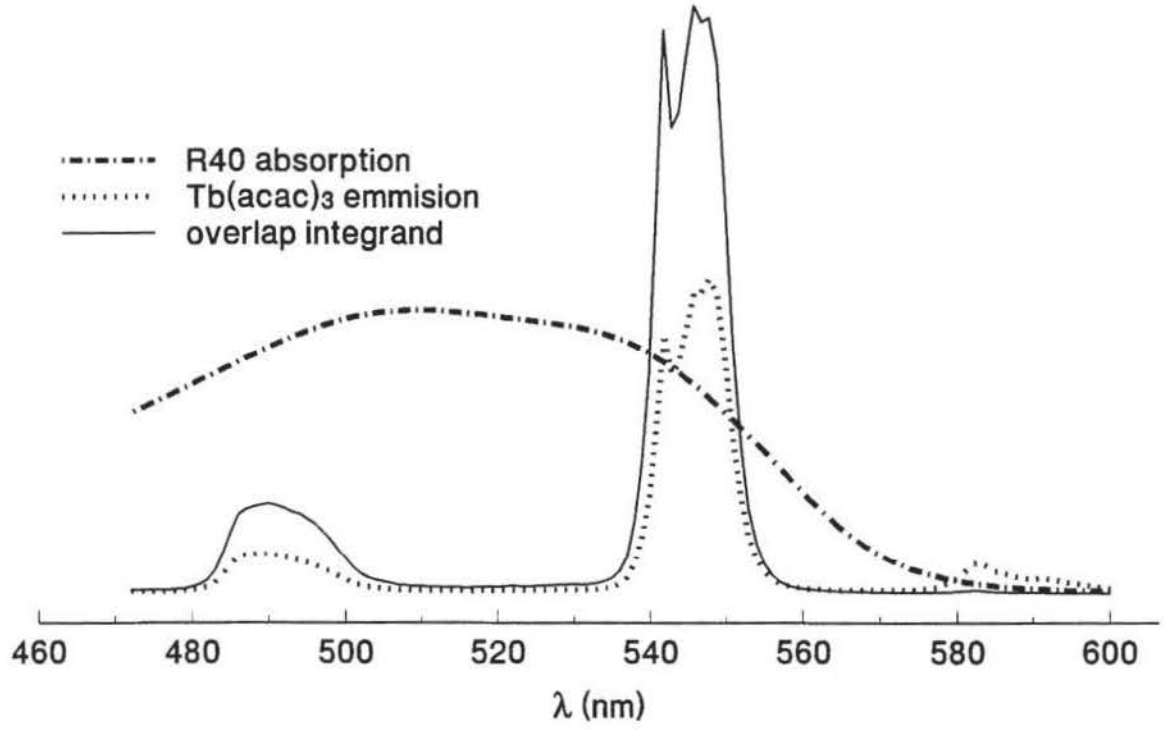

Figure 31 shows the emission spectrum of $Tb(acac)_3$ and $Tb(acac)_3$ with Red 40 at two radiative path lengths. The cuvette holder was mounted on a stage that could shift relative to the beam to adjust the radiative path lengths to approximately 2.5 and 7.5 mm.

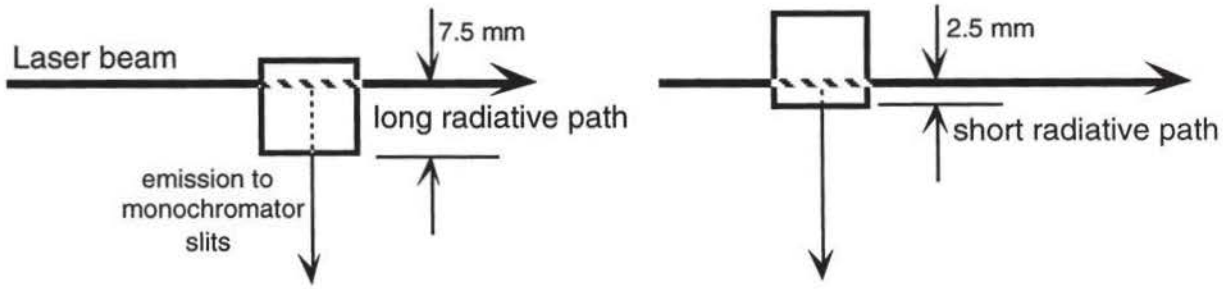

The radiative path length in other experiments was approximately 2.5 mm. The higher intensity spectrum in Figure 31 illustrates that there is no self-absorption in $Tb(acac)_3$. The lower intensity spectra illustrates that when Red 40 is added, path length dependent radiative quenching occurs. The difference in intensity of spectra may be explained with Beer's law (equation (7)).

Figure 31: Effect of radiative energy transfer. **a** and **b** are the long and short path lengths respectively for 7.5×10^{-4} M $Tb(acac)_3$ and no Red 40. **c** and **d** are the long and short path lengths of 7.5×10^{-4} M $Tb(acac)_3$ and 3.2×10^{-5} M Red 40.

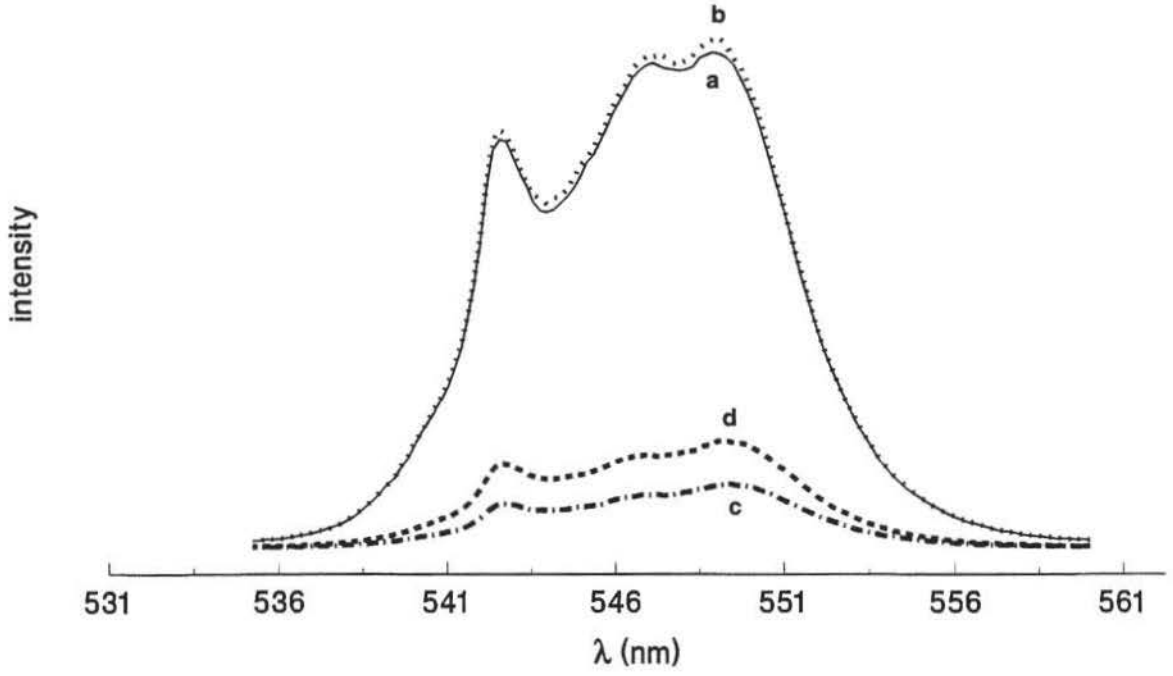

II. Time-Resolved Luminescence.

Tables 3 and 4 summarize the composition of the glycerol solutions used in this study.

Table 3: Run 1; Composition of glycerol solutions of 8.01(3) x 10^{-4} M $Tb(acac)_3$ with Red 40. Solutions are listed in order of increasing quencher concentration. Precision is expressed as a 68% confidence limit.

Solution	Molar Concentration (Red 40)	Ratio (Red 40/$Tb(acac)_3$)
1	0.0	0:1
2	$5.24 \pm .3 \times 10^{-5}$	0.07:1
3	$1.05 \pm .3 \times 10^{-4}$	0.1:1

Table 4: Run 2; Composition of glycerol solutions of 8.04(3) x 10^{-4} M $Tb(acac)_3$ with Red 40 in glycerol. Solutions are listed in order of increasing quencher concentration. Precision is expressed as a 68% confidence limit.

Solution	Molar Concentration (Red 40)	Ratio (Red 40/$Tb(acac)_3$)
1	0.0	0:1
2	$1.011 \pm .03 \times 10^{-4}$	0.1:1
3	$3.034 \pm .06 \times 10^{-4}$	0.4:1
4	$4.045 \pm .07 \times 10^{-4}$	0.5:1
5	$5.056 \pm .06 \times 10^{-4}$	0.6:1

Representative luminescence profiles measured in glycerol from both runs are shown in Figure 32.

Figure 32: Time resolved luminescence data measured in glycerol at 547 nm. Molar concentration of Red 40: **a** = 0.0, **b** = 2.513 x 10^{-5}, **c** = 5.235 x 10^{-5}, **d** = 1.047 x 10^{-4}, **e** = 3.034 x 10^{-4}.

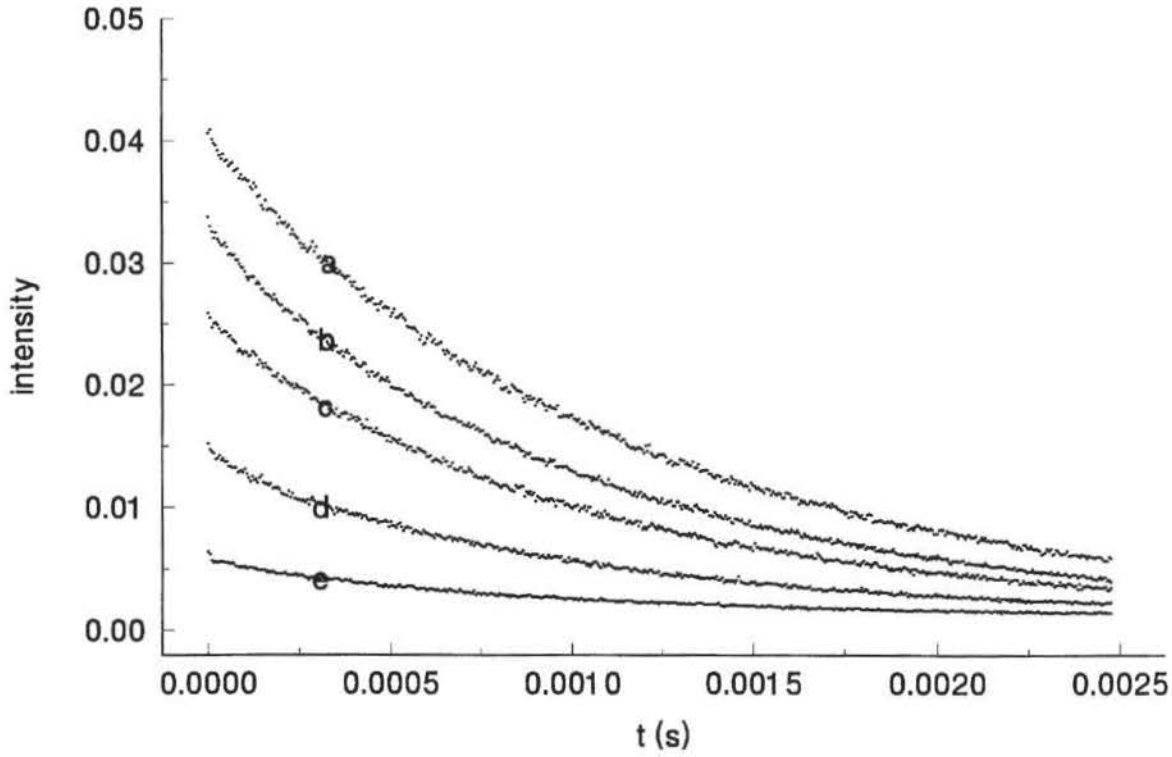

Tables 5 and 6 summarize the composition of the ethanol solutions used in this study.

Table 5: Run 1; Lifetimes of 7.56(3) x 10^{-4} M $Tb(acac)_3$ with Red 40 in ethanol. The precision is expressed as a 68% confidence limit.

Solution	Molar Concentration (Red 40)	Ratio (Red 40/$Tb(acac)_3$)	τ (μs) (5)
1	0.0	0:1	794 (τ_o)
2	2.47 ± .9 x 10^{-7}	0.0003:1	732
3	4.94 ± .2 x 10^{-7}	0.0007:1	682
4	9.87 ± .9 x 10^{-7}	0.001:1	623
5	1.97 ± .2 x 10^{-6}	0.003:1	569
6	2.96 ± .2 x 10^{-6}	0.004:1	514
7	9.87 ± .5 x 10^{-6}	0.013:1	344
8	1.68 ± .1 x 10^{-5}	0.022:1	255
9	2.37 ± .1 x 10^{-6}	0.031:1	202
10	3.06 ± .1 x 10^{-5}	0.04:1	184

Table 6: Run 2; Lifetimes of 8.09(3) x 10^{-4} M $Tb(acac)_3$ with Red 40 in ethanol. Solutions are listed in order of increasing quencher concentration. The precision is expressed as a 68% confidence limit.

Solution	Molar Concentration (Red 40)	Ratio (Red 40/$Tb(acac)_3$)	τ (μs) (5)
1 (a)	0.0	0:1	796 (τ_o)
2	2.42 ± .1 x 10^{-7}	0.0004:1	735
3	4.84 ± .3 x 10^{-7}	0.0006:1	697
4	7.74 ± .5 x 10^{-7}	0.0009:1	660
5	9.67 ± .9 x 10^{-7}	.001:1	634
6	2.90 ± .2 x 10^{-6}	0.004:1	529
7	9.67 ± .6 x 10^{-6}	0.01:1	330
8 (h)	2.32 ± .1 x 10^{-5}	0.03:1	199

A representative sample of the ethanol data from both runs is shown in Figure 33.

Figure 33: Time resolved luminescence profiles of $^5D_4$-$^7F_5$ $Tb(acac)_3$ measured at 547 nm an 0.8 mm slit width for run 2 in ethanol. Profiles shown are representative of both data sets. Molar concentration of Red 40: **a** = 0.0, **b** 2.4 x 10^{-7}, **c** = 4.8 x 10^{-7}, **d** = 7.7 x 10^{-7}, **e** = 9.6 x 10^{-7}, **f** = 2.9 x 10^{-6}, **g** = 9.6 x 10^{-6}, **h** = 2.3 x 10^{-5}.

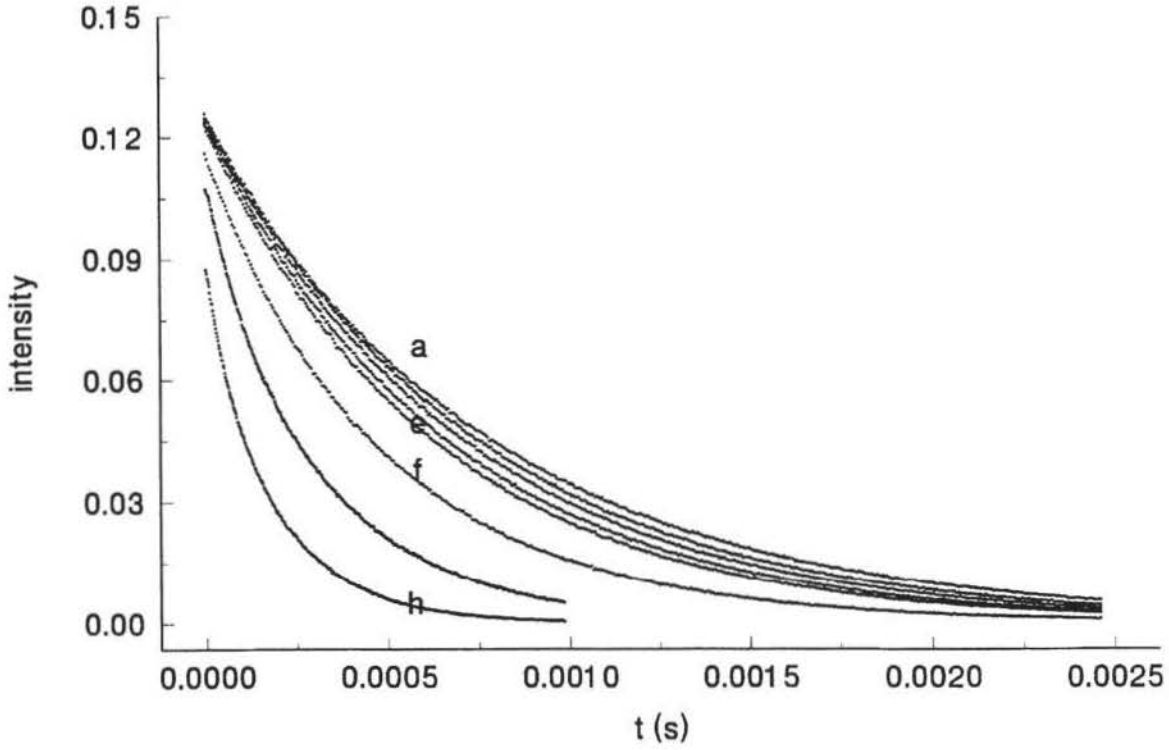

III. Electrical Conductivity.

Table 7 shows the results of conductivity measurements. This study helps depict the electrolytic behavior of Red 40 in solution.

Table 7: Conductivity data with calculated κ and Λ_m values.

[Red 40] M	Resistance in Ω	κ (Ω^{-1} cm^{-1})	Λ(Ω^{-1} cm^2 mol^{-1})
2.00×10^{-3}	421	2.855×10^{-3}	142.8
5.00×10^{-3}	1443	8.038×10^{-4}	160.8
1.25×10^{-3}	5320	2.303×10^{-4}	184.2
3.125×10^{-4}	19750	6.117×10^{-5}	195.7
1.031×10^{-4}	57700	2.083×10^{-5}	202.0

Data Treatment and Results.

I. Quenching Mechanism.

Table 1 summarizes the distinguishing features of the various quenching mechanisms. The results of the corresponding tests with $Tb(acac)_3$ and Red 40 are presented in Table 8.

Table 8: Results of various tests to characterize the $Tb(acac)_3$ + Red 40 quenching mechanism(s). Tb = $Tb(acac)_3$ and R40 = Red 40.

TEST CONDITION	OUTCOME
increased radiative path length	decreased intensity
effect of R40 on Tb^* lifetime	decreases τ
effect of R40 on Tb^* emission spectrum	decreased intensity
spectral changes upon mixing Tb and R40	no change
effect of increasing solvent viscosity	dynamic quenching persists

The absence of spectral changes upon mixing $Tb(acac)_3$ with Red 40 indicates that these compounds do not chemically react or form a ground state complex or an exciplex. Attenuation of the $Tb(acac)_3$ luminescence spectrum by increasing radiative path lengths confirms the role of static radiative quenching by the Red 40 dye. Moreover, dynamic quenching by resonance energy transfer is also indicated by the decrease in terbium's excited state lifetime in the presence of Red 40. Contact electron exchange can be ruled out as an important dynamic quenching mechanism since excited state lifetimes are diminished by Red 40 even in cold glycerol in which the donor and acceptor have no perceptible mobility during the radiation period.

II. Förster Resonance Energy Transfer in the Slow Diffusion Limit.

Quantitative studies were made in cold glycerol to determine τ_o, the excited state lifetime of $Tb(acac)_3$ in the absence of quencher and also determine the Förster critical radius of the Tb-Red 40 energy transfer in the absence of diffusion effects. The very high viscosity of cold glycerol (η = 12,110 cp. @ 0.0 °C (50)) prevents fluctuations in the distance between donors and acceptors during the radiative process (see appendix C). Time resolved luminescence is described under these conditions by equation (27). A custom LabView program was developed to evaluate and compare this function with experimental data. This program features a graphical user interface with interactive controls to define each of the parameters in equation (27) (see Figure 34).

Figure 34: *Förster Resonance Energy Transfer* VI. In this example the program displays both the experimental and calculated decay profiles of $Tb(acac)_3$ in the absence of Red 40.

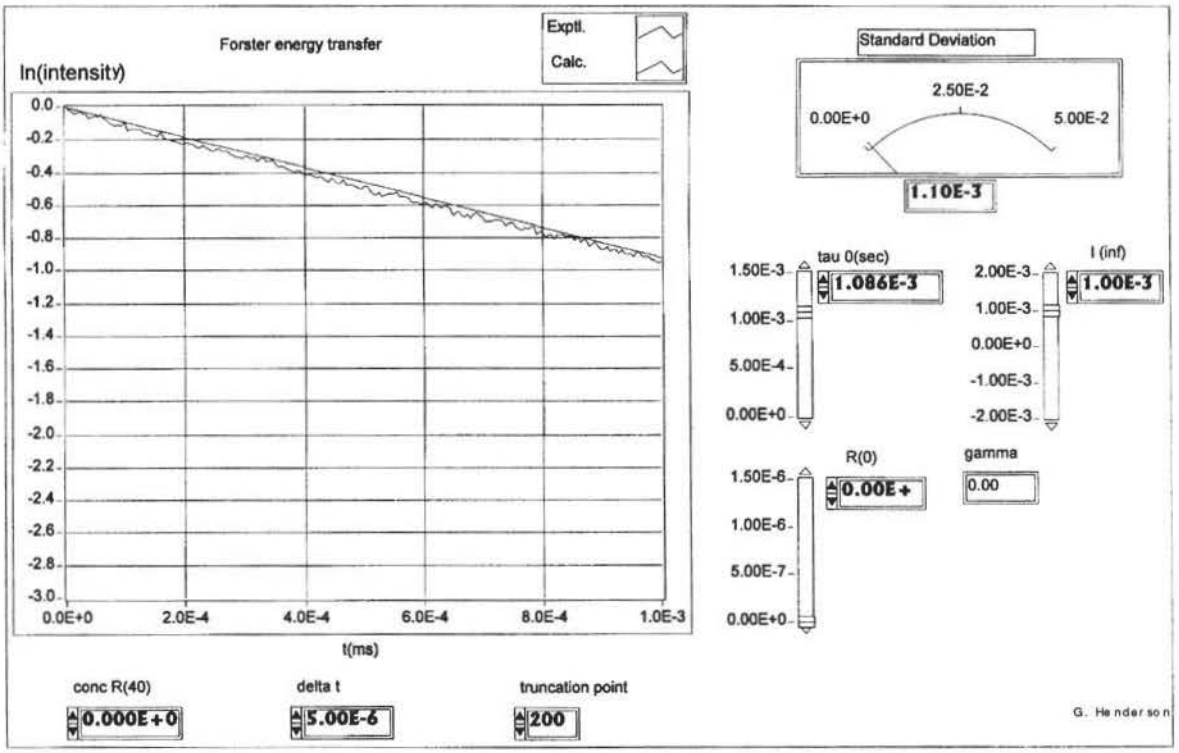

Decay data in the absence of quencher were first analyzed to determine τ_o. The τ_o control was adjusted to optimize the fit of the experimental data as indicated by a minimum standard deviation of the fit. This analysis gives an optimized τ_o = 1090(10) μs (glycerol), the same τ_o as that obtained from the slope of a least squares fit of ln intensity vs time.

Decay data for $Tb(acac)_3$ in cold glycerol solution with various concentrations of Red 40 were then analyzed using a fixed value of τ_o. Optimized fits of a representative data set are displayed in Figure 35.

Figure 35: Calculated and observed decay curves for $Tb(acac)_3$ and Red 40 in glycerol at 0 °C under Förster energy transfer quenching conditions. Molar Red 40 concentrations: **a** = 0.0 and **b** = 4.05×10^{-4}

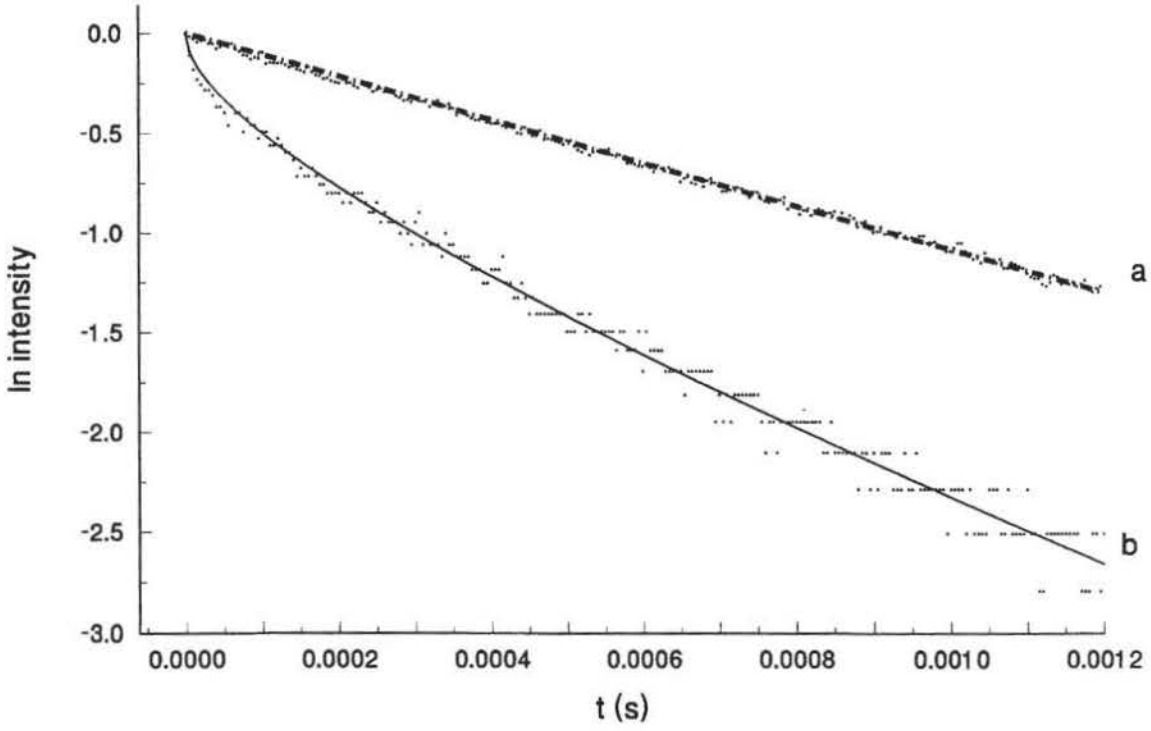

Due to radiative quenching, the intensity of each data set diminishes with increasing Red 40 concentration. In order to isolate the effects of nonradiative energy transfer each data set was scaled to a common relative intensity by dividing each intensity by the initial maximum intensity.

$$i_{rel} = \frac{i(t)}{i(t_o)} \qquad (58)$$

R_o was interactively adjusted to optimize the fit of these experimental decay profiles as seen in Figure 36.

Figure 36: Förster Energy Transfer VI front panel with 5.06 x 10^{-4} M Red 40 fit.

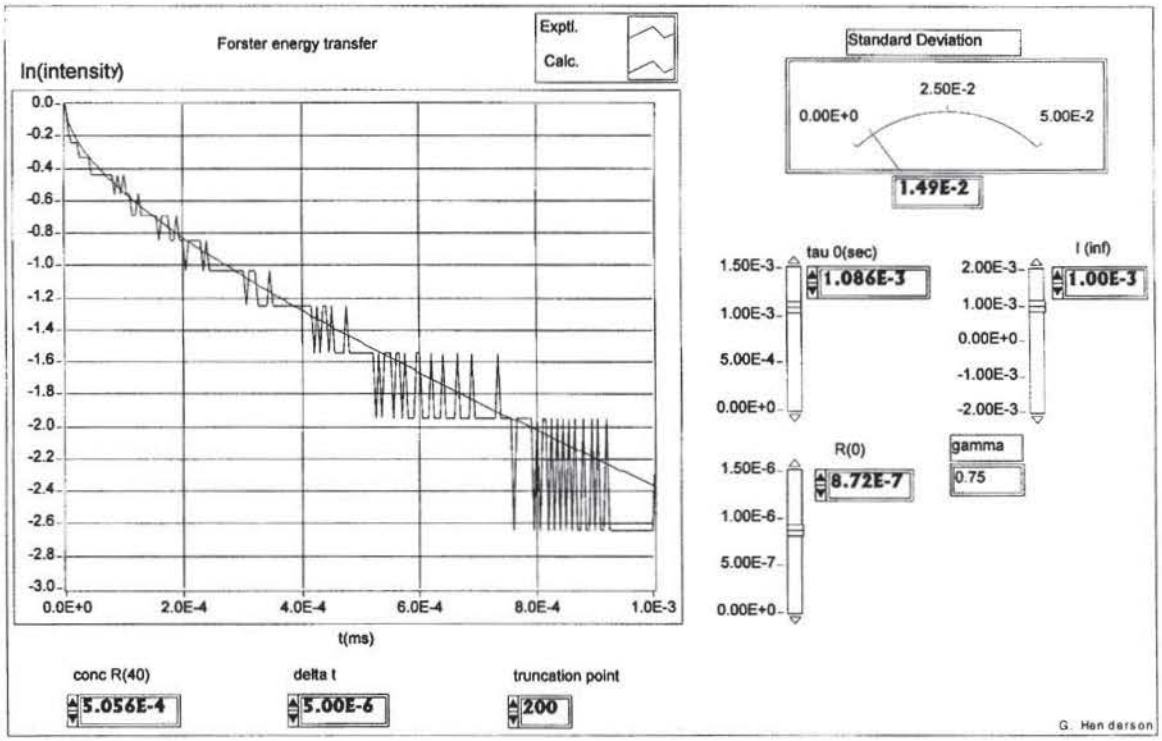

The program also calculated and displayed γ, the ratio of the concentration of Red 40 to the critical concentration of Red 40 defined in equation (28). A summary of these results and statistical analyses are presented in Tables 9 and 10. Precision limits on all results are expressed as ± standard deviation (68% confidence limits).

Table 9: Run 1; r_o values of 8.01(3) x 10^{-4} M $Tb(acac)_3$ with Red 40 in glycerol.

Molar Concentration (Red 40)	r_o (Å) ± 5
5.235 ± .06 x 10^{-5}	77.6
1.047 ± .06 x 10^{-4}	78.1

Table 10: Run 2; r_o values of 8.04(3) x 10^{-4} M $Tb(acac)_3$ with Red 40 in glycerol.

Molar Concentration (Red 40)	r_o (Å) ± 5
1.011 ± .03 x 10^{-4}	78.1
3.034 ± .06 x 10^{-4}	78.1
4.045 ± .07 x 10^{-4}	87.2
5.056 ± .06 x 10^{-4}	87.2

III. Quantum Efficiency in Glycerol.

Theoretical quantum efficiencies of radiationless dipole-dipole transfers which obey Förster kinetics can be calculated for given γ-values as described by equation (43). The integrated data sets used to find the experimental quantum efficiencies are shown in Figure 37.

These data sets were scaled to a common relative intensity as described by equation (58) to compensate for radiative quenching and changes in the monochromator slit width.

Figure 37: The i_∞ corrected data sets which were integrated for quantum efficiency calculations. The molar concentration of Red 40: **a** = 0.0, **b** = 5.24×10^{-5}, **c** = 1.05×10^{-4}, **d** = 5.06×10^{-4}.

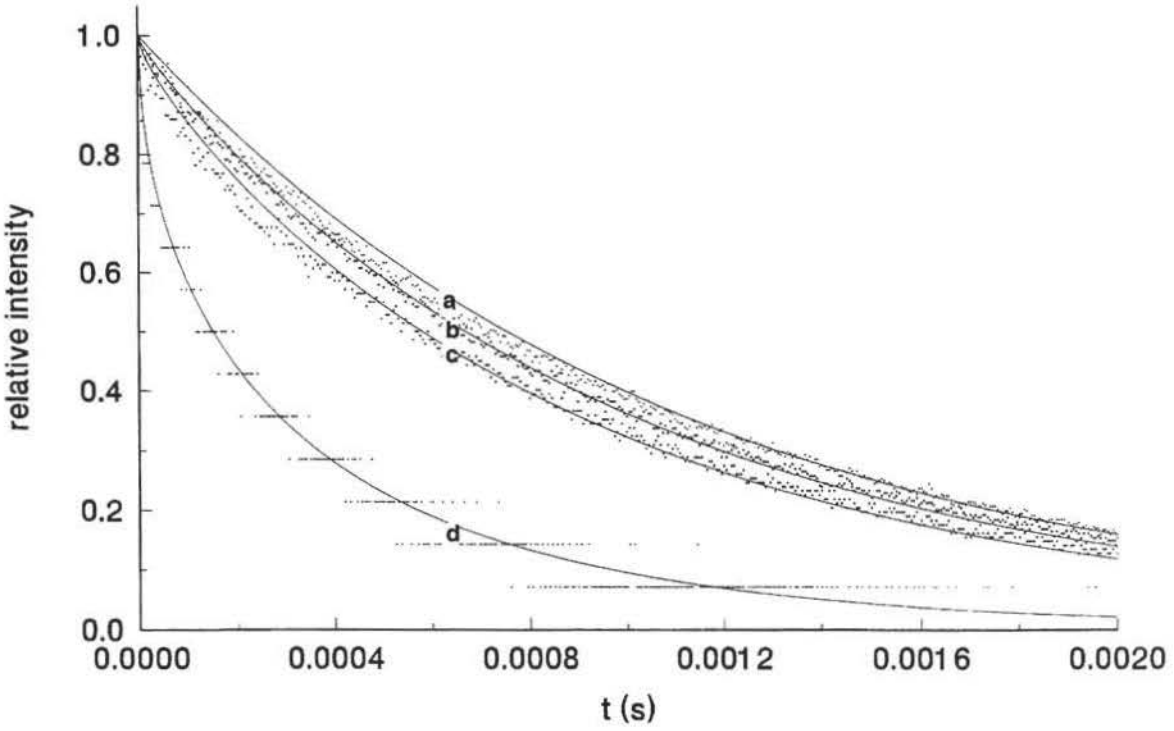

A comparison of theoretical quantum efficiencies of Förster energy transfer (equation (43)) with experimentally observed quantum efficiencies is presented Figure 38.

Figure 38: Quantum efficiency of Förster energy transfer.

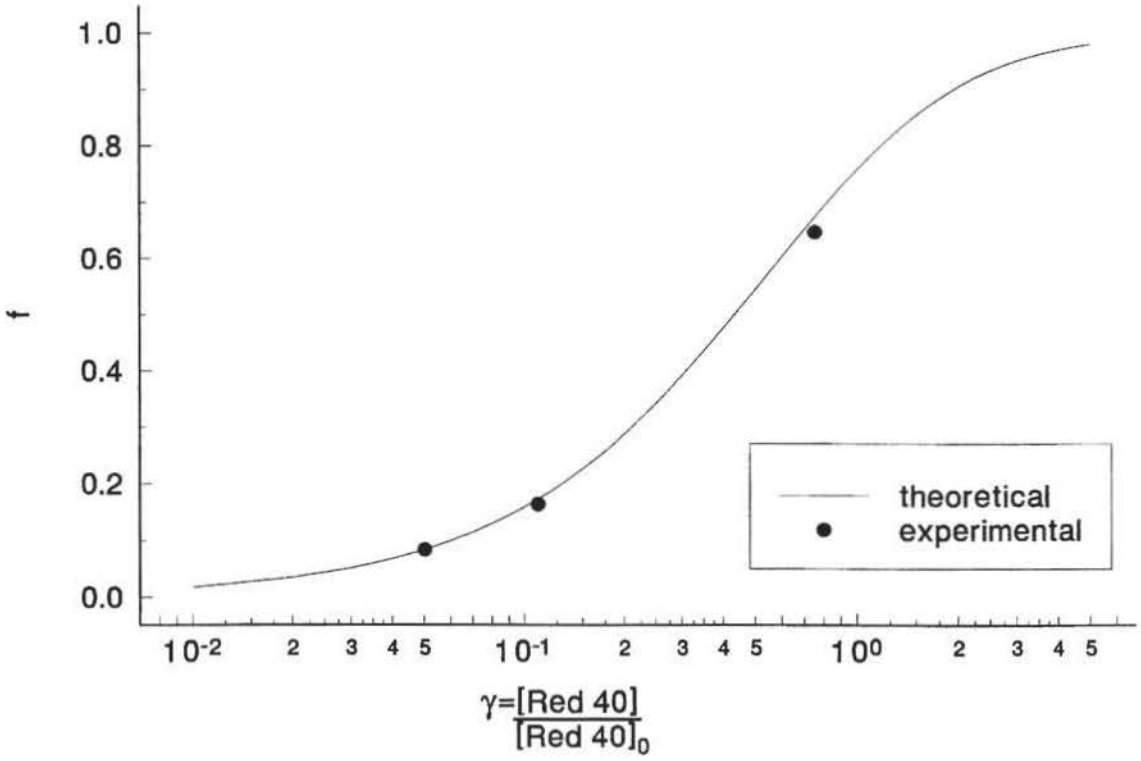

Table 11 lists experimentally observed values used in Figure 38.

Table 11: Experimental quantum efficiency data in glycerol.

[Red 40]	γ	$1 - \frac{f_{tb(acac)_3 + Red\ 40}}{f_{tb(acac)_3\ only}}$
$5.056 \pm .06 \times 10^{-4}$	$0.75 \pm .05$	.647
$1.047 \pm .06 \times 10^{-4}$	$0.11 \pm .007$	.164
$5.235 \pm .06 \times 10^{-5}$	$0.05 \pm .003$	.084

There was good agreement between the experimental points and the resonance energy transfer theory (26, 27). It is felt that any disagreement between theory and experiment is due to dilution errors and not to shortcomings in the theory.

IV. Diffusion Enhanced Förster Energy Transfer.

The theoretical diffusion enhanced energy transfer models (Equations 30 and 37) discussed above are characterized by three parameters: 1) r_o, the Förster critical quenching distance as defined by equation (25); 2) τ_o, the excited state lifetime in the absence of quencher and 3) D = D(Tb) + D(Red 40), the sum of the donor and acceptor diffusion coefficients. τ_o can be determined from the analysis of the exponential decay of the ethanol-$Tb(acac)_3$ solutions in the absence of Red 40. The time resolved $Tb(acac)_3$ emission profiles were analyzed with a custom LabView program designed to implement both the Voltz and Yokota-Tanimoto (YT) diffusion models. This program was tested using literature data (51). The program was first used to analyze $Tb(acac)_3$ profiles in the absence of Red 40 to determine τ_o = 796(5) μs, (Figure 39).

Figure 39: LabView VI, being used to find τ_o for the series. The quality of the fit makes the calculated line difficult to see in the experimental data.

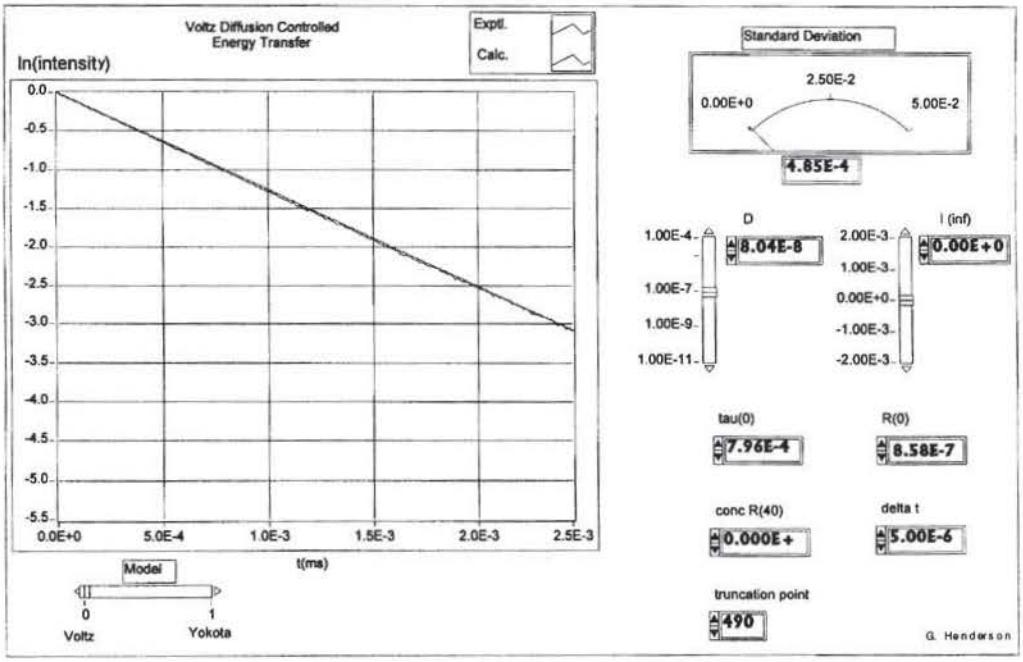

Using appropriate values of the index of refraction[c] , the value of r_o in ethanol can be calculated from the value of r_o measured in glycerol: $r_o(alc) = r_o(gly)\ [\eta(gly) / \eta(alc)]^{2/3}$.

$$r_o(alc) = 8.11 \times 10^{-7} \quad \left(\frac{1.4796}{1.3611}\right)^{2/3} = 8.58 \times 10^{-7} \text{ cm.} \qquad (59)$$

The r_o and τ_o parameters were then fixed at these values and the diffusion coefficient control of the VI was interactively adjusted to minimize the standard deviation of the selected theoretical model from the observed profile. Both the Voltz and the YT models were used in this manner to determine diffusion coefficients for various concentrations of Red 40. A representative fit is shown in Figure 40.

---

[c] The refractive index of glycerol at 0 °C can be found from its molar refractivity and density at 20 °C using: $\Re = (\eta^2-1) / (\eta^2+2) * M/d$ (52), where η is the refractive index, M is the molecular weight and d is the density of glycerol. Since $\Re$ depends only on the sample's polarizability, α_o (where $\Re = 4\pi N / 3 * \alpha_o$ = constant), the equation may be solved for η using the density of glycerol at 0 °C.

Figure 40: LabView VI, set to fit the Yokota-Tanimoto intermediate diffusion energy transfer model.

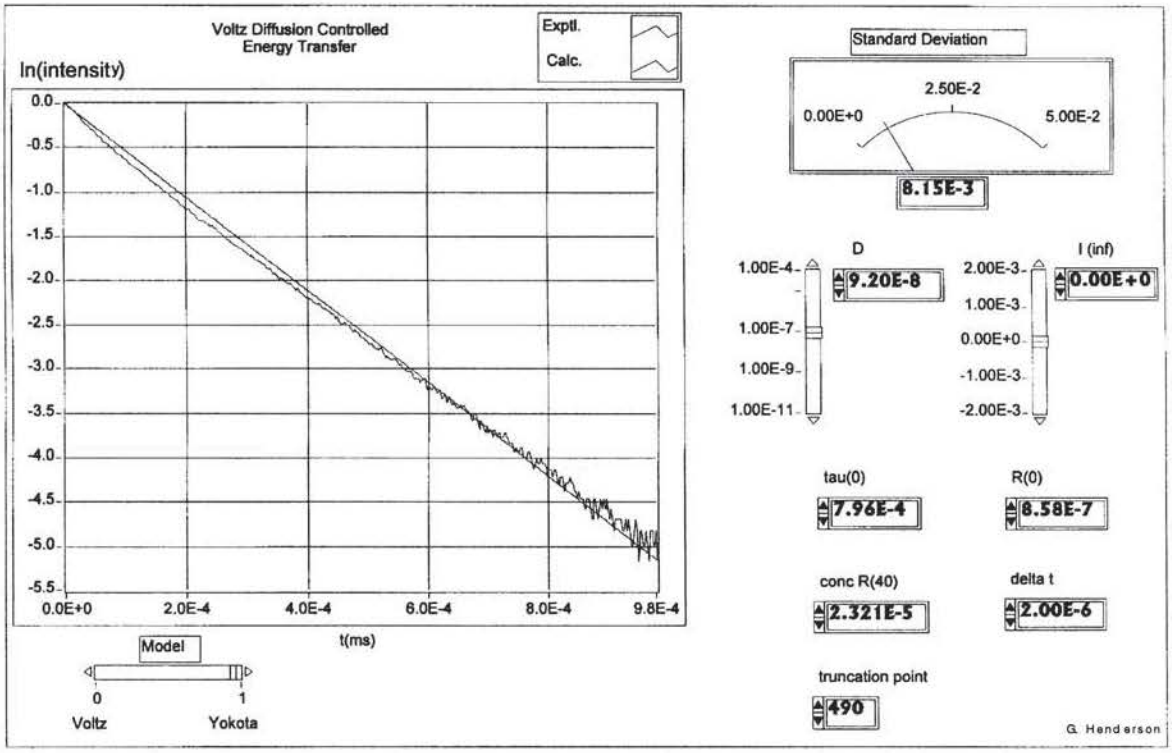

Figure 41 is a representative sample of calculated YT fits for a family of experimental data.

Figure 41: Intensity decay plots of experimental and calculated fits using the Yokota-Tanimoto intermediate diffusion energy transfer model. The $Tb(acac)_3$ is 8.099×10^{-4} M and was monitored at λ = 548 nm and 0.6 mm slit width. Molar concentrations of Red 40 were: **a** = 0.0, **b** = 2.4×10^{-7}, **c** = 7.7×10^{-7}, **d** = 2.9×10^{-7}, **e** = 9.6×10^{-6}, **f** = 2.3×10^{-5}.

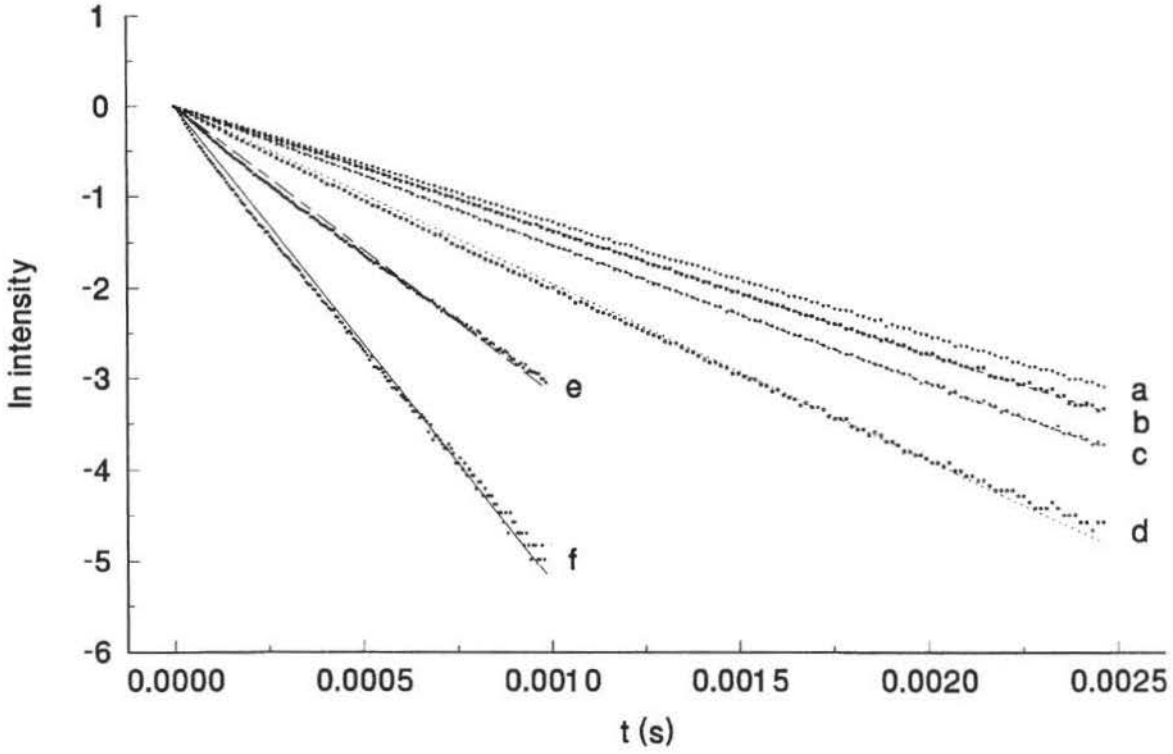

Diffusion coefficients obtained from the YT analysis are summarized in Tables 12 and 13.

Table 12: Run 1 diffusion coefficients from the Yokota-Tanimoto intermediate diffusion energy transfer model.

Solution	Molar Concentration (Red 40)	Diffusion Coefficient (cm^2/s) Yokota-Tanimoto model $\pm (0.1 \times 10^{-8})$
1	0.0	0.0
2	$2.47 \pm .9 \times 10^{-7}$	3.44×10^{-7}
3	$4.94 \pm .2 \times 10^{-7}$	3.15×10^{-7}
4	$9.87 \pm .9 \times 10^{-7}$	2.26×10^{-7}
5	$1.97 \pm .2 \times 10^{-6}$	1.51×10^{-7}
6	$2.96 \pm .2 \times 10^{-6}$	1.40×10^{-7}
7	$9.87 \pm .5 \times 10^{-6}$	9.68×10^{-8}
8	$1.68 \pm .1 \times 10^{-5}$	8.88×10^{-8}
9	$2.37 \pm .1 \times 10^{-6}$	8.08×10^{-8}
10	$3.06 \pm .1 \times 10^{-5}$	7.78×10^{-8}

Table 13: Run 2 diffusion coefficients from the Yokota-Tanimoto intermediate diffusion energy transfer model. Letters denote fitted profile in Figure 41.

Solution	Molar Concentration (Red 40)	Diffusion Coefficient (cm^2/s) Yokota-Tanimoto model $\pm (0.1 \times 10^{-8})$
1 (**a**)	0.0	0.0
2(**b**)	$2.42 \pm .1 \times 10^{-7}$	3.37×10^{-7}
3	$4.84 \pm .3 \times 10^{-7}$	2.53×10^{-7}
4(**c**)	$7.74 \pm .5 \times 10^{-7}$	2.35×10^{-7}
5	$9.67 \pm .9 \times 10^{-7}$	2.33×10^{-7}
6(**d**)	$2.90 \pm .2 \times 10^{-6}$	1.39×10^{-7}
7(**e**)	$9.67 \pm .6 \times 10^{-6}$	1.07×10^{-7}
8 (**f**)	$2.32 \pm .1 \times 10^{-5}$	9.10×10^{-8}

A corresponding analysis of the $Tb(acac)_3$ decay profiles was carried out using the Voltz diffusion model as depicted in Figures 42 and 43. Figure 42 is a representative fit using the Voltz model.

Figure 42: LabView VI, used to fit the Voltz intermediate diffusion energy transfer model.

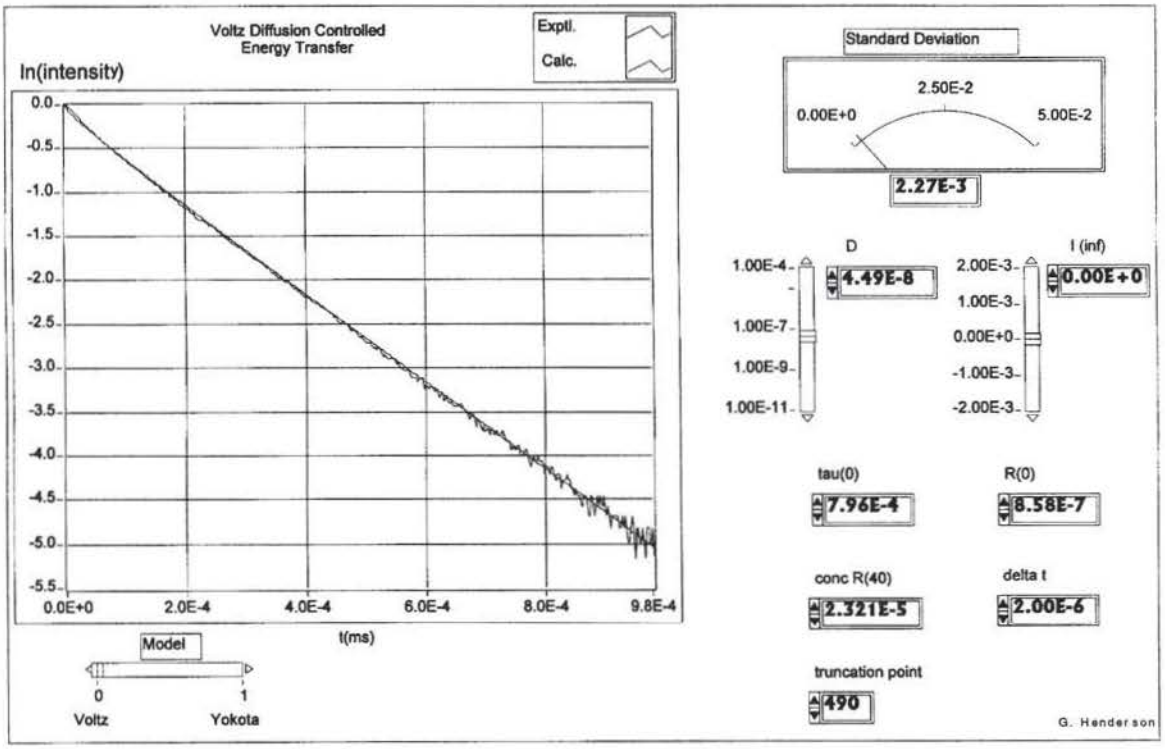

Figure 43 is a representative sample of calculated Voltz fits for a family of experimental data.

Figure 43: Intensity decay plots of experimental and calculated fits using the Voltz intermediate diffusion energy transfer model. $Tb(acac)_3$ is 8.09×10^{-4} M and was monitored at λ = 548 nm and 0.6 mm slit width. Molar concentrations of Red 40 were: **a** = 0.0, **b** = 2.4×10^{-7}, **c** = 7.7×10^{-7}, **d** = 2.9×10^{-7}, **e** = 9.6×10^{-6}, **f** = 2.3×10^{-5}.

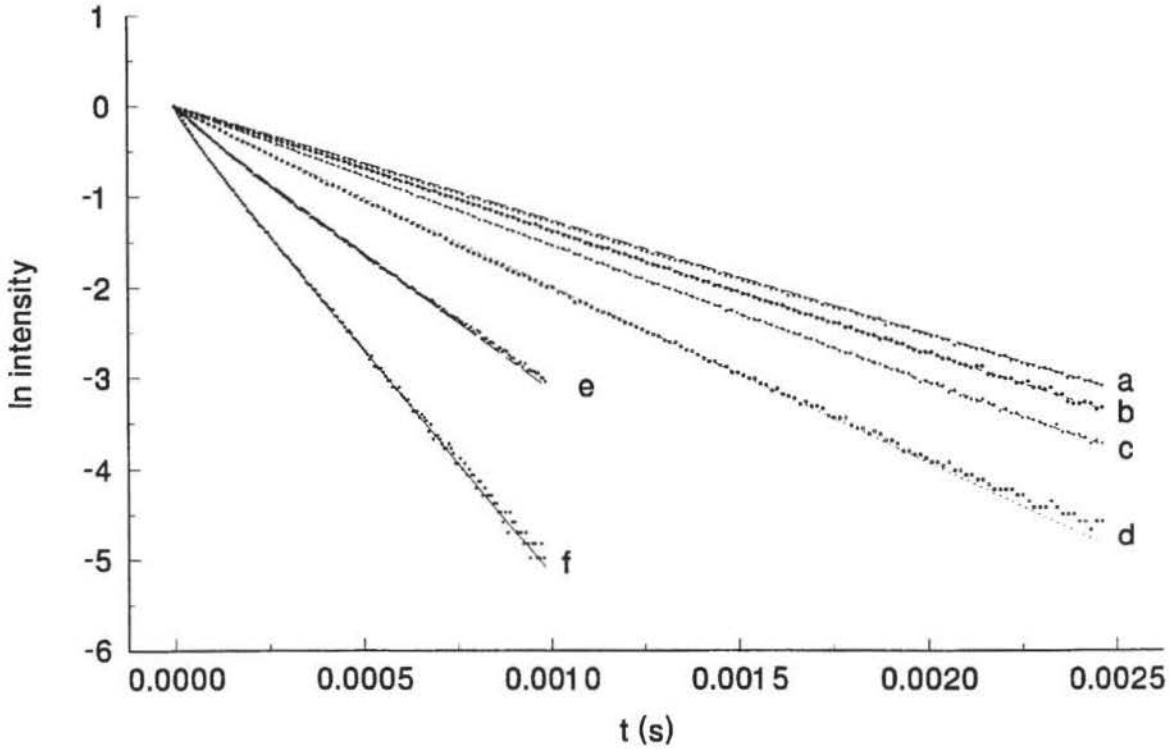

Diffusion coefficients obtained from the Voltz analysis are summarized in Tables 14 and 15

Table 14: Run 1 diffusion coefficients from the Voltz intermediate diffusion energy transfer model.

Solution	Molar Concentration (Red 40)	Diffusion Coefficient (cm^2/s) Voltz model $\pm (0.1 \times 10^{-8})$
1	0.0	0.0
2	$2.47 \pm .9 \times 10^{-7}$	1.35×10^{-7}
3	$4.94 \pm .2 \times 10^{-7}$	1.25×10^{-7}

4	$9.87 \pm .9 \times 10^{-7}$	8.90×10^{-8}
5	$1.97 \pm .2 \times 10^{-6}$	7.90×10^{-8}
6	$2.96 \pm .2 \times 10^{-6}$	6.79×10^{-8}
7	$9.87 \pm .5 \times 10^{-6}$	4.89×10^{-8}
8	$1.68 \pm .1 \times 10^{-5}$	4.49×10^{-8}
9	$2.37 \pm .1 \times 10^{-6}$	4.19×10^{-8}
10	$3.06 \pm .1 \times 10^{-5}$	3.99×10^{-8}

Table 15: Run 2 diffusion coefficients from the Voltz intermediate diffusion energy transfer model. Letters denote fitted profile in Figure 43.

Solution	Molar Concentration (Red 40)	Diffusion Coefficient (cm^2/s) Voltz model $\pm (0.1 \times 10^{-8})$
1 (**a**)	0.0	0.0
2(**b**)	$2.42 \pm .1 \times 10^{-7}$	1.31×10^{-7}
3	$4.84 \pm .3 \times 10^{-7}$	1.06×10^{-7}
4(**c**)	$7.74 \pm .5 \times 10^{-7}$	9.90×10^{-7}
5	$9.67 \pm .9 \times 10^{-7}$	9.90×10^{-7}
6(**d**)	$2.90 \pm .2 \times 10^{-6}$	6.71×10^{-7}
7(**e**)	$9.67 \pm .6 \times 10^{-6}$	5.29×10^{-7}
8 (**f**)	$2.32 \pm .1 \times 10^{-5}$	4.49×10^{-8}

It is evident from a comparison of Figure 40 with Figure 42 that the Voltz diffusion model (equation 37) fits the observed decay profiles better than the Yokota-Tanimoto model (equation 30). Diffusion coefficients determined from these models are compared in Figure 44.

Figure 44: Concentration dependence of the sum of the $Tb(acac)_3$ + Red 40 diffusion coefficients as determined from energy transfer data using the Yokota-Tanimoto theoretical model (**a**, **b**) and the Voltz theoretical model (**c**, **d**). **a** and **c** are from run 2 and **b** and **d** are from run 1.

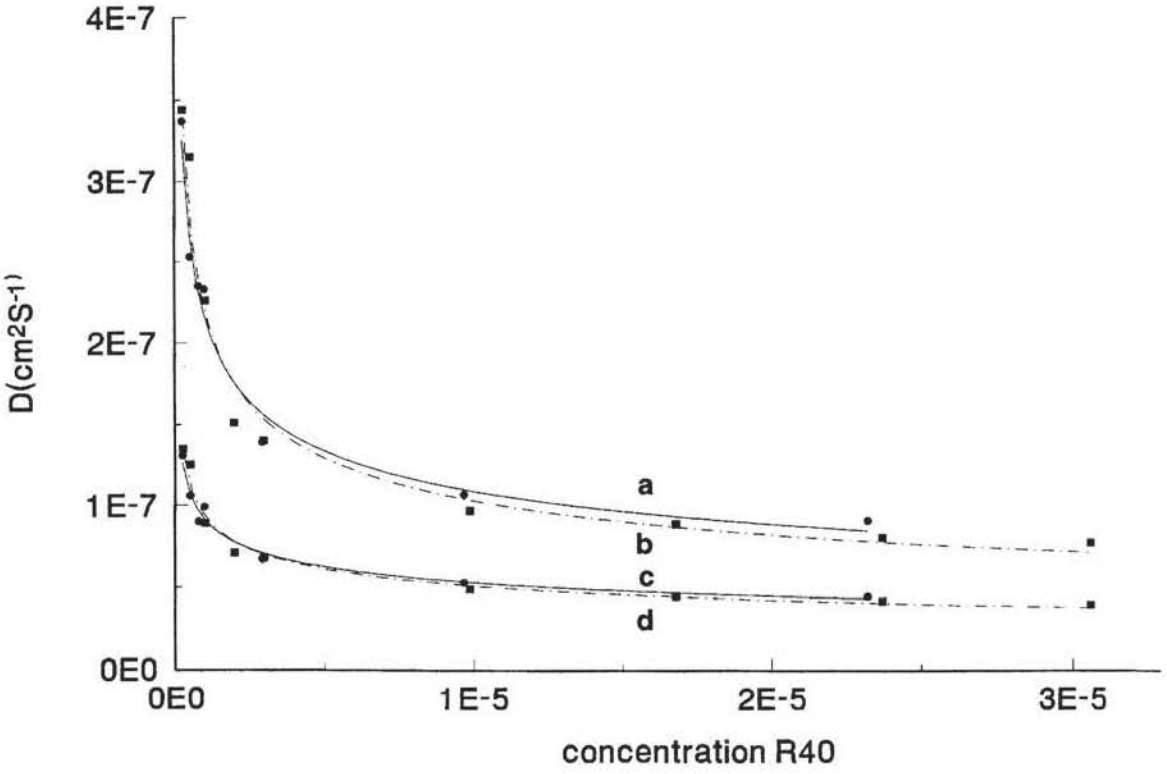

V. Diffusion Effects on Energy Transfer Quantum Efficiency.

Figure 45 compares the time resolved emission profiles of $Tb(acac)_3$ in ethanol with and without Red 40 quencher. These profiles may be compared to curves **a** and **b** in Figure 37 of 0.0 and 5.24 x 10^{-5} M Red 40 quencher in cold glycerol.

Figure 45: Time resolved emission profiles of $Tb(acac)_3$ in ethanol with 0.0 and 3.06 x 10^{-5} M Red 40 quencher.

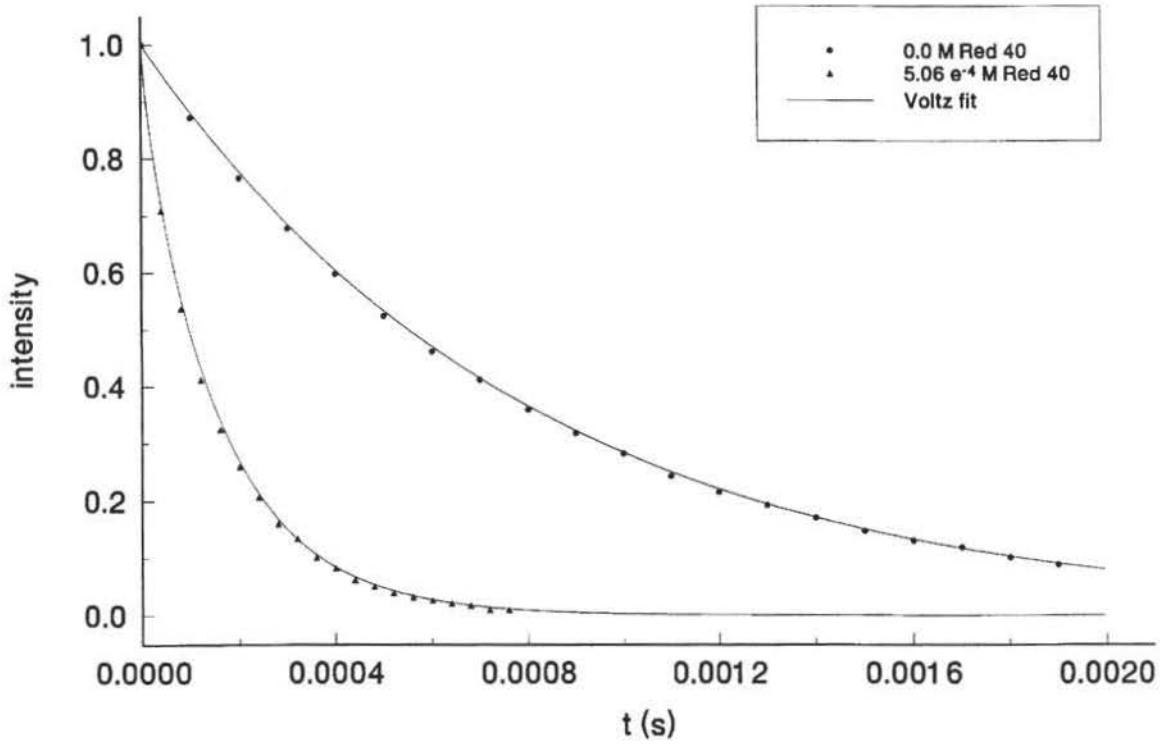

The profiles in Figure 37 show that little energy is transferred at these concentrations in cold glycerol. When compared to Figure 45 it is evident that energy transfer is greatly enhance by diffusion at a similar concentration. These decay profiles can be integrated to determine the total energy emitted by spontaneous emission. The ratio of these integrals with and without quencher $\langle i(t) \rangle / \langle i(t) \rangle_0$ describes radiative efficiency in the presence of quencher and equation 41 describes the quantum efficiency , f (fraction of energy transferred). Energy transfer efficiencies were calculated in this manner for solutions in cold glycerol using the data from curves **a** and **b** in Figure 37 and in room temperature ethanol using the data from Figure 45. The energy transfer in ethanol was found to be approximately 10 times greater than in the glycerol solution of approximately equal concentrations. This dramatic increase can be attributed to diffusion enhancement.

These results are compared to theoretically predicted diffusion enhancement as described by equation (45) in Figure 46.

Figure 46: Diffusion enhanced energy transfer quantum efficiency. A comparison of experimental measurement with theoretical predictions. Concentrations of Red 40 in glycerol = 5.235×10^{-5} M and in ethanol = 3.06×10^{-5} M.

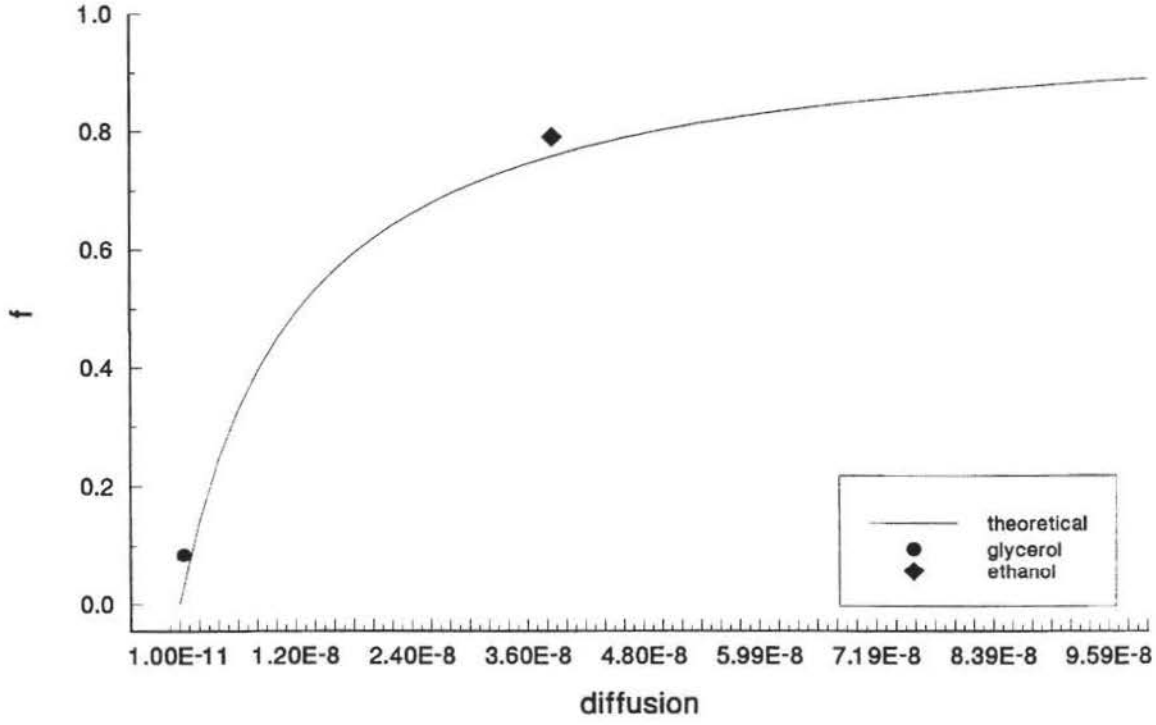

Discussion and Conclusions.

I. Evidence for Ion Association.

This study has revealed trends in excited state lifetime, diffusion coefficients and activity coefficients that dramatically deviate from those of ideal systems (Figure 47). These trends suggest that strong ion associations occur in ethanol solutions of divalent Red 40 at concentrations above 10^{-6} M. Ion associations are known to greatly diminish activity coefficients, ionic mobilities and diffusion coefficients (53).

A bimolecular energy transfer rate constant is given by the slope of a Stern-Volmer plot. As ion association increases with increasing electrolyte concentration, the ability of an anionic energy acceptor to diffuse to within the Förster critical radius is diminished along with the energy transfer rate constant causing a decrease in the slope of a Stern-Volmer plot. (Figure 47 plot **a**).

Diffusion coefficients for ideal binary solutions exhibit a linear dependence on mole fraction concentration (54). In contrast, the diffusion coefficients calculated from the energy transfer data by the Voltz diffusion model are greatly reduced from their infinite dilution limit concentrations above 10^{-6} M (Figure 47 plot **b**).

Theoretical activity coefficients for dilute electrolytes can be calculated from the Debye-Huckel limiting law (55) as a function of their concentration in solvents of a given dielectric constant and temperature.

$$\log \gamma_{\pm} = -1.825 \times 10^{-6} \; |Z^+ Z^-| \left(\frac{\rho_o}{\varepsilon^3 T^3} \right)^{1/2} \left(I \right)^{1/2} \qquad (60)$$

where $Z^{\pm}$ is the charge on the positive or negative ion, ρ the density of the solvent, ε is the dielectric constant of the solvent, T is the temperature in Kelvin and I is the ionic strength of the solution.

Experimental activity coefficients can be determined from measured diffusion coefficients as described by Gordon (56):

$$D(c) = D_o \left(1 + c \frac{\partial \ln \gamma_{\pm}}{\partial c} \right) \frac{\mu_o}{\mu} \qquad (61)$$

where D_o is the diffusion coefficient at infinite dilution, c is the electrolyte concentration, μ_o is the viscosity of the solvent, μ is the viscosity of the solution and $\mu_o / \mu \approx 1.00$ for dilute solutions. The diffusion coefficients determined from the Voltz model (Tables 14 and 15) can be extrapolated to infinite dilution. This limiting value is the sum of the donor + acceptor contributions extrapolated to infinite dilution:

$$D_o = D_o (Tb(acac)_3) + D_o (Red\ 40) \qquad (62)$$

Diffusion coefficients are inversely proportional to their effective hydrodynamic radii (57). Assuming an approximate ratio of r(Red 40): $r(Tb(acac)_3) = 1.3$ (see Figure 48) and a D_o value of 3.4×10^{-7} cm^2/sec, D_o(Red 40) is estimated as 1.5×10^{-7} cm^2/sec. Mean ionic activity coefficients were calculated from experimental diffusion coefficients by numerically integrating equation (61) (Appendix D). The deviation from the Debye-Huckel limiting law (Figure 47, plot **c**) is consistent with ion association.

Figure 47: Deviations from Stern-Volmer kinetics (**a**) are correlated with the Red 40 concentration dependence of the diffusion coefficients (**b**) and mean activity coefficients (**c**) The data in plot **b** were calculated from the Voltz diffusion enhanced energy transfer model. The activity coefficients in plot **c** were calculated by numerical integration of equation (61).

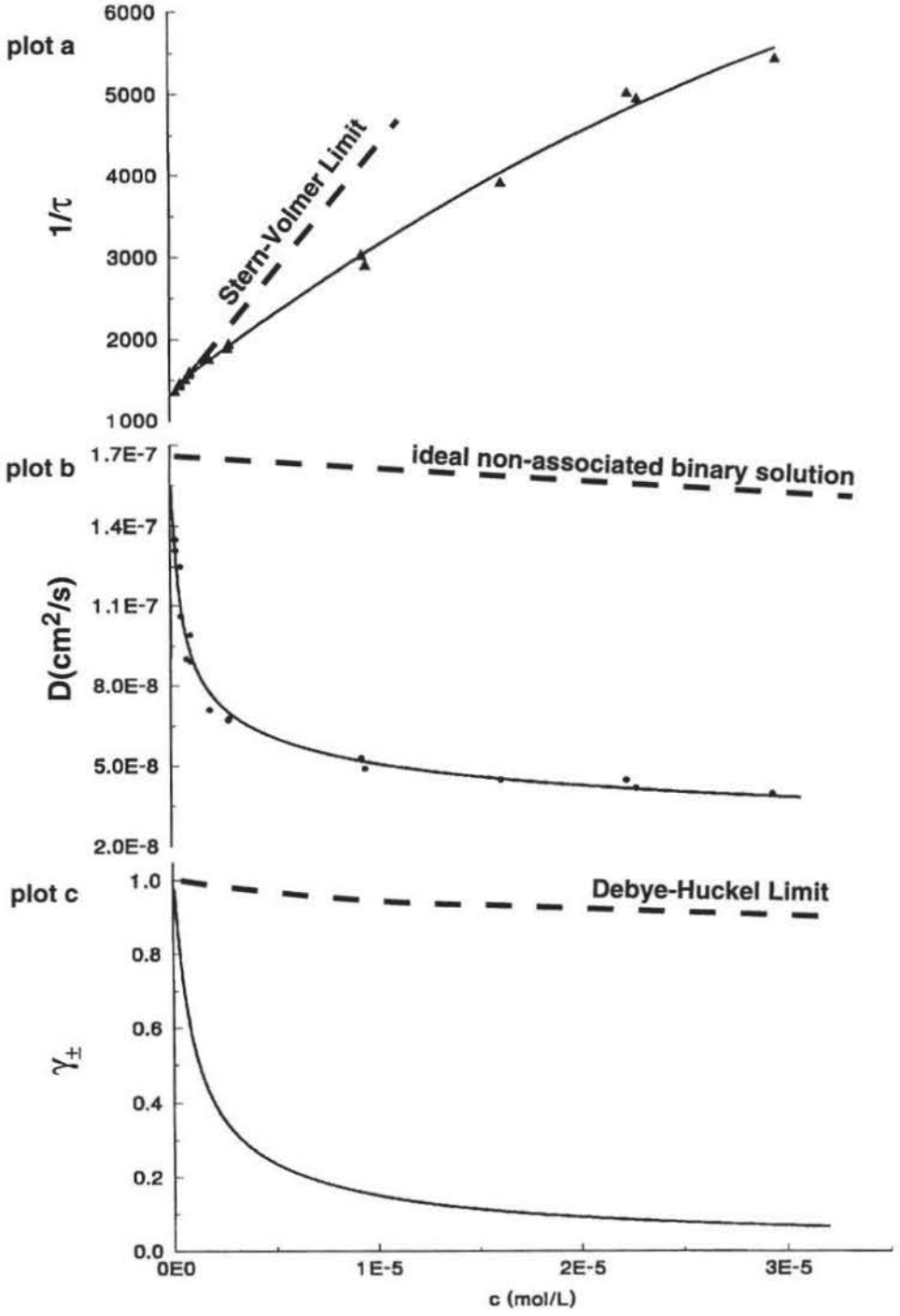

Figure 48: Space filled models of terbium acetylacetonate and Red 40[d] .

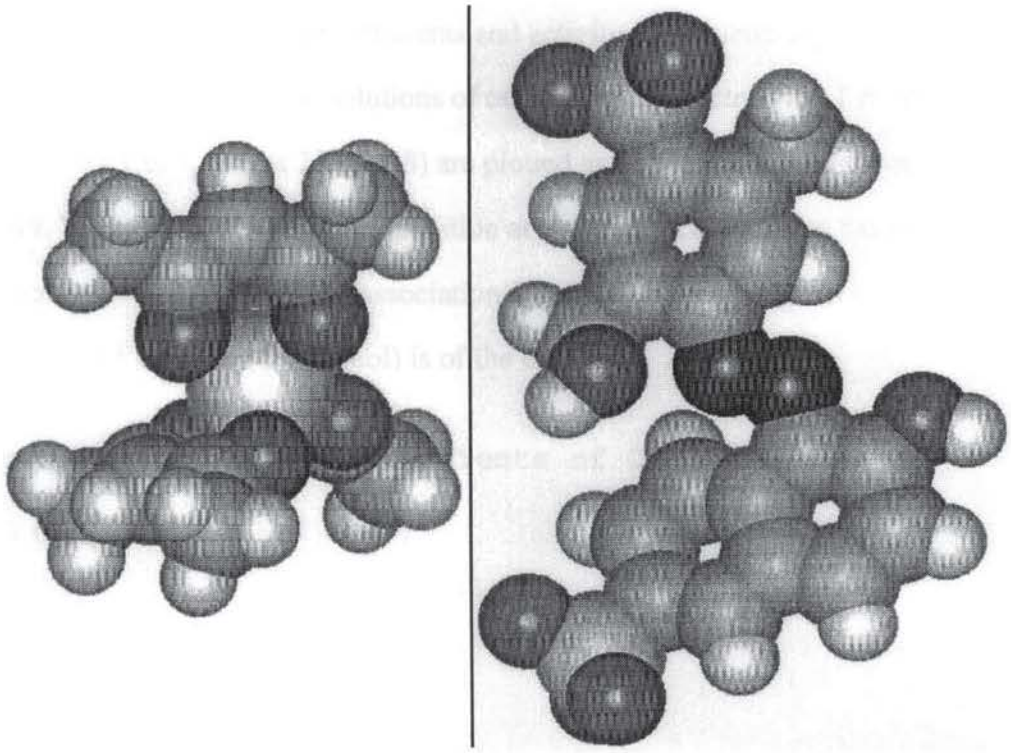

Terbium acetylacetonate Red 40

[d] Graphics by Jeremiah Aeschleman using HyperChem 4 (Hyper Cube Inc., 419 Phillip St., Waterlou, Ontario Canada, N2L3X2)

II. Effects of Dielectric Constant.

The trends in diffusion coefficients and activity coefficients reported in Figure 47 have been observed in aqueous solutions of other divalent electrolytes. Diffusion coefficients for $CaCl_2$ (aq) at 25 °C (58) are plotted as a function of molar concentration in Figure 49. We might define the concentration at maximum curvature as the critical concentration c* above which ion association is appreciable. We note that the ratio of c* for $CaCl_2$ (aq) to c* for Red 40 (ethanol) is of the order 10^4.

Figure 49: Diffusion coefficients of $CaCl_2$.

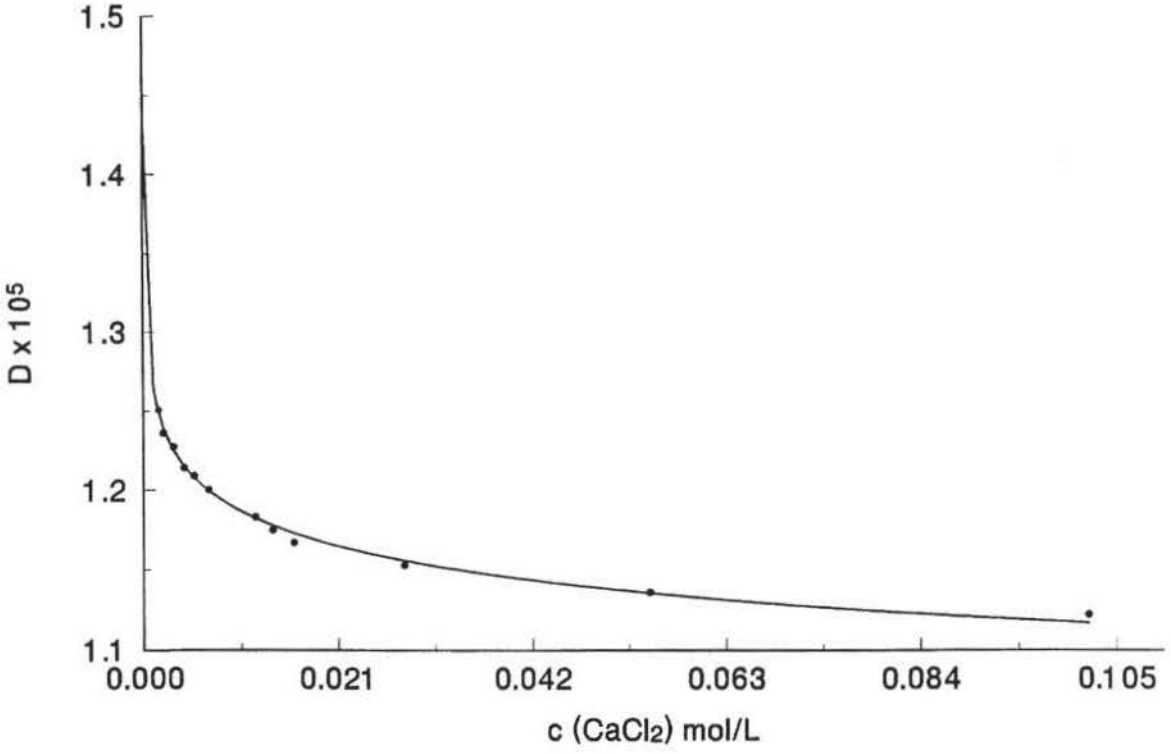

Mean activity coefficients for K_2CrO_4 (aq) at 25 °C (59) are plotted as a function of molar concentration in Figure 50. As in the case of divalent Red 40, the activity coefficient drops to a very low value with increasing concentration. Here we note the ratio of c* for K_2CrO_4 to c* for Red 40 (ethanol) is of the order 10^5.

Figure 50: Mean activity coefficients of K_2CrO_4.

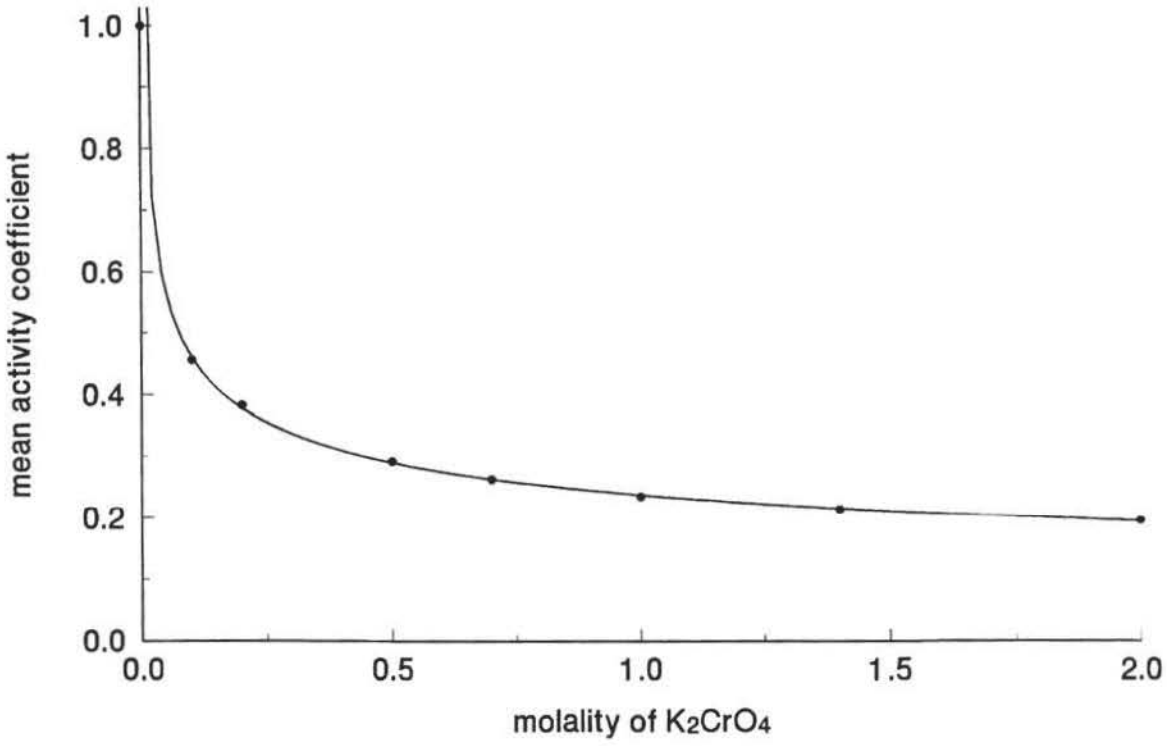

The ratio of critical concentrations in water and alcohol can be related to the corresponding ion association equilibrium constant's dependence on the dielectric constant of the solvent. Denison and Ramsey (60) have shown that ion pair formation constants can be expressed as:

$$K = \exp\left(\frac{|z^+ z^-|e^2}{a\,\varepsilon\,k\,T}\right) \qquad (63)$$

where a is the ion pair contact radius, e the charge of an electron, ε is the dielectric constant of the solvent, k is the Boltzman constant at T the Kelvin temperature.

Consider the ion pair association reaction $m^+ + x^{2-} \leftrightarrow mx^-$ where:

$$K = \frac{[mx^-]}{[m^+][x^{2-}]} \qquad (64)$$

If the concentration of the electrolyte is increased to c* then $[mx^-] \geq [m^+] = [x^{2-}]$ and:

$$K = \frac{(c^*/2)}{(c^*/2)(c^*/2)} = 2 / c^*. \qquad (65)$$

It is instructive to calculate the effect of ε on c*. Assuming a value of 2.4 Å for the ion pair contact radius and ε = 78.5 for water, equation 63 becomes:

$$K_{(H2O)} = \exp\left(\frac{(2)(4.8 \times 10^{-10})^2}{(2.4 \times 10^{-8})(78.5)(1.38 \times 10^{-16})(298)}\right) = \exp(5.95) = 3.82 \times 10^2 \qquad (66)$$

In ethanol when ε = 25.3 then $k_{(ethanol)} = \exp(18.4) = 1.03 \times 10^8$

and:

$$\frac{c^*(water)}{c^*(ethanol)} = \frac{K(ethanol)}{K(water)} = \frac{1.03 \times 10^8}{3.8 \times 10^2} = 2.7 \times 10^5 \qquad (67)$$

Although this calculation was carried out for a hypothetical ion pair it reveals the extreme effect that the dielectric constant of the solvent can have on ion association.

In this study the formation of $[Na(Red\ 40)_2]^{2-}$ triplet ions is considerably more favorable in ethanol than water.

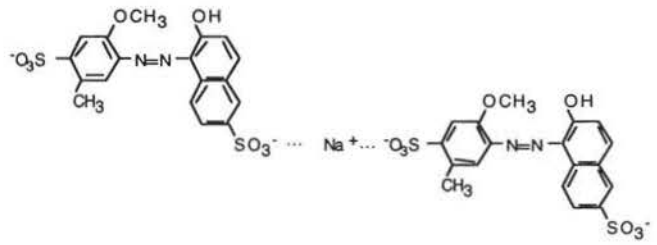

The sterically bulky triplet ion is expected to have considerably smaller mobility and diffusion coefficients than the isolated Red 40 anion.

III. Conductivity Trends.

Table 7 lists the values of resistance and conductivity for measurement of Red 40 in water. The molar conductance of Red 40 is plotted vs the square root of concentration in Figure 51.

Figure 51: Concentration dependence of the molar conductivity of Red 40 in water.

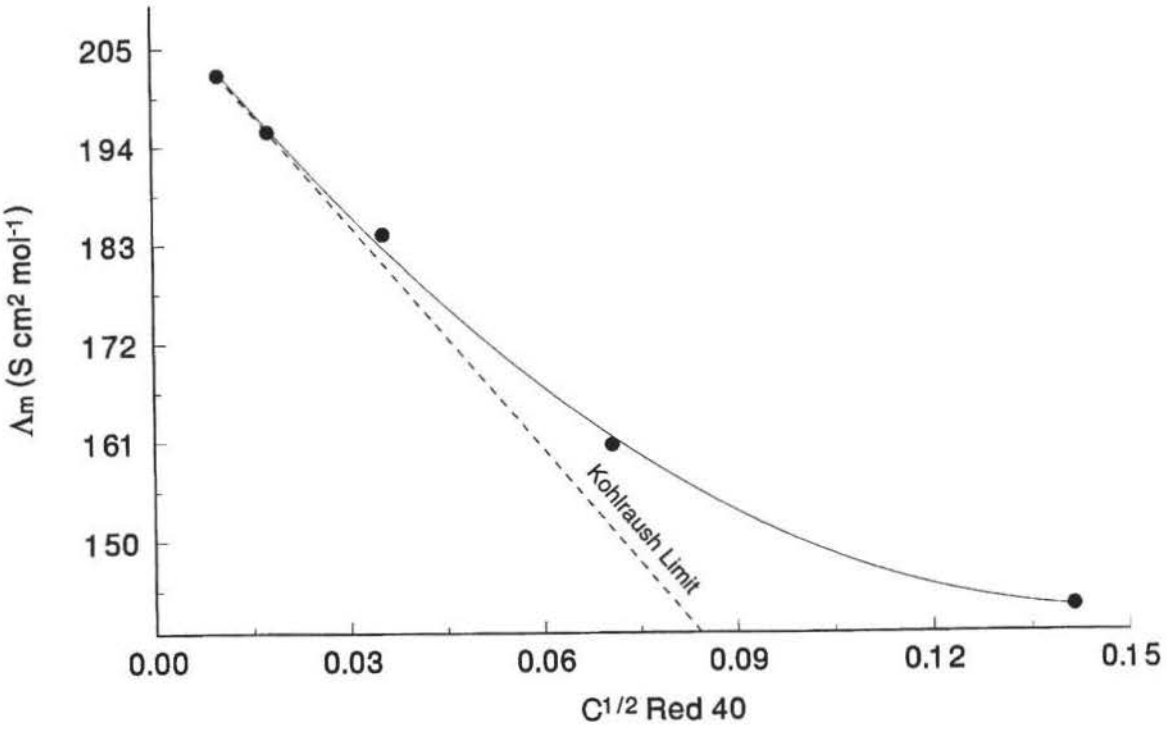

The molar conductivity of the Red 40 anion at infinite dilution, λ_0(Red 40), was found to be 79.05 S cm^2 mol^{-1}. Using this value and equation (55) $D_0(H_20)$, the diffusion of Red 40 in water at infinite dilution, was found to be 1.05 x 10^{-5} S cm^2 mol^{-1}. Although the Red 40 anion is a strong electrolyte in water, it is a divalent ion and shows some tendency to associate into larger species as shown by the deviation from the Kohlrausch limit (Figure 51). This behavior is observed in other divalent ions e.g. $CuSO_4$ (Figure 13).

Other recent spectroscopic studies have observed ion associations in nonaqueous solvents. Alía and Edwards et. al. (61) report vibrational studies of silver(I), copper(I) and thallium(I) thiocyanates in N,N-dimethylthioformamide. They observe IR absorption by ion pairs at 10^{-1} and 10^{-2} M in which silver ion bonded to sulfur while copper ion form bonds to the N atom of the thiocyanate anion. Both types of bonding pairs were detected using thallium.

Muhuri et. al. (62) correlated conductivity measurements with Raman spectra to study pair and triple-ion lithium halide species in 1,2 dimethoxyethane. The IR data suggests that solvation of Li^+ is through the ethereal oxygen atom of DME.

Time resolved laser spectroscopy techniques have been used by Rasimas and Blanchard (63) to study sodium resorufin ion pair dynamics in a binary solvent of *n*-butyl and *tert*-butyl alcohol. Resorufin is an organic anion and a visible chromophore which exhibits strong ion pairing with sodium in *tert*-butyl alcohol and is completely ionized in *n*-butyl alcohol. By using picosecond pump-probe spectroscopy in a mixed solvent system rate constants for both ground state and excited state ion pair formation and dissociations have been determined.

Alía and Diaz et. al. (64) have studied the IR spectrum of lithium trifluoromethane-sulfonate in several solvents. They observed the free monovalent anion's ν_1, S-O

symmetric stretching mode as a single isolated absorption band at 1033 cm^{-1} in water at 10^{-2} M. Extensive ionic pairing was detected in solvents of lower dielectric constant (acrylonitrile, acetonitrile and acetone) as evident by the loss in intensity of the 1033 cm^{-1} and the appearance of new signals at 1043 and 1052 cm^{-1}.

Project Summary.

Pulsed laser spectroscopy has been used to study the luminescence of excited state $Tb(acac)_3$ in the presence of an organic dye, Red 40. The effects of solvent viscosity and radiative path length on wavelength and time resolved spectra have shown that both radiative energy transfer and resonance energy transfer are principal quenching mechanisms in this system.

The excited state lifetime of Tb in the absence of Red 40 has been determined in cold glycerol and room temperature ethanol as 1083(10) and 796(5) μs respectively. These lifetimes are compared with τ_o values of $Tb(acac)_3$ in other solvents in Table 16.

Table 16: The natural radiative lifetime of $Tb(acac)_3$ in various solvents.

Solvent	Temperature (°C)	τ_o (μs)	Ref
pyridine	20	595	16
dimethy sulfoxide	20	649	16
methanol	25	670	17
ethylene glycol	20	695	16
chloroform	25	780	17
n-butanol	20	790	16
ethanol	25	796	This work
acetone	20	800	16
ethanol	23	820	65
benzonitrile	20	825	16

carbon tetrachloride	20	830	16
benzene	20	900	16
acetonitrile	20	930	16
glycerol	0	1083	This work

The Förster critical radius has been determined in cold glycerol and room temperature ethanol as 81(5) and 85(5) Å respectively. These radii are amongst the largest critical radii observed. Thomas et. al. (18) observed $r_0 = 65.7$ Å for $Tb(DPA)_3$ with rhodamine B as the acceptor and $r_o = 44.6$ Å for $Tb(DPA)_3$ with (NDB) diethanolamine as the acceptor. Van Der Meer et. al. (65) reported 63.5 Å using Tb^{3+} as the donor and bacteriorhodopsin as an acceptor. These trends can be attributed to the respective differences in energy transfer overlap integrals. Various resonance energy transfer species have been used extensively to measure intermolecular distances in the range of 10 - 60 Å in peptides, proteins, DNA segments , membranes and polymers (3). The results reported here suggest the use of a Tb^{3+}-Red 40 probe might easily extend those measurements to more than 200 Å.

Interactive computer graphics tools were developed to analyze diffusion enhanced energy transfer dynamics. The Voltz diffusion model was found to fit time resolved $Tb(acac)_3$ emission profiles better than the more elegant Yokota-Tanimoto theory.

Experimentally measured energy transfer efficiencies in cold glycerol were found to be in good agreement with those predicted by Förster theory. Measured diffusion enhanced energy transfer efficiencies in room temperature ethanol solution were also in agreement with theoretical predictions.

Calculated $Tb(acac)_3$-Red 40 diffusion coefficients decreased with increasing concentration of Red 40 in ethanol solutions suggesting significant ion association in ethanol at concentrations above 10^{-6} M.

Diffusion data was used to estimate mean activity coefficients for Na_2Red 40. The concentration dependence of electrical conductance, diffusion and activity coefficients were found to resemble those of other divalent electrolytes. Differences between electrolyte behavior in ethanol and water were shown to be consistent with the respective dielectric constants of these solvents.

Suggested Future Studies.

The effects of ion association on diffusion could be further substantiated by comparing the results of this study with those of a similar study of the electrically neutral Red 40 methyl ester. This species could be prepared by reaction of the sodium salt of Red 40 with methyl iodide or methyl sulfate:

$$Na_2\text{Red 40} + 2CH_3I \rightarrow (CH_3)_2\text{Red 40} + 2NaI \qquad (68)$$

Ion associations are expected to depend on the electric charge density of the participating ions. It would therefore be instructive to carry out similar studies on samples of Red 40 in which Na^+ was exchanged with other cations. For example, the Li^+ salt of Red 40 would be expected to exhibit even greater ion associations and would therefore diminish diffusion enhanced energy transfer with increasing concentration to a greater extent than the Na^+ salt used in the study. The opposite trend would be expected with the $N(Tert\text{-}Butyl)^+$ salt of Red 40.

Ion association is also expected to strongly depend on the dielectric constant of the solvent. The role of ion association in diffusion enhanced energy transfer could therefore

be further verified by a similar study using solvents with larger and smaller dielectric constants than ethanol.

It would be interesting to examine the effects of stirring on the dynamics of energy transfer. Perhaps stirring would provide sufficient mixing to eliminate the time dependence of the energy transfer rate constant and the system could then be described by the Stern-Volmer limit.

The energy transfer dynamics observed in this study suggest that the diffusion and activity coefficients of Red 40 in ethanol drop dramatically above 10^{-6} M. This behavior could be confirmed by a direct measurement of diffusion coefficients using a Polson cell (67-69).

The limited solubility of Red 40 in ethanol prevents conductivity measurements with the conventional dip cells normally used with aqueous solutions. However, a custom conductivity cell equipped with appropriate sized electrodes could be used to study the concentration dependence of Red 40 in ethanol.

Bibliography

1. Scandola, F.; Balzani, V., *J. Chem. Edu.* **1983,** 60, 814-817.

2. Dong, W.; Flint, C. D., *J. C. S., Faraday II*, **1992**, 88(18) 2661.

3. Van Der Meer, B. W.; Coker III, G.; Chen, S.-Y. S., *Resonance energy transfer: theory and data*, VCH, New York, **1994**.

4. Andrews, D. L.; Demidov, A. A., *Resonance Energy Transfer*, Wiley, New York, **1999**.

5. Dawson, W. R.; Kropp, J. L.; Windsor, M. W. *J. Chem. Phys.*, **1965**, 45 p. 2410.

6. Selvin, P. R.; Rana, T. M.; Hearst, J. E., *J. Am. Chem. Soc.*, **1994**, 116, 6029-6030.

7. Horrocks, W. DeW. Jr.; Sudnick, D. R., *Acct. of Chem. Res.*, **1981**, 14, 384-392.

8. Napier, G. D. R.; Neilson, J. D.; Shepherd, T. M., *J. C. S., Faraday II*, **1975**, 1487-1496.

9. Bünzli, J.-C.G.; Choppin, G. R., *Lanthanide Probes in Life, Chemical and Earth Sciences*, Elsevier, New York, **1989** 229.

10. Ref. (9) p 11.

11. Crosby, G. A.; Whan, R. E.; Alire, R. M., *J. Chem. Phys.*, **1961**, 34(3), 743-748.

12. Whan, R. E.; Crosby, G. A., *J. Mol. Spectr.*, **1962**, 8, 322.

13. Freeman, J. J.: Crosby, G. A., *J. Phys. Chem.*, **1963**, 67, 2717-2723

14. Lujan-Upton, H.; Okamoto, Y.; Walser, A. D., *J. Polymer Sci. Part A Polymer Ch*, **1997**, 35(3), 393,394.

15. Kropp, J. L.; Windsor, M. W., *J. Chem. Phys.*, **1965**, 42(5), 1602

16. Neilson, J. D.; Shepherd, T. M., *J. C. S., Faraday II*, **1976**, 72, 545-564.

17. Tanaka, F.; Ishibashi, T, *J. C. S., Faraday II*, **1996**, 92(7), 1105-1110.

18. Thomas, D. D.; Carlsen, W. F.; Stryer, L., *Proc. Natl. Acad. Sci.*, **1978**, 75,12, 5746-5747.

19. Steinberg, I. Z.; Katchalski, E., *J. Chem. Phys.*, **1968**, 48, 2404-2410.

20. Fraiji, L. K.; Hayes, D. M.; Werner, T. C., *J. Chem. Edu.* **1992**, 69, 424-425.

21. Demas, J. N., *J. Chem. Edu.* **1983**, 60, 803-806.

22. Porter, G. B., *Concepts of Inorganic Photochemistry*, Wiley (Interscience), New York, **1975 .**

23. Henderson, G. L., *Am J. Phys.*, **1980**, 48, 8, 604.

24. Sherwin, C. W., *Quantum Mechanics*, Henry Holt, New York, **1959**, Chapter 5.

25. Rabi, I., *Phys. Rev* **1937**, 17, 520.

26. Atkins, P. W. *Physical Chemistry*, 5th ed., W. H. Freeman, New York, **1994**, 764.

27. Förster, Th., *Fara. Disc. Chem. Soc.*, **1959** 27, 7 - 12.

28. a. Förster, Th., *Ann. Phys., Lpz.*, **1948**, 2, 55-75.

    b. Förster, Th., *Z. Naturf.*, **1949**, 4a, 321-327.

29. Rice, S. A., *Diffusion - Limited Reactions*, Elsevier, New York, **1985**, Chapter 2.

30. Dexter, D. L. *J. Chem. Phys.*, **1953**, 21, 836.

31. Galanin, M. D., *Sov. Phys. JETD*, **1955**, 1, 317.

32. McDaniel, E. W.; Mason, E. A. *The Mobility and Diffusion of Ions in Gases*, John Wiley and Sons, N.Y., **1972**, 11.

33. Yokota, M., Tanimoto, O., J. Phys. Soc. Japan, **1967**, 22, 3, 779-784.

34. a. Voltz, R.; Laustriat, G.; Coche, A., *J. Chim. Phys.*, **1966**, 63, 1253-1258.
    b. Voltz, R., et al. *J. Chim. Phys.*, **1966**, 63, 1259 - 1264.

35. Noyes, R. M. *Progress Reaction Kinetics*, **1961**, 1, 129-160.

36. Rice, S. A., *Diffusion - Limited Reactions*, Elsevier, New York, **1985**, Chapter 4.

37. Birks, J. B. *Photophysics of Aromatic Molecules*, Wiley - Interscience, New York, **1970**, Chapter 11.

38. Ref. (26) p. 834-837.

39. Moore, W. J., *Phys. Chem.*, 4th ed., Prentice-Hall New Jersey, **1972**, 426.

40. Ref. (39) pp. 457-458.

41. Ref. (26) p. 840.

42. Ref. (26) p. 824.

43. Ref. (39) p. 437.

44. *The Merck Index*, 12th ed., Budavari, S., ed.; Merck Research Labs: New Jersey **1996.**

45. *Handbook of Organic Solvents*, Lide, D. R.; CRC: Boca Raton, Florida, **1995**, p. 205 .

46. Demas, J. N., Excited State Lifetime Measurements, Academic Press, San Diego, **1983** p 118.

47. Reference (46) p 121.

48. Shoemaker, D. A.; Garland, C. W.; Nibler, J. *Experiments in Physical Chemistry*, Sixth ed., McGraw Hill, New York, **1996**, p. 80-81.

49. Ref. (5) 2411

50. *Handbook of Chemistry and Physics* 71st ed.; Lide, D. R. Ed, CRC Press, Boston, **1990-1991**.

51. Birks, J. B.; Georghiou, S., *J. Phys. B (Proc. Phys. Soc.)*, **1968**, 1(2), 958-965.

52. Smyth, C. P., *Dielectric Behavior and Structure*, McGraw-Hill: New York, **1955**, 7.

53. Harned, H. S.; Owen, B. B., *The Physical Chemistry of Electrolytic Solutions* 3rd ed., Reinhold, N.Y. **1958**.

54. Skelland, A. H. P., Diffusional Mass Transfer, John Wiley and Sons, N.Y. **1974**.

55. Ref. (39) eq 10.66 p. 435.

56. Gordon, J. Chem. Phys. **1937** 522.

57. Ref. (26) p. 850.

58. Harned, H. S.; Levy A. L., *J. Am. Chem. Soc.*, **1955** 77, 265.

59. Stokes, H. R., *Trans. Faraday Soc.*, 1948, 44, 295.

60. Denison, J. T.; Ramsey, J. B., *J. Am. Chem. Soc.*, **1955**, 77, 2615

61. Alía, J. M.; Edwards, H. G. M.; García -Navarro, F. J., *J. Chem., Soc., Faraday Trans.*, **1998**, 94, 1249.

62. Muhuri, P. K.; Das, B.; Hazra, D. K., *J Phys. Chem. B* **1997**, 101, 3329-3332.

63. Rasimas, J. P.; Blanchard, G. J., *J. Phys. Chem.*, **1996**, 100, 11526-11533.

64. Alía, J. M.; Díaz de Mera, Y.; Edwards, H.G.M.; García, F.J.; Lawson, E. E., *J. Mol. Struct.*, **1997**, 408/409, 439-450.

65. Ref. (3) p. 155.

66. Ref. (5), P. 2413.

67. Polson, A., *Nature*. **1944**, 54, 823.

68. Linder P. W. ; Nassimbeni, L. R.; Polson, A.; Rodgers, J., *J. Chem. Ed.*, **1976**, 53, 330536-538.

69. Tanford, C., *Physical Chemistry of macromolecules*, **1961**, Wiley, New York, p. 34.

Appendix A

Integrated Voltz decay profile.

Integrated Voltz decay profile.

The decay of an excited state donor in the presence of an energy transfer acceptor is governed by simultaneous luminescence and non-radiative energy transfer:

$$D^* \xrightarrow{1/\tau_o} D + h\nu \qquad (5)$$

$$D^* + A \xrightarrow{k'_{DA}} D + A^* \qquad (A\text{-}1)$$

and is described by:

$$\frac{d[D^*]}{dt} = -\frac{[D^*]}{\tau_o} - k'_{DA}[A][D^*] \qquad (36)$$

Unlike equation (9) in which the Stern-Volmer rate constant is time independent, the Voltz energy transfer rate constant characterizes a time dependent diffusion process:

$$k'_{AD} = \frac{2\pi N D r_o}{1000}\{1 + r_o(\pi D t)^{-1/2}\} \qquad (35)$$

It is convenient to define:

$$k_{DA} = \frac{2\pi N D r_o}{1000} \qquad (38)$$

and

$$F = \frac{2 N r_o^2 (\pi D)^{1/2} [A]}{1000} \qquad (39)$$

then

$$k'_{DA} = k_{DA} + \frac{F}{t^{1/2}[A]} \qquad (A\text{-}2)$$

The time dependent decay profile of the excited state donor is obtained by integrating equation 36.

$$\int \frac{d[D^*]}{[D^*]} = -\frac{1}{\tau_{obs}} \int [dt] - k_{DA}[A][D^*] \int [dt] - F \int t^{-1/2} [dt]$$

$$\ln \frac{[D^*]}{[D^*]_o} = -\frac{t}{\tau_o} - k_{AD}[A]\, t - 2\, F\, t^{1/2} \qquad \text{(A-3)}$$

Since the emission intensity profile, i(t), is proportional to [D*]:

$$[D^*](t) \propto i(t) = i(t)_o \exp\left(-\frac{1}{\tau_o} - k_{AD}[A]\, t - 2\ F\, t^{1/2}\right) \qquad (37)$$

Appendix B.

Tris (phenanthroline) iron(II) cation as an Energy Transfer Acceptor in the presence of $Tb(acac)_3$.

Tris (phenanthroline) iron(II) cation as an Energy Transfer Acceptor in the presence of $Tb(acac)_3$.

Initially 1, 10-phenanthroline ferrous perchlorate [$(Fe(II)(phe)_3$] appeared to be a good energy transfer acceptor for the $Tb(acac)_3$ system. The compound dissolved reasonably well in ethanol, had an absorption spectrum that overlapped favorably with $Tb(acac)_3$ emission and was ionic as desired.

Figure B-1: Absorption spectra of $Fe(II)(phe)_3$ in alcohol.

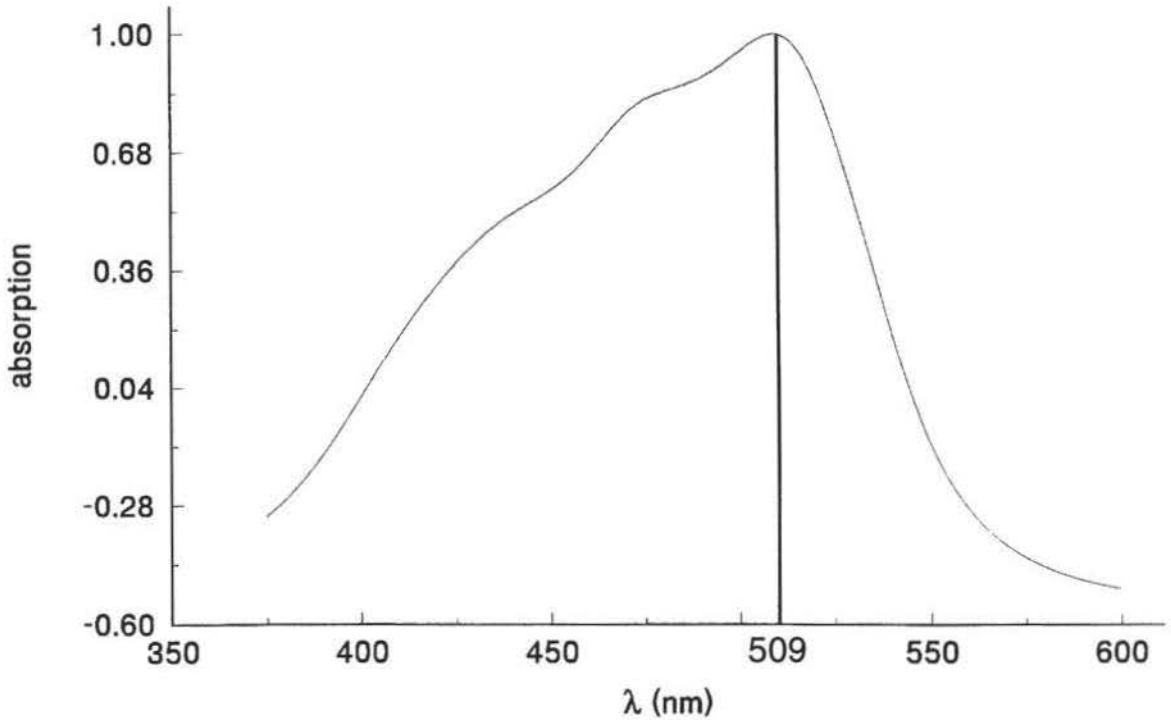

$Fe(II)(phe)_3$ dissolved in alcohol is susceptible to oxidation, but this was not observed through changes in the absorption spectrum to any significant degree in this study. After a $Tb(acac)_3$-$Fe(II)(phe)_3$ dilution series was prepared and measured, it came to be noticed that the initial red-orange color had shifted to yellow. The 509 nm absorption

maximum as seen in Figure B-1 had disappeared. Absorption measurements revealed a less intense peak centered at about 433 nm.

Figure B-2: Absorption spectra of 12 to 1 mixture $Tb(acac)_3$-$Fe(II)(phe)_3$ bleaching from initial mixing to ∞: **a**. 10 min., **b**. 15 min., **c**. 1 hour, **d**. 4 hours and **e**. 3 days.

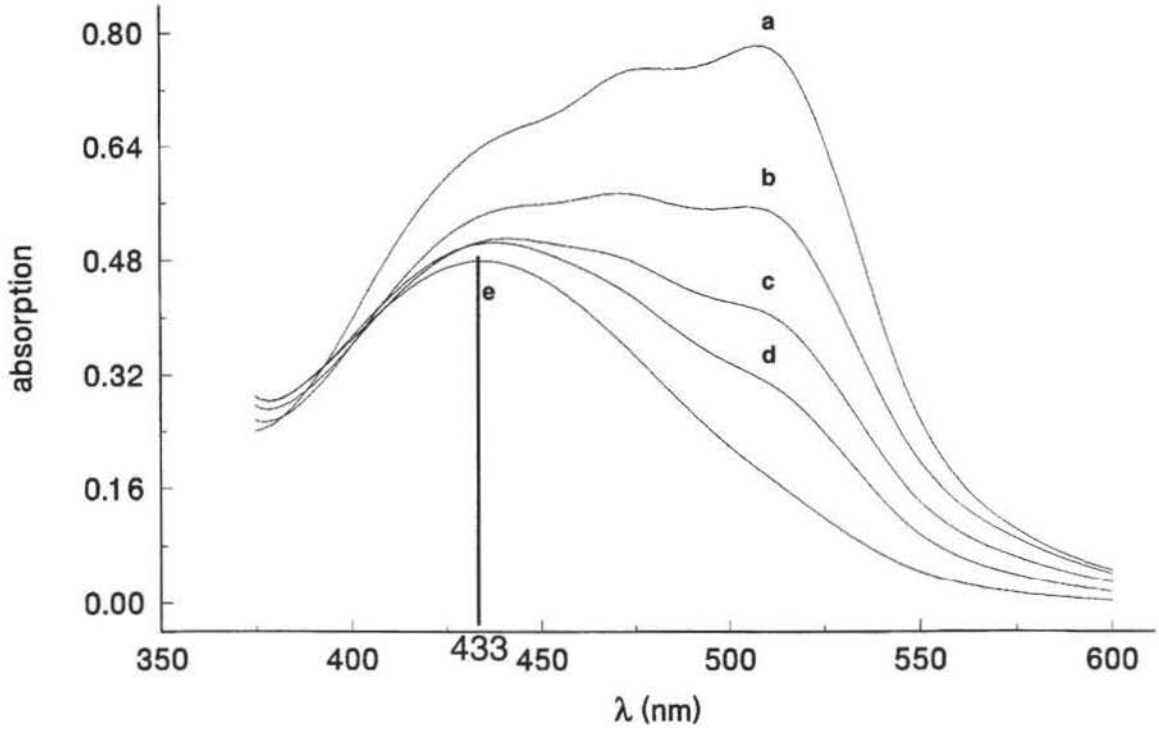

The half life of the reaction was only a few minutes. Possible reactions were oxidation of iron from Fe(II) → Fe(III) or the phenanthroline ligand exchange with acac:

$$Fe(phe)_3^{2+} + acac^- \Leftrightarrow [Fe(phe)_2(acac)]^+ + phe \qquad \text{(B-1)}$$

$$[Fe(phe)_2(acac)]^+ + acac- \Leftrightarrow Fe(phe)(acac)_2 + phe. \qquad \text{(B-2)}$$

Ligand exchange was confirmed by the following experiment. Three test tubes each containing a mixture of 1 x 10^{-3} M $Tb(acac)_3$ and 1 x 10^{-4} M $Fe(II)(phe)_3$ were prepared. A few drops of 2, 4 pentanedione (acac) + NH_3 were added to tube **a**. No reagent was added

to **b** and a few drop of phenanthroline solution added to **c**. Solution **a** changed from red-orange to yellow in about 5 minutes, solution **b** changed similarly in about 20 minutes and **c** held its red-orange color for many days. From this test it appeared that ligand exchange was occurring. S. Ittel[1] described $Fe(II)(DPPE)(acac)_2$ as golden yellow.

Further study of this quenching system was not pursued because the azo dye, Red 40 was found to be stable when mixed with $Tb(acac)_3$ and contained the same desired features as $Fe(II)(phe)_3$.

---

[1] Ittel, S. D., *Inorganic Chemistry*, **1977**, 16(5), p. 1245.

Appendix C.

Solute diffusion distances in ethanol and cold glycerol.

Solute diffusion distances in ethanol and cold glycerol.

The excited state lifetime of $Tb(acac)_3$ in the presence of Red 40 was measured in –10 to 0°C glycerol to approximate the conditions of a random and static distribution of donors and acceptors as described by Förster's equation (27). The root mean square (RMS) distance that a solute molecule will diffuse in time t depends on D, the diffusion coefficient in a given solvent:

$$d_{RMS} = (6Dt)^{1/2}. \qquad \text{(C-1)}$$

D, for a spherical solute molecule of hydrodynamic radius r, can be estimated from temperature (T) and viscosity (η) of the solvent:

$$D = \frac{k\,T}{6\pi\,\eta\,r} \qquad \text{(C-2)}$$

where k is Boltzmans constant. Equations (C-1) and (C-2) can be used to estimate solute diffusion distances in room temperature ethanol and in cold glycerol. These distances can then be compared with diffusion enhancement threshold distances for a given solute concentration.

Room temperature ethanol.

Molecular modeling calculation were used to estimate the hydrodynamic radius of solvated Red 40 anions as 4 Å. Using equation (C-2) and the viscosity of ethanol at 298 K[a]:

$$D_{EtOH} \approx \frac{(1.38 \times 10^{-23})\,(298)\ \text{kg m}^2\text{s}^{-2}}{6\pi\,(1.10 \times 10^{-3}\ \text{kg m}^{-1}\text{s}^{-1})\,(4 \times 10^{-10}\ \text{m})} = 4.96 \times 10^{-10}\ \frac{\text{m}^2}{\text{s}} \qquad \text{(C-3)}$$

[a] *Handbook of Chemistry and Physics* 71st ed.; Lide, D. R. Ed, CRC Press, Boston, **1990-1991**.

and the RMS diffusion distance is:

$$d_{RMS} \approx \sqrt{6\,(4.96 \times 10^{-10}\ m^2/s)\,(.001\ s)} = 1.72 \times 10^{-6}\ m = 17{,}200\ \text{Å} \qquad \text{(C-4)}$$

Cold glycerol.

Measurements in glycerol were made at a temperature between –10 and 0 °C. Using equation (C-2) and the viscosity of glycerol at 273 K[a]:

$$D_{gly} \approx \frac{(1.38 \times 10^{-23})\,(273)\ kg\ m^2 s^{-2}}{6\pi\,(12070 \times 10^{-3}\ kg\ m^{-1}s^{-1})\,(4 \times 10^{-10}\ m)} = 4.14 \times 10^{-14}\ \frac{m^2}{s} \qquad \text{(C-5)}$$

and the root mean square distance traveled is:

$$d_{RMS} \approx \sqrt{6\,(4.14 \times 10^{-14}\ m^2/s)\,(.001\ s)} = 1.58 \times 10^{-8}\ m = 158\ \text{Å} \qquad \text{(C-6)}$$

Threshold energy transfer enhancement diffusion distance.

The number density of a 10 μM solute is:

$$\rho \approx 1 \times 10^{-5}\ \frac{mole}{L} * 6.022 \times 10^{23}\ \frac{mol}{mole} * \frac{1\ L}{1000\ cm^3} * 1 \times 10^{6}\ \frac{cm^3}{m^3} = 6 \times 10^{21}\ \frac{mol}{m^3} \qquad \text{(C-7)}$$

and the average solute-solute distance is:

$$\bar{r} \approx \rho^{-3} = 5.5 \times 10^{-8}\ m = 550\ \text{Å} \qquad \text{(C-8)}$$

The threshold diffusion distance a donor and acceptor pair must travel during the donor's excited state lifetime in order to enhance resonance energy transfer (RET) is (see Figure 9):

$$(\bar{r} - r_o) = 550 - 80 = 470 \text{ Å} \qquad \text{(C-9)}$$

Figure 9: Representation of r_o and the mean donor-acceptor distance, $\bar{r}$.

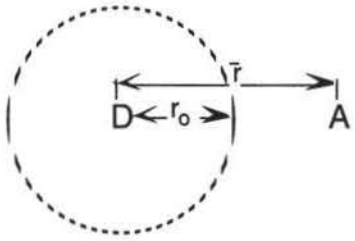

Since the diffusion distance required to enhance RET is larger than the RMS diffusion distance in cold glycerol, measurements in –10 to 0°C glycerol approximate the random and static distribution conditions described by equation (27).

Appendix D.

Activity Coefficients from Numerically Integrated Diffusion Data.

Activity Coefficients from Numerically Integrated Diffusion Data.

Equation (61) describes the concentration dependence of diffusion coefficients in terms of activity coefficients:

$$D(c) = D_o \left(1 + c \frac{\partial \ln \gamma_{\pm}}{\partial c}\right) \frac{\mu_o}{\mu} \qquad (61)$$

In this study diffusion coefficients were determined at various concentrations from energy transfer data. Assuming $u_o = u$ in dilute solutions, equation 61 can be written:

$$\frac{\partial \ln \gamma_{\pm}}{\partial c} = \frac{D(c) - D_o}{D_o c} \qquad (D\text{-}1)$$

This differential equation can be solved numerically by replacing the differential with a finite difference. This technique divides the observed concentration domain into a large number of increments, δc as shown below:

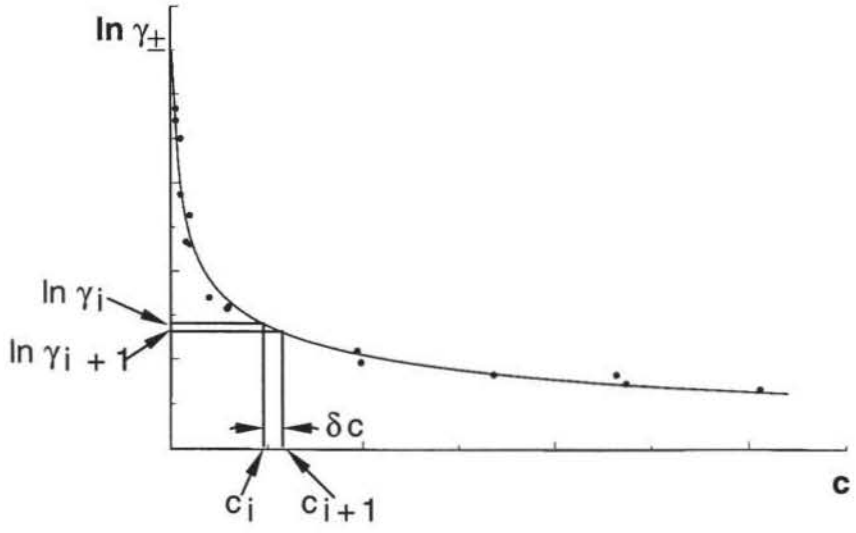

Equation D-1 can then be approximated as:

$$\frac{\delta \ln \gamma}{\delta c} \approx \frac{\partial \ln \gamma}{\partial c} = \frac{D_i - D_o}{D_o c_i} \qquad \text{(D-2)}$$

or

$$\ln\gamma_{i+1} = \ln\gamma_i + \frac{D_i - D_o}{D_o c_i} \delta c \qquad \text{(D-3)}$$

This technique requires a knowledge of the activity coefficient at infinite dilution: $\gamma_o = 1.00$ at $c_o = 0.0$; and the value of D_i at each concentration increment. The D_i values were generated by fitting the observed diffusion coefficients (Tables 14 and 15) to a power function:

$$D(c) = 2.89 \times 10^{-9} * e^{(-.25017)} \qquad \text{(D-4)}$$

and evaluating the function at each concentration step, c_i. The γ values calculated in this manner are presented in Figure 47 **c**.

Appendix E.

LabView VI diagrams (G-code) used for data collection and analysis.

1. *Pulsed Emission Spectrometer* VI: This program controlled the monochrometer, Tektronic digitizer, data transfer and integration of the pulsed luminescence spectra of Tb(III).

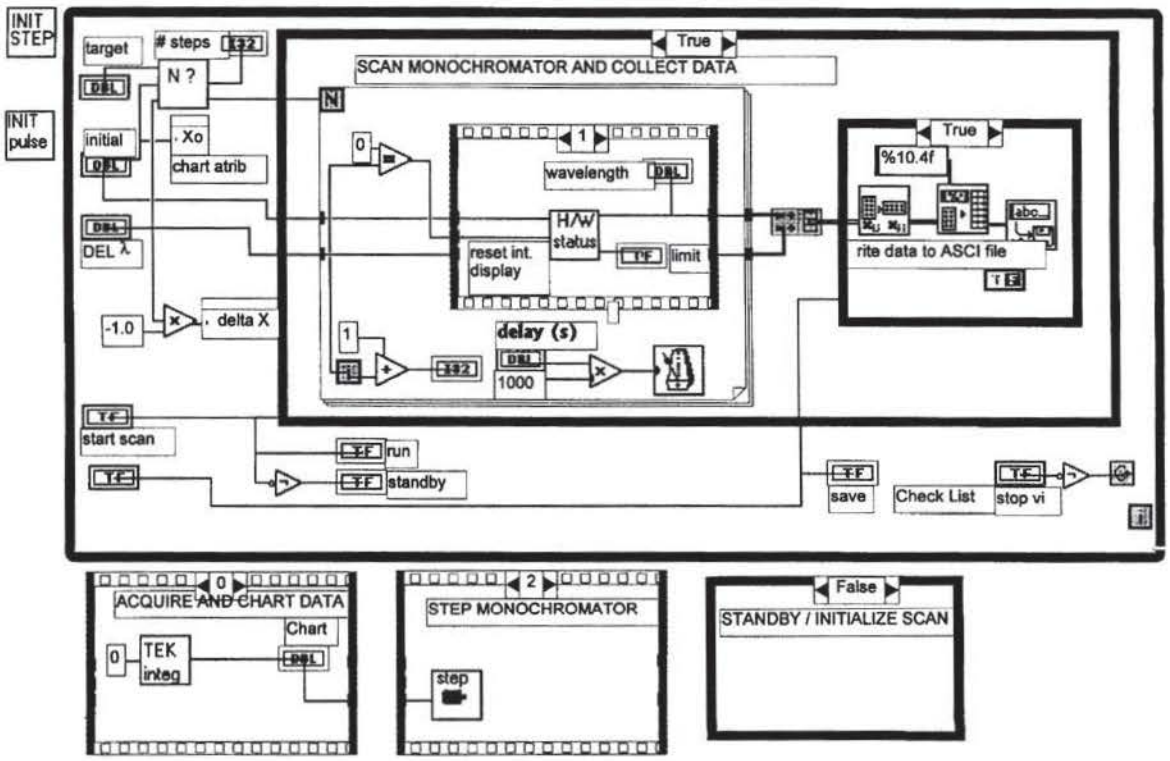

2. *LIF/Raman Spectrometer* VI: The program controlled the laser, monochrometer and gated integrator. This VI acquired data when measuring wavelength resolved spectra of pulsed nanosecond sources.

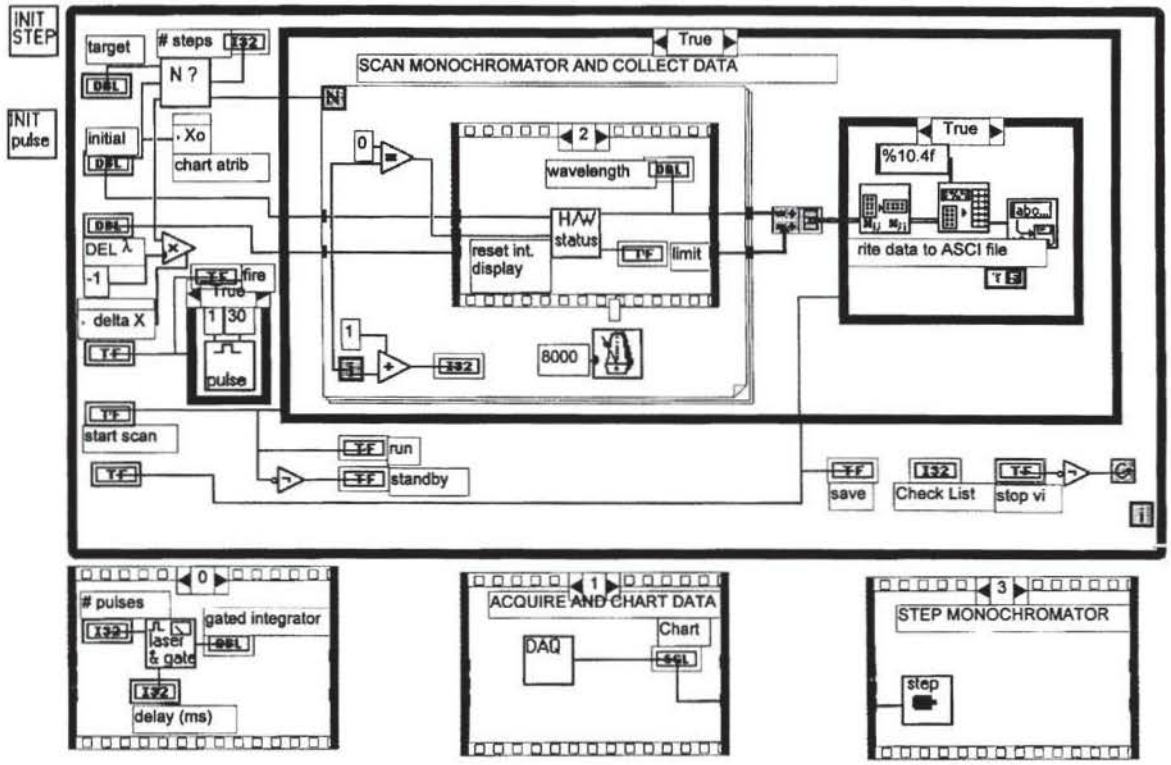

3. *RC Distortion* VI: This program enabled interactive simulation of the RC time constant's distortion of exponential decay profiles.

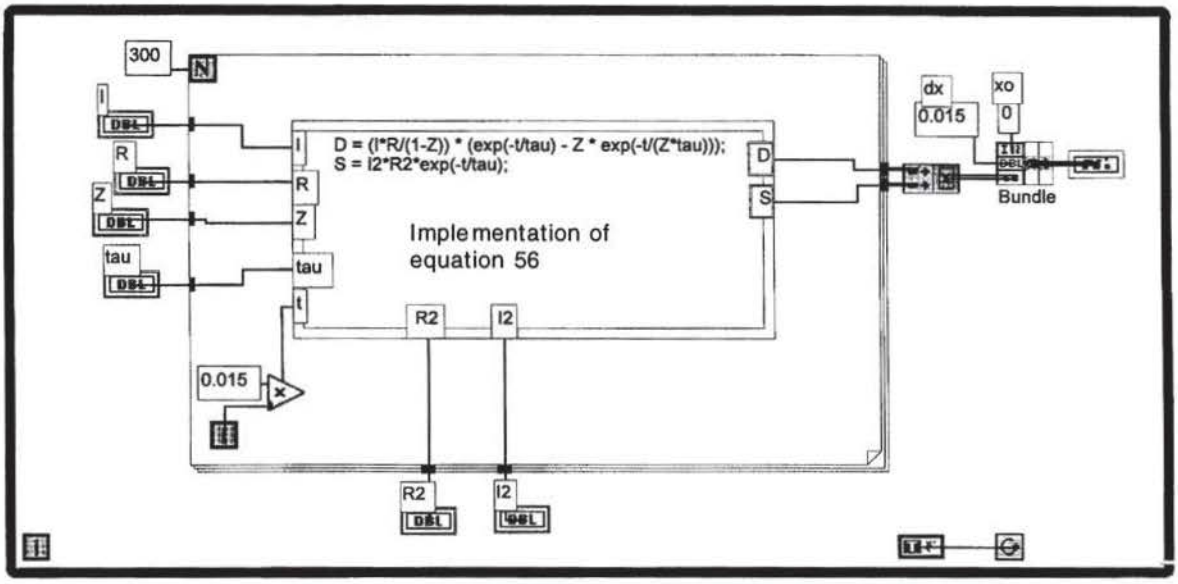

4. *Förster Energy Transfer* VI: This program enabled interactive fitting of the time resolved emission profiles using the Förster resonance energy transfer model.

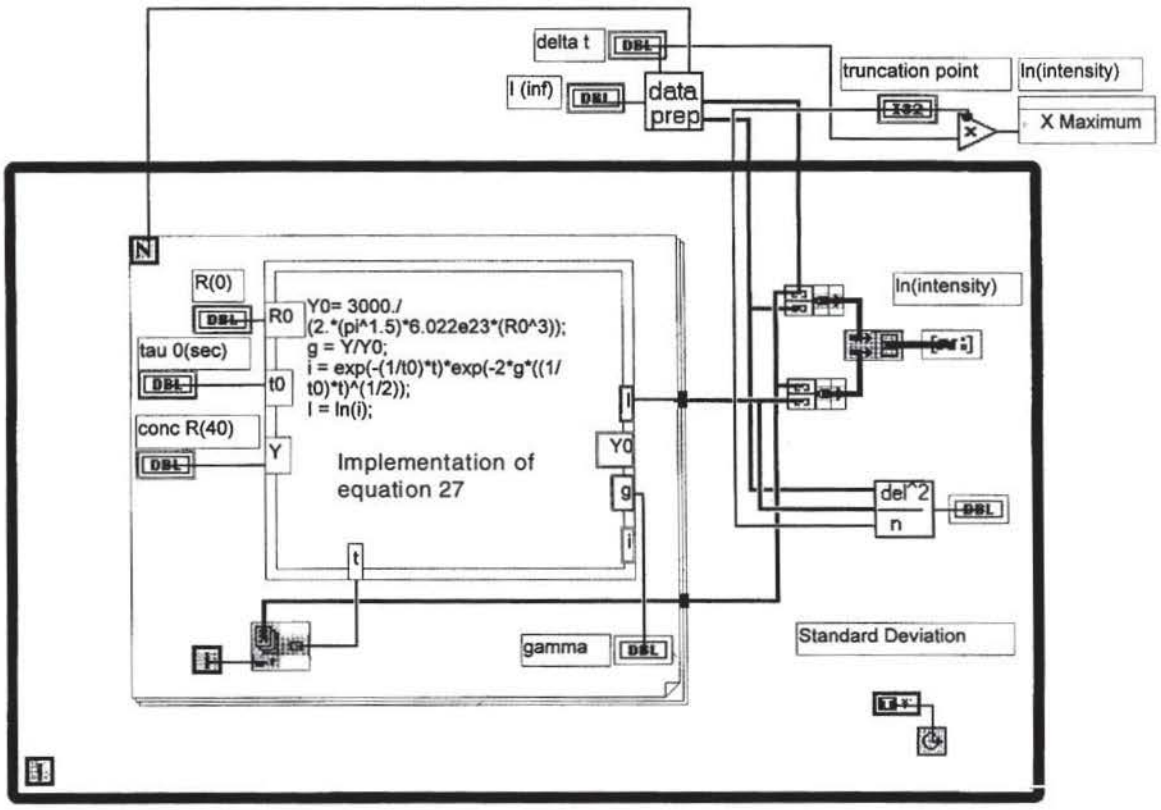

5. *Voltz Diffusion Transfer* VI: This program enables interactive fitting of time resolved emission profiles using either the Voltz or the Yokota-Tanimoto diffusion enhanced energy transfer model.

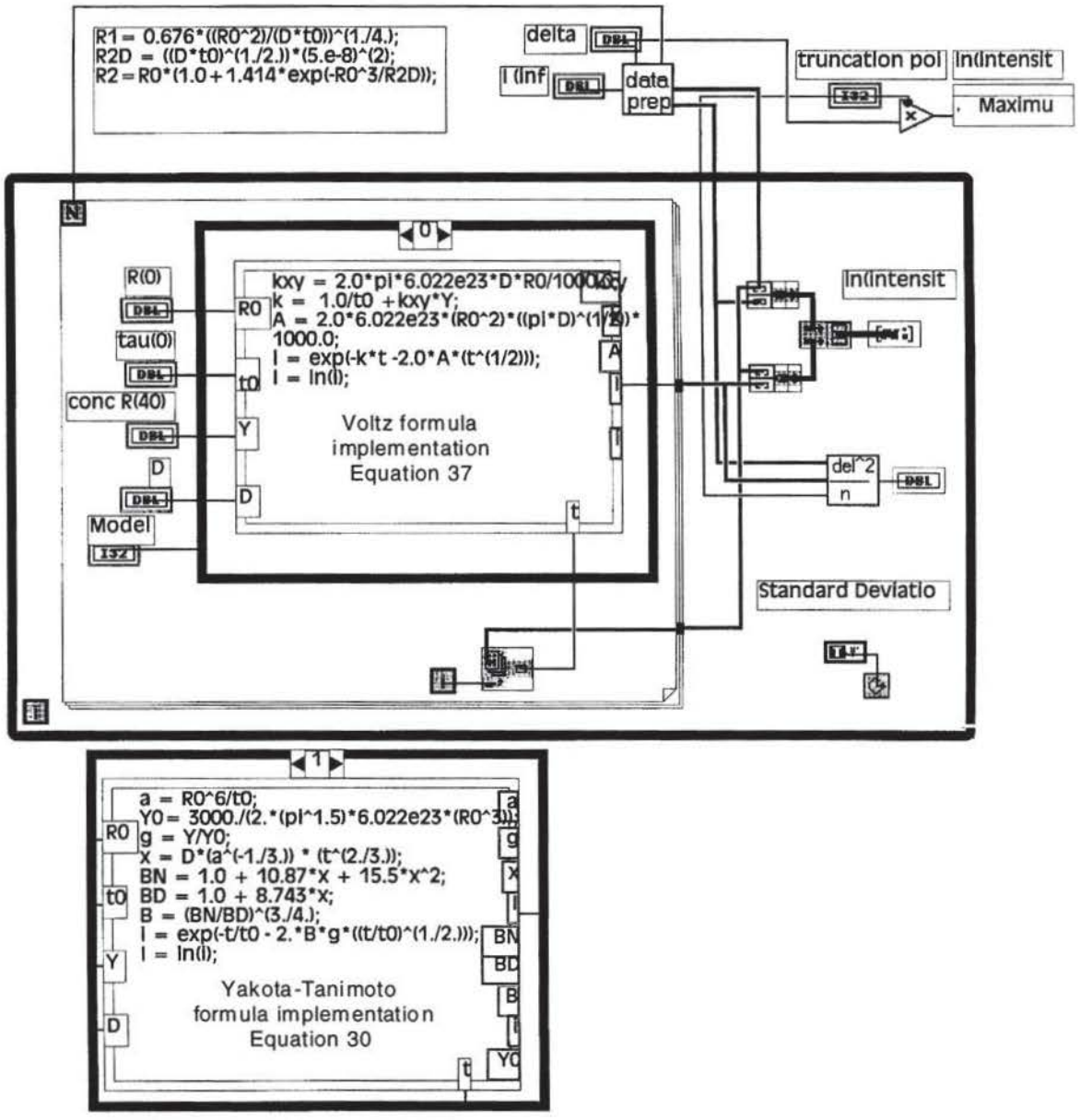

6. *Data Prep* VI: This is a sub VI used by Förster Energy Transfer and Voltz Diffusion/Transfer VI. It opens the user selected file and normalizes the data to an initial intensity of zero before taking ln (i). i_{∞} corrections were applied here if needed.

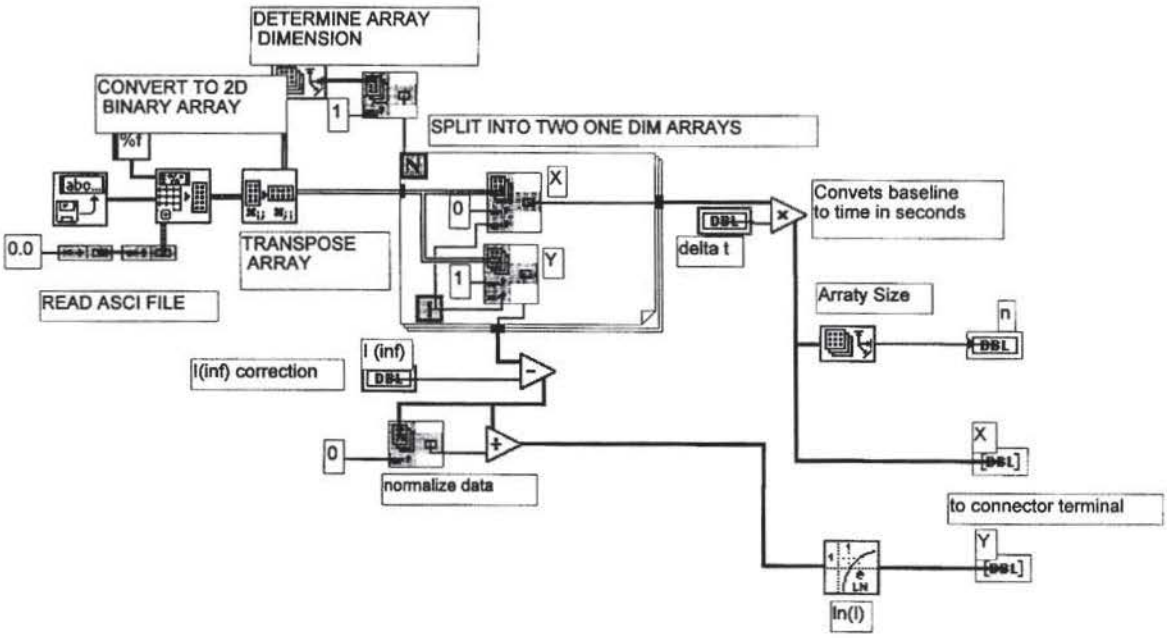

Appendix F.

Excited State Lifetimes and Bimolecular Quenching of Iodine Vapor.

Excited State Lifetimes and Bimolecular Quenching of Iodine Vapor

Giles Henderson, Ronald Tennis, and Terry Ramsey
Department of Chemistry, Eastern Illinois University, Charleston, IL 61920

Extremely accurate molecular constants have been determined for molecular iodine with high-resolution laser spectroscopy (*1–3*). Studies of the vibronic absorption (*4–11*) and emission (*12, 13*) spectra of molecular iodine vapor have become classic experiments in the undergraduate physical chemistry laboratory.

During recent years, the availability of inexpensive monochromatic lasers has enabled undergraduates to study fluorescence emission from selected rovibronic states (*14–16*). Low-cost, tunable, pulsed nitrogen-pumped dye lasers are well suited for these measurements (*17*). Moreover, since the pulse widths of these lasers are short (ns) compared to the I_2 $B(^3\Pi)$ excited state lifetime (μs), they may also be used with a photomultiplier and oscilloscope to directly observe fluorescence decay and the effects of bimolecular quenching (*18*).

Time-resolved gas phase fluorescence measurements usually require a good vacuum system to control and accurately measure sample pressures. It has been our experience that undergraduate students generally lack the experience and expertise with sample purification and vacuum line techniques to avoid fluorescence quenching by molecular oxygen (air) or other foreign gas impurities. However, we find that good time-resolved data can be obtained by using a sealed iodine cell in which the vapor pressure of the sample is accurately controlled by regulating the temperature of the $I_2(s) \rightleftharpoons I_2(vap)$ equilibrium. Once an iodine sample has been purified and vacuum-distilled into a suitable cell and the cell sealed, there is no further need for a vacuum line or accurate pressure measurements. In this paper, we describe a computer-controlled thermoelectric module used to regulate sample vapor pressures and present representative student results derived from Stern–Volmer analysis of fluorescence decay data.

Theory

A ground state I_2 $X(^1\Sigma_g^+)$ molecule will undergo a transition to the $B(^3\Pi_{ou}^+)$ excited state upon absorbing a photon of appropriate wavelength. The excited molecule can lose its excess energy by spontaneous emission (fluorescence) and also by nonradiative processes including predissociation and bimolecular quenching. Fluorescence quenching occurs when an excited B-state molecule collides with another iodine molecule or a foreign gas molecule and loses its energy without the emission of a photon, usually by dissociating (*18*).

If the iodine molecules are initially excited with a laser pulse that is much shorter than the excited state lifetime, the decay of the excited state can be experimentally measured by observing the fluorescence intensity as a function of time:

$$\frac{d[I_2^*]}{dt} = -\frac{[I_2^*]}{\tau_{rad}} - \frac{[I_2^*]}{\tau_{nr}} - k_s[I_2][I_2^*] \qquad (1)$$

The first term represents decay of the excited state concentration, $[I_2^*]$, by spontaneous emission with a radiative lifetime τ_{rad}. The second term in eq 1 represents nonradiative decay due to spontaneous predissociation. The rate constant for nonradiative decay, $1/\tau_{nr}$, is dependent on the vibrational and rotational energies of the excited molecule. The third term in eq 1 describes fluorescence quenching, usually by dissociation, which can occur when I_2^*collides with another I_2 molecule. This bimolecular process is characterized by a rate constant k_s and depends on a collision cross section.

The integrated form of eq 1 describes an exponential fluorescence decay:

$$[I_2^*] = Ae^{-t/\tau_{obs}} \qquad (2)$$

where A is a constant and

$$\frac{1}{\tau_{obs}} = \frac{1}{\tau_{rad}} + \frac{1}{\tau_{nr}} + k_s[I_2] \qquad (3)$$

Since the fluorescence intensity is proportional to $[I_2^*]$, the fluorescence lifetime τ_{obs} can be obtained from the slope of a plot of the natural logarithm of fluorescence intensity vs time. $k_s[I_2]$ has dimensions s^{-1} and may be regarded as a collision frequency associated with a self-quenching cross section σ_s.

If a monochromatic laser pulse is used to generate the excited-state molecules, the nonradiative lifetime is a constant, characteristic of a particular vibrational and rotational energy level. Thus, under this condition, the first two terms of eq 3 are constant and can be combined:

$$\frac{1}{\tau_0} = \frac{1}{\tau_{rad}} + \frac{1}{\tau_{nr}} \qquad (4)$$

It is convenient to express the concentration of iodine vapor molecules per unit volume in terms of pressure. Using eq 4 and the ideal gas law, eq 3 may be written:

$$\frac{1}{\tau_{obs}} = \frac{1}{\tau_0} + \frac{k_s}{kT}P(I_2) \qquad (5)$$

where τ_0 is the fluorescence lifetime in the limit $P(I_2) \rightarrow 0$. Alternatively, the decay can be expressed in terms of the effective collision cross section:

$$\frac{1}{\tau_{obs}} = \frac{1}{\tau_0} + \sigma_s\sqrt{\frac{16\pi}{mkT}}P(I_2) \qquad (6)$$

where σ_s is the effective self-quenching cross section[1] and m is the mass of an iodine molecule.

It is evident from eqs 5 and 6 that both the quenching rate constant and the effective self-quenching cross section can be obtained from the slope of a Stern–Volmer plot of $1/\tau_{obs}$ vs the iodine vapor pressure, $P(I_2)$.

[W] Supplementary materials for this article are available on *JCE Online* at *http://jchemed.chem.wisc.edu/Journal/issues/1998/Sep/abs1139.html*.

Experimental Procedure

Time-Resolved Photometry

Our students use a Laser Photonics model LN300C sealed nitrogen laser to pump an LD2S dye laser (Fig. 1). Coumarin C-500 is well suited as a laser dye, since emission can be induced over the range 473 to 547 nm—which coincides with the I_2 (B ← X) absorption band. This system produces 3.5-ns pulses of 9-kW peak power. Although simple filters have been successfully used to remove scattered laser radiation from fluorescence emission (*18*), we have adapted an old Hitachi 139 monochromator for this purpose. Time-resolved emission intensities are measured with a photomultiplier (PMT) tube and are digitized and displayed with a 100-MHz Tektronix TDS-320 oscilloscope. The PMT analog signal is connected to the oscilloscope by means of double shielded (Belden 9273) coaxial cable. Special precautions must be taken to match the impedance of the photomultiplier and the oscilloscope to the impedance of the connecting coaxial cable to avoid reflected standing waves at these impedance boundaries. This can be achieved by simply terminating the 50-Ω coaxial cable with 50-Ω resistors between the signal conductor and ground. Digitized data are transferred to a Pentium PC through an 8-bit parallel ANSI/IEEE 488 (GPIB) communication port. Data transfer to a user-specified ASCII data file is controlled by National Instrument LabView software (6504 Bridge Point Parkway, Austin, TX 78730-5039).

Vapor Pressure Control

Iodine vapor is in equilibrium with iodine solid at temperatures below its triple point: $I_2(s) \rightleftharpoons I_2(g)$. Thus the vapor pressure of the sample (*19*) can be controlled by regulating temperature in accord with equation (*7*):

$$\log P(\text{atm}) = \frac{-3512.830}{T} - 2.013 \log T + 13.37400 \quad (7)$$

We use a computer-controlled Peltier thermoelectric (TE) module to regulate the equilibrium temperature of the sample cell's cold-finger between 5 and 25 °C. Precise temperature control (±0.02 °C) is achieved by operating the TE unit in a pulsed mode. A regulated power supply is computer gated to deliver a predetermined number of discrete energy pulses to the Peltier device. The pulse sequence is determined by a computer that monitors the sample temperature with a precision thermistor. The computer uses the difference between the set-point temperature and the actual temperature along with a calibrated heat capacity function to calculate the pulse sequence. The software used to control the temperature and vapor pressure of the sample has been developed with National Instrument LabView. The program creates an interactive virtual instrument (VI) control panel which is displayed on the computer monitor (Fig. 2). The various knobs, controls and switches on the VI panel are operated with the computer mouse and are active while the program is running. Panel indicators display the current temperature and the mean and standard deviation of the past 50 measurements, and chart the temperature history. Equation 7 is used by the computer to calculate the corresponding vapor pressure, which is then displayed on the VI pressure gauge.

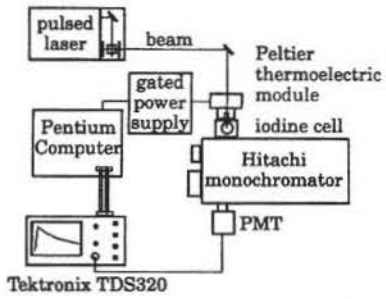

Figure 1. Time-resolved fluorescence measurements of iodine vapor. Sample vapor pressures are controlled by a Peltier thermoelectric module powered by a computer-controlled gated power supply. $B(^3\Pi)$ molecules are prepared by 3.5 ns dye laser pulses. Time-resolved profiles of specific vibronic emission features are observed with a monochromator, photomultiplier, and computer-interfaced oscilloscope.

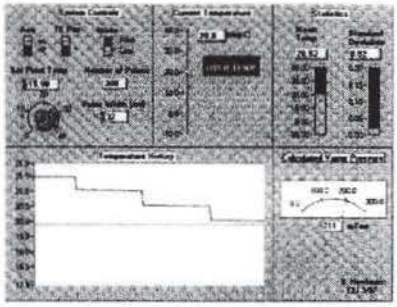

Figure 2. LabView virtual temperature control panel. All switches and controls can be operated interactively by means of a mouse. In this figure, the temperature history chart shows cooling steps in progress towards a panel-controlled set-point temperature (19.90 °C). Fifty consecutive temperature readings are made in each plateau region, the mean and standard deviation are calculated and displayed, and a TE pulse sequence determined for the next cool/heat cycle. The maximum number of TE power pulses in each sequence is limited to avoid overshooting the set-point temperature. The software also calculates and displays the sample vapor pressure.

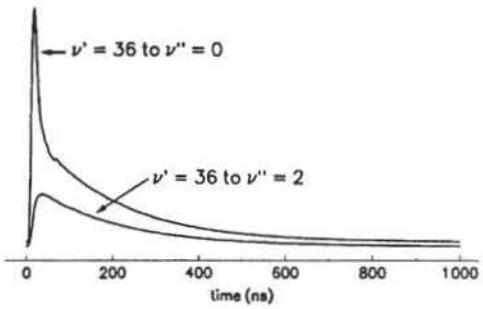

Figure 3. Time-resolved fluorescence measurements at ambient temperature. The upper profile is observed at the excitation wavelength (524.1 nm) and exhibits a spike due to scattered laser radiation on top of the slower-decaying resonance fluorescence signal. Tuning the monochromator to a longer wavelength (536.1 nm), non-resonance vibronic emission band eliminates the scattered radiation component, as observed in the lower profile.

Measurements

Students determine an excitation wavelength by consulting a previously measured vibronic absorption spectrum and choosing a band head in the region of the dye laser's maximum intensity. Both the monochromator and the dye laser are then tuned to the excitation wavelength. Slit width and PMT gain are adjusted to display the time-resolved fluorescence signal on the oscilloscope. A typical profile measured at ambient room temperature (Fig. 3) exhibits a sharp spike due to scattered laser radiation on top of a much slower-decaying resonance fluorescence signal. The scattered radiation component can be eliminated, at some expense to signal intensity, by retuning the monochromator to a nearby nonresonance fluorescence emission signal (Fig. 3). Students are instructed to use the signal-averaging capability of the oscilloscope to enhance the signal-to-noise ratio.

Our students measure fluorescence decay curves at approximately 4.9, 12.2, 16.7, 19.9, and 22.5 °C, which give corresponding iodine vapor pressures of approximately 50, 100, 150, 200, and 250 mtorr, respectively (Fig. 4). The data are transferred from the oscilloscope to an ASCII computer file for subsequent analysis.

Results

A representative example of the natural logarithm of the fluorescence decay plotted vs time is shown Figure 5. The fluorescence lifetimes derived from the least-squares slopes of these plots are summarized in Table 1.

A typical Stern–Volmer plot of $1/\tau_{obs}$ vs $P(I_2)$ is shown in Figure 6. The fluorescence lifetime τ_0 in the limit $P(I_2) \rightarrow 0$ is determined from the intercept of the line fit by least squares. The self-quenching rate constant k_s and the effective self-quenching cross section $\sigma(I_2)$ are calculated from the slope of the line fit by least squares to the Stern–Volmer plot, in accord with eqs 5 and 6. Typical student results are compared with literature values in Table 2.

Discussion

Our students' results are in excellent agreement with those reported by Capelle and Broida (*18*) as well as with earlier modulated continuous-wave phase-shift measurements (*20*). We have found it much easier to provide a well-regulated sample temperature and vapor pressure with a sealed cell than to directly measure and control sample pressures with conventional vacuum systems. This approach eliminates competing quenching processes from air or other impurities and provides years of trouble-free measurements. We have designed an inexpensive, computer-controlled Peltier device for precise temperature regulation using readily available and inexpensive components.

Table 1. Fluorescence Lifetimes of I_2 B($^3\Pi$)

t / °C	P_{vap} / mtorr	τ / ns
4.90	50(1)	732(1)
12.20	100	465
16.70	150	351
19.90	199	289
22.50	249	245

NOTE: Numbers in parentheses are precision limits of last digit.

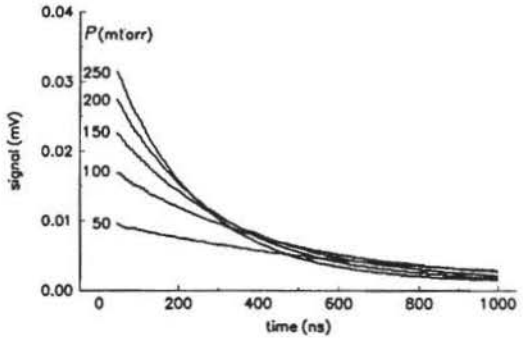

Figure 4. $v' = 36 \rightarrow v'' = 2$ fluorescence decay curves measured at 536.1 nm. An increase in sample pressure results in an increase in fluorescence intensity, while the corresponding increase in collision frequency causes a decrease in the excited-state lifetimes.

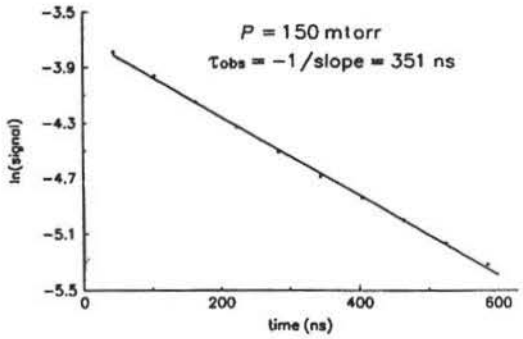

Figure 5. A representative regression plot of fluorescence decay of I_2 B($^3\Pi$) measured at 249 mtorr pressure. The fluorescence lifetime is determined from the least-squares slope (Table 1).

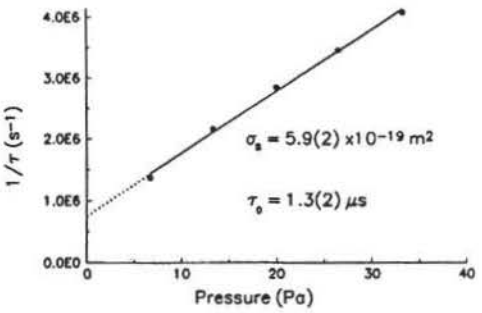

Figure 6. The I_2 B($^3\Pi$) effective self-quenching cross section is determined from the least-squares slope of a Stern–Volmer plot in accord with eq 6.

Table 2. Student Results Compared to Literature Values

Parameter	Student Value	Literature (*18*) (pulsed laser)	Literature (*20*) (phase shift)
k_s / $m^3\ s^{-1}$	$4.1(2) \times 10^{-16}$	$4.0(5) \times 10^{-16}$	$4.1(3) \times 10^{-16}$
$\sigma(I_2)$ / m^2	$5.9(2) \times 10^{-19}$	$5.8(6) \times 10^{-19}$	$6.0(4) \times 10^{-19}$
τ_0 / μs	1.3(2)	1.1(2)	0.97(5)

NOTE: Numbers in parentheses are precision limits of last digit.

Acknowledgments

We wish to express our gratitude to the National Science Foundation, Instrumentation and Laboratory Improvement Grant No. DUE-9551644, for supporting the development of laser spectroscopy in our undergraduate curriculum.

Note

1. The effective *self-quenching* cross section is defined $\sigma_s = (d_{12})^2$ where d_{12} is the $I_2^* - I_2$ collision diameter (*18, 21*), not to be confused with the effective *collision* cross section, $\sigma = \pi(d_{12})^2$ (*21*).

Literature Cited

1. Levenson, M. D.; Schawlow, A. L. *Phys. Rev. A* **1972**, *1*, 10–20.
2. Wei, J.; Tellinghuisen, J. *J. Mol. Spectrosc.* **1974**, *50*, 317–332.
3. Gerstenkorn, S.; Luc, P.; LeRoy, R. J. *Can. J. Phys.* **1991**, *69*, 1299–1303.
4. Davies, M. *J. Chem. Educ.* **1951**, *28*, 474–477.
5. Stafford, F. E. *J. Chem. Educ.* **1962**, *39*, 626–629.
6. Hollenberb, J. L. *J. Chem. Educ.* **1970**, *47*, 2–14.
7. D'alterio, R.; Mattson, R.; Harris, R. *J. Chem. Educ.* **1974**, *51*, 282–284.
8. McNaught, I. J. *J. Chem. Educ.* **1980**, *57*, 101–105.
9. Snadden, R. B. *J. Chem. Educ.* **1987**, *64*, 919–921.
10. George, S.; Krishnamurthy, N. *Am. J. Phys.* **1989**, *57*, 850–853.
11. Lessinger, L. *J. Chem. Educ.* **1994**, *71*, 388–391.
12. Steinfeld, J. *J. Chem. Educ.* **1965**, *42*, 85–87.
13. Shoemaker, D.; Garland, C.; Nibler, J. *Experiments in Physical Chemistry*, 6th ed.; McGraw-Hill: New York, 1996; p 425.
14. Tellinghuisen, J. *J. Chem. Educ.* **1981**, *58*, 438–441.
15. Lewis, E. L.; Palmer, C. W. P.; Cruickshank, J. L. *Am. J. Phys.* **1994**, *62*, 350–356.
16. Muenter, J. S. *J. Chem. Educ.* **1996**, *73*, 576–580.
17. Jones, K. In *Optics and Spectroscopy Undergraduate Resource Book*; Jones, K. M.; Strait, J., Eds.; Optical Society of America: Washington, DC, 1993; pp 121–124.
18. Capelle, G. A.; Broida, H. P. *J. Chem. Phys.* **1973**, *58*, 4212–4222.
19. Gillespie, L. J.; Fraser, L. H. D. *J. Am. Chem. Soc.* **1936**, *58*, 2260–2263.
20. Chutjian, A.; Link, J. K.; Brewer, L. *J. Chem. Phys.* **1967**, *46*, 2666–2675.
21. Moore, W. J. *Physical Chemistry*, 4th ed.; Prentice-Hall: Englewood Cliffs, NJ, 1972; p 366.

Appendix G.

Vibration Spectra, Heat Capacity and Speed of Sound of Methane.

ABSTRACT PAGE MS# 1999-0900

Title: Vibrational Spectra, Heat Capacity and Speed of Sound of Methane

Authors: Ronald Tennis, Ryan Bailey and Giles Henderson*
Department of Chemistry
Eastern Illinois University
Charleston, IL 61920
*cfglh@eiu.edu

Keywords: Gases
Laboratory Equipment/Apparatus
Laser Spectroscopy
Physical Chemistry
Raman Spectroscopy
Statistical Mechanics

Abstract: A two-part physical chemistry laboratory experiment is described in which students evaluate statistical mechanical theory by comparing a measured speed of sound and heat capacity with values predicted from vibrational spectra. In part 1 students measure the IR spectrum of $CH_4(g)$ and the Raman spectrum of $CH_4(l)$ to determine quantized vibrational energy spacings. Strong Raman scattering of a pulsed nitrogen laser beam is observed with a liquid methane sample in a custom cryogenic cell constructed from two side arm test tubes and a length of Pyrex tube. This data is used with the statistical mechanics of a harmonic oscillator to calculate vibrational heat capacities, C_P/C_V, and the speed of sound of $CH_4(g)$. In part 2, the predicted speed of sound is compared with an experimental value measured with a simple acoustic resonance cavity (Kundt's tube) exhausted to a Bunsen burner.

Vibrational Spectra, Heat Capacity and Speed of Sound of Methane

Ronald Tennis, Ryan Bailey and Giles Henderson*

Department of Chemistry

Eastern Illinois University

Charleston, IL 61920

*cfglh@eiu.edu

Introduction

We have developed a two-part physical chemistry laboratory experiment in which students calculate the molar heat capacity ratio, $\gamma = C_p/C_v$ from an experimentally measured speed of sound. These results are then compared with values predicted by statistical mechanical theory and experimentally measured vibrational spectra and also compared with values predicted by the classical equipartition theorem.

Methane was selected for this study due to its suitability to both spectroscopic and convenient acoustic measurements. In part 1 students measure FTIR and Raman spectra to determine quantized vibrational energy levels of methane. This data is used with the statistical mechanics of a harmonic oscillator to calculate vibrational heat capacities (1, 2):

$$C_V\,(\text{vib}) = R \sum_{i}^{3N-6} \left[\left(\frac{\theta_i}{T} \right)^2 \xi_i \right] \qquad \mathbf{1}$$

where θ_i (°K) = $hc\bar{\nu}_i/k$ is the *characteristic vibrational temperature* of the i^{th} vibrational mode, h is Planck's constant, c is the speed of light $\bar{\nu}_i$ is the wavenumber of the ith mode in units of cm^{-1}, k = the Boltzman constant and

$$\xi_i = \frac{\exp(-\theta_i/T)}{[1 - \exp(-\theta i/T)]^2} \qquad \mathbf{2}$$

is known as an *Einstein function.*

Students use their calculated vibrational heat capacity along with assumed translational and rotational heat capacities as described by the classical equipartition theorem to calculate

$$\gamma = 1 + \frac{R}{C_v(trans) + C_v(rot) + C_v(vib)} \approx 1 + \frac{R}{3\ R + C_v(vib)} \qquad \mathbf{3}$$

and the corresponding speed of sound (eq. 4).

For an ideal gas:

$$c = \sqrt{\frac{\gamma R T}{M}} \qquad \mathbf{4}$$

where R is the gas constant, T is the Kelvin temperature and M is the molecular mass.

In part 2, the predicted speed of sound is compared with an experimental value measured with an acoustic resonance cavity (Kundt's tube) exhausted to a Bunsen burner.

Data acquisition can be completed in two three-hour laboratory periods. An alternate experimental format in which students are divided into three teams responsible for the IR, Raman and speed of sound measurements respectively, can be completed in a single lab period if teaching assistants are available to simultaneously supervise these components. In cases where spectroscopy equipment is unavailable, students could calculate vibrational frequencies using either *ab initio* or semi-empirical methods.

Experimental

I. FTIR Spectrum

Our students obtain infrared spectra of methane gas with a Nicolet 20DXB FTIR spectrometer using a 10 cm gas cell equipped with KBr windows. The sample cell is initially located in a hood and simply purged with ultra pure methane. The sample composition can be adjusted with nitrogen to produce the desired spectral intensity.

II. Raman Spectrum

We use a homemade Raman spectrometer which employs an inexpensive pulsed nitrogen laser (Laser Photonics LN300C) with a Hitachi 139 monochromator which has been retrofitted with a computer controlled wavelength stepper motor, a Hamamatsu R1414 photomultiplier and a Laser Science model 337971 gated integrator. This system is controlled by custom LabVIEW software which provides students with an interactive virtual control panel to set wavelength scan limits and step sizes, laser pulse delays, and to control signal averaging, data acquisition and display. Since we are unable to measure the very weak Raman scattering from methane gas samples, we have constructed a simple condenser/cell to facilitate measuring the Raman spectrum of liquid methane (Figure 1).

III. Speed of Sound

Our students use a variable audio frequency oscillator to generate acoustic standing waves at several resonance frequencies in a fixed length acoustic cavity equipped with a small speaker (Figure 2). Resonance modes are determined by maximum amplitude antinodes of the sound wave which are detected with a small piezoelectric microphone at the opposite end of the cavity and displayed with an oscilloscope. Students systematically tune the audio frequency through five or six consecutive resonance modes (ν_n) in the 0.6 - 1.5 kHz range. The resonance frequencies are measured with a digital frequency meter and the speed of sound is determined from the slope of a plot of ν_n vs the cavity mode number.

Our students first use this apparatus with pure nitrogen using a temperature corrected handbook value for the speed of sound of dry nitrogen to calibrate the length of the acoustic cavity. This procedure also insures that the cavity has been purged of air and that the subsequent flow of methane can not form an explosive mixture. A Bunsen burner

is connected to the exhaust port of the cavity by a length of rubber tubing and the methane flow rate is adjusted to support a small flame before resonance measurements are made.

Safety

Since methane is flammable and can form explosive mixtures with air/oxygen, the following precautions are essential:

1. The acoustic resonance cavity is purged with nitrogen prior to admitting methane.
2. The methane gas flow through the acoustic resonance cavity is consumed with a Bunsen burner.
3. Air is pumped out of the Raman cell before a methane gas flow is established and liquid nitrogen is added to the cold finger.
4. Safety glasses are absolutely essential, not only for mechanical protection, but also for protection from any scattered 337.1 nm uv radiation from the nitrogen laser.

Results and Discussion

Representative examples of gas phase IR and liquid phase Raman spectra are presented in Figures 3 and 4 respectively. The assigned transition frequencies are compared with literature values in Table 1. Ideally, gas phase frequencies are used to calculate vibrational heat capacities. However, we are unable to measure gas phase Raman signals since they are on the order of a thousand times weaker than liquid signals. Moreover, the small differences between liquid and gas phase frequencies (~10 cm^{-1}) has no perceptible effect on the heat capacity calculated to four significant figures. Students may also compare their results with a gas phase IR spectrum available from the NIST web page: http://webbook.nist.gov/chemistry

Table 1. Infrared and Raman bands of methane. All frequencies are in cm^{-1}.

Assignment	Spectrum (phase)	Student Measurements	Literature Value	Reference
ν_1	Raman (l)	2911±14	2909	3
ν_2	Raman (l)	1542±14	1535	4
ν_3	IR (g)	3016±2	3019	5
ν_4	IR (g)	1304±2	1306	5
$\nu_2 + \nu_3$	IR (g)	4544±2	4533[a]	5
$\nu_3 + \nu_4$	IR (g)	4315±2	4307[a]	5
$\nu_1 + \nu_4$	IR (g)	4217±2	4206[a]	5

[a] Liquid phase Raman peaks observed by Crawford et.al (5).

Figure 5 illustrates a representative plot of the acoustic cavity resonance frequencies vs the cavity mode index number.

Characteristic vibrational temperatures, Einstein functions and the corresponding contribution of each vibrational mode to the vibrational heat capacity are calculated from eq (4) and (5) and summarized in Table 2.

Table 2. Statistical mechanics of CH_4 vibrational modes at 298 K.

i	$\bar{\nu}_i$ [a]	g_i [b]	θ_i/T [c]	ξ_i [d]	$g_iC_v(i)$ [e]
1	2911	1	14.05	7.910×10^{-7}	1.561×10^{-4} R
2	1542	2	7.445	5.850×10^{-4}	6.485×10^{-2} R
3	3016	3	14.56	4.750×10^{-7}	3.021×10^{-4} R
4	1304	3	6.296	1.850×10^{-3}	2.200×10^{-1} R

[a] $\bar{\nu}_i$ is the wavenumber of the i^{th} vibrational mode.
[b] g_i = degeneracy.
[c] θ_i = Einstein function.
[d] $g_iC_v(i)$ = the contribution of i^{th} vibrational mode to the heat capacity as calculated from eq (4) and (5).

$$C_v(vib) = \Sigma g_iC_v(i) = 0.2853 \text{ R}$$

$$C_v = 3.2853 \text{ R}$$

This value of the vibrational heat capacity is then combined with classical translational and rotational values to obtain C_v, the molecular heat capacity at constant volume. This result is compared with both the classical and strongly quantized limits as well as a literature value in Table 3.

Table 3. Heat capacity, γ-values and speed of sound of CH_4 at 298 K.

Quantity	Calc from IR/Raman Spectra[a]	Student Exp. Value	Lit Value Ref.	Class-ical Limit[d]	SQL Limit[e]
C_v (J/mol*K)	27.31	-	27.33[b]	99.8	24.9
γ	1.30	1.27±.06	1.304[b]	1.08	1.33
c (m/s)	449	444±10	451[c]	410	454

[a] Propagation of uncertainties in wavenumber measurements gives ±0.1% precision limits of calculated quantities.
[b] NIST ref. 6
[c] Handbook value (7) corrected to 298 K.
[d] The classical limit assumes $\Delta E_i(vib)$ 0 and that $C_v(vib) = (3N - 6)R$.
[e] Strongly quantized limit: assume $\Delta E_i(vib) > kT$ for all modes.

It is evident (Table 3) that the heat capacity calculated from the IR and Raman spectra, the γ-value calculated from eq (3) and the speed of sound calculated from eq (4) are not only bracketed by the classical and strongly quantized theoretical limits, but are in good agreement with the experimental and measured literature values. Students use the results of their statistical mechanical analyses to plot the partitioning of internal energy as shown in Figure 6.

This new physical chemistry lab experiment introduces important concepts and techniques to students.

1) It demonstrates the power of statistical mechanics to predict bulk properties from the quantum descriptions of particles.
2) It illustrates how the partitioning of internal energy depends on the spacing between quantum levels.
3) A small symmetric molecule like methane provides a good opportunity to apply symmetry criteria of IR and Raman activity.

4) Raman measurements of liquid methane introduce students to cryogenic, vacuum line and laser techniques.

5) The acoustic measurements illustrate a resonance phenomenon in a simple, easy to understand system.

6) The theoretical model discloses how the speed of sound is diminished when energy that would otherwise contribute to translation is diverted to rotation and vibration.

A more rigorous treatment could consider the effects of quantum restrictions on rotational energies and the effects of anharmonicty on vibrational energy spacings, particularly the low frequency ν_2 and ν_4 bending modes.

Acknowledgments

The authors wish to express their gratitude to the National Science Foundation, Instrument and Laboratory Improvement Grant No. DUE-9551644, for supporting the development of laser spectroscopy in our undergraduate curriculum.

Literature Cited

1. McQuarrie, D. A. *Statistical Thermodynamics*, Harper & Row, New York, **1973**, 130-132.

2. Shoemaker, D. P.; Garland, C. W.; Nibler, J. W. *Experiments in Physical Chemistry*, 6th ed., McGraw-Hill: New York, **1996**, p. 386.

3. Rest, A.; Warren, R.; Murray S. *Spectrochim. Acta. Part A*, **1996**, 52, 1455-1463.

4. Crawford, M.; Welsh, H.; Harrold, J. *Can. J. Phys.* **1952**, 30, 81-98.

5. Shimanouchi, T. *Tables of Molecular Vibrational Frequencies Consolidated Volume I.*, National Bureau of Standards, **1972**, 78.

6. "NIST-JANAF Thermochemical Tables", 4th ed., Chase, M. W., Jr., Ed.; *J. Phys. Chem. Ref. Data*, Monograph 9, **1998.**

7. *Handbook of Chemistry and Physics*, 43rd ed., Hodgman, C. D., Ed.; CRC: Cleveland OH, **1962**.

Figure 1: A simple methane condenser/Raman cell was constructed from two side arm test tubes, a length of Pyrex tube and rubber stoppers. The laser beam is aligned with the center of the coaxial tubes to avoid side reflections of the beam directly into the monochromator. Coaxial alignment of the sample and Dewar tubes is maintained with a cork ring-spacer. We find attenuation of the 337.1 nm laser radiation by the Pyrex negligible.

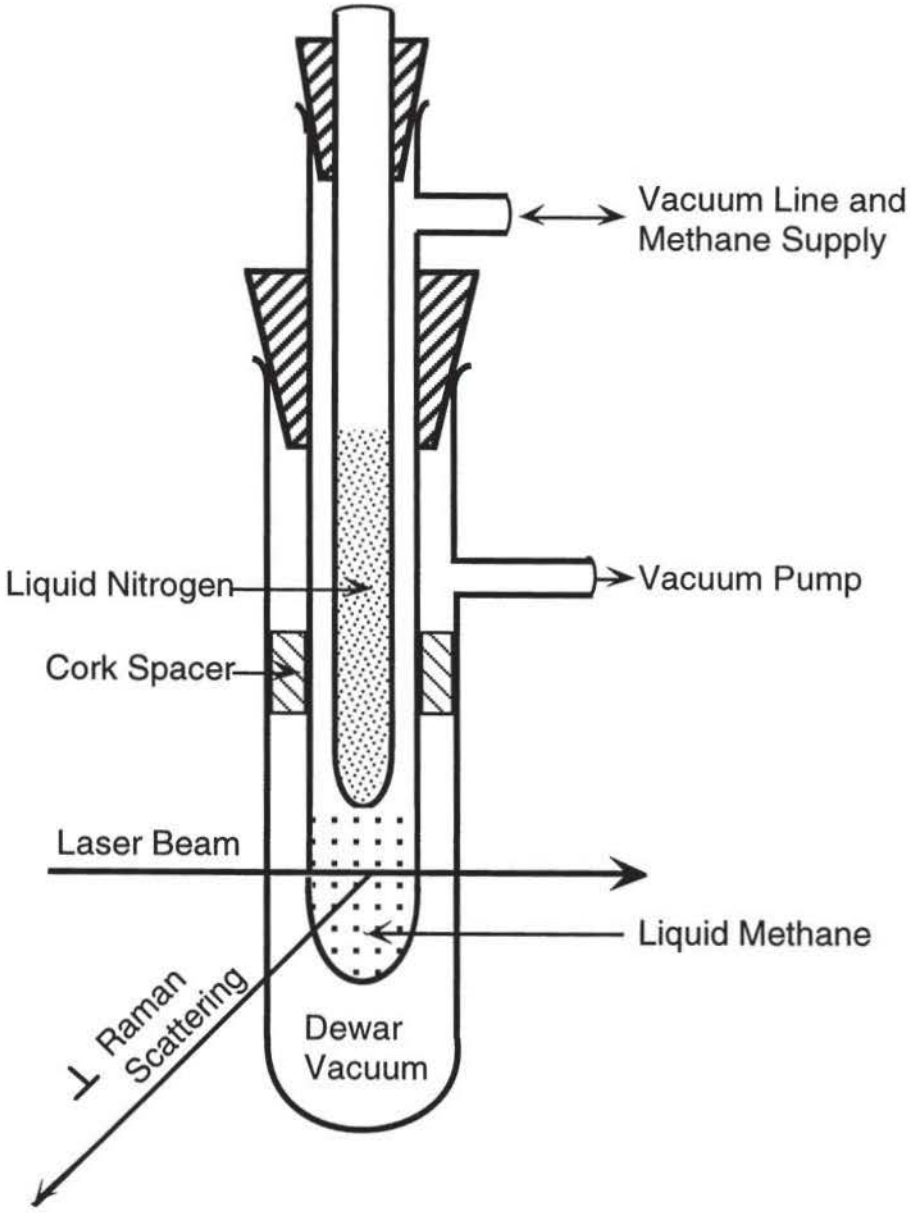

Figure 2: Experimental set up to measure the speed of sound in methane with an acoustic resonance cavity.

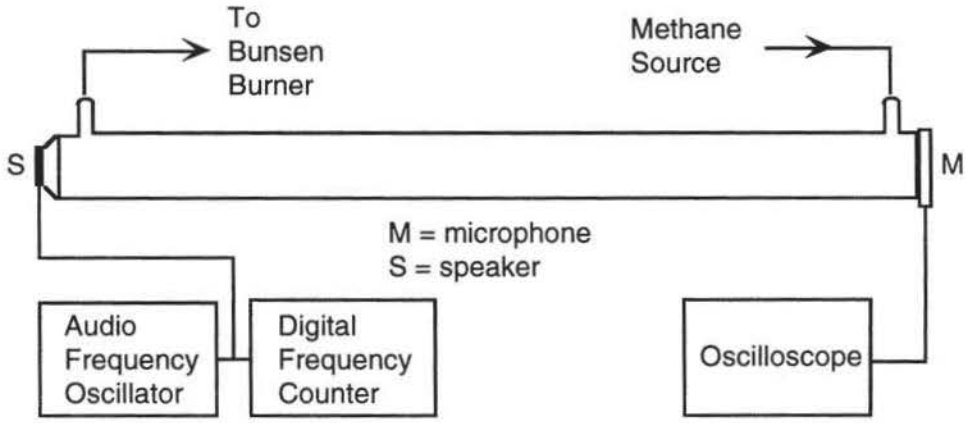

Figure 3: Gas phase IR absorption spectrum of methane at room temperatures.

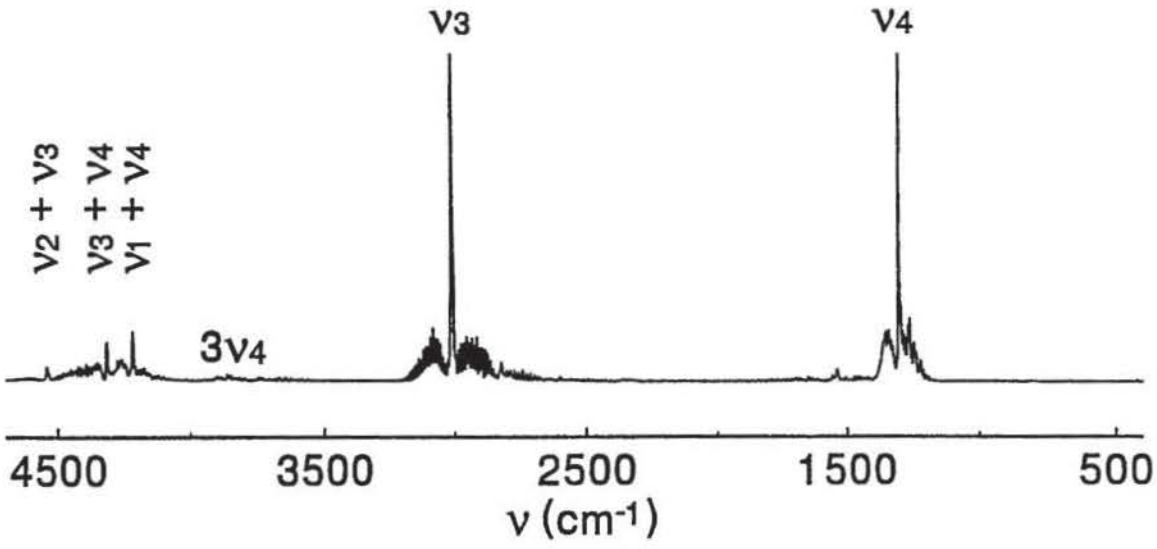

Figure 4: Raman spectrum of liquid methane at approximately 101 K.

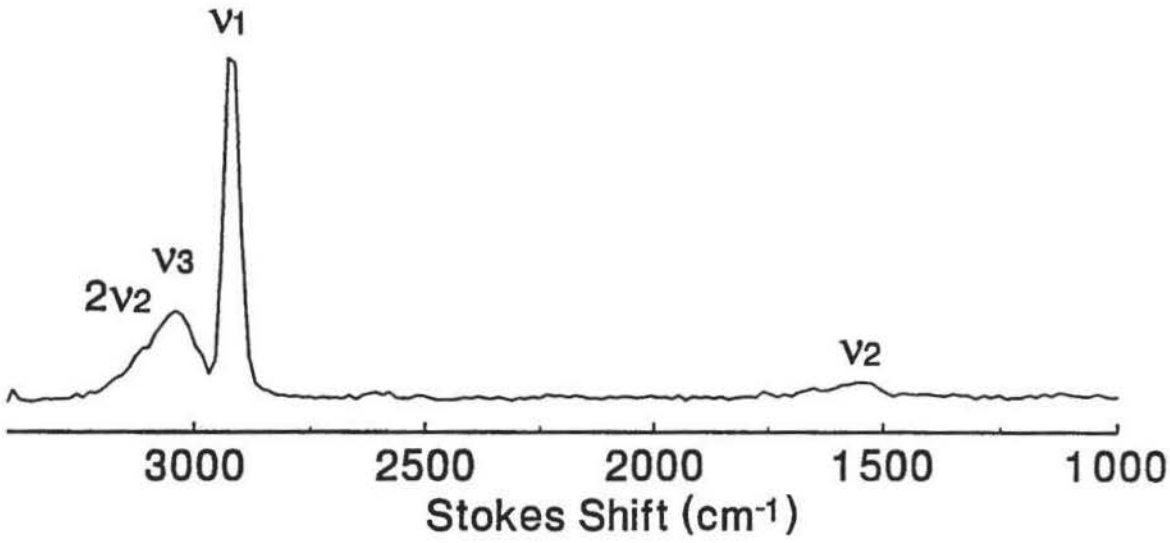

Figure 5: Acoustic cavity resonance modes of methane.

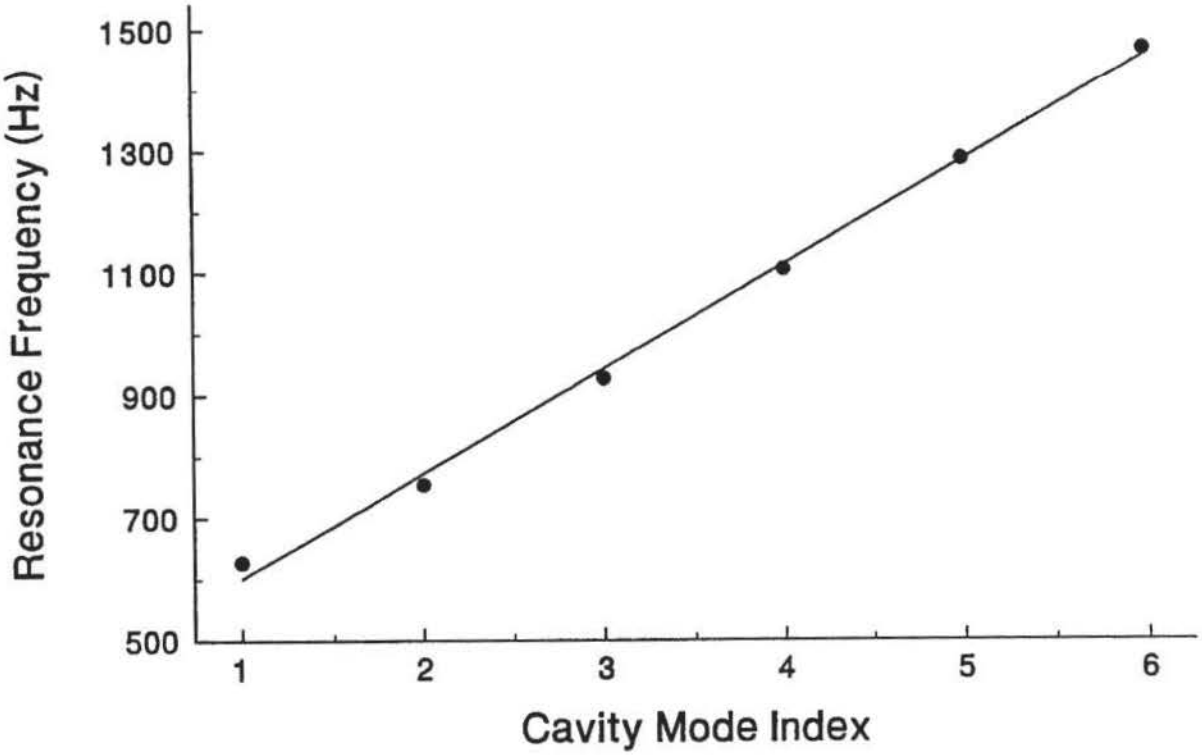

Figure 6: Partitioning of internal energy in methane at 298 K.